AFOSR-TR- 85-0163

IFSM-85-133

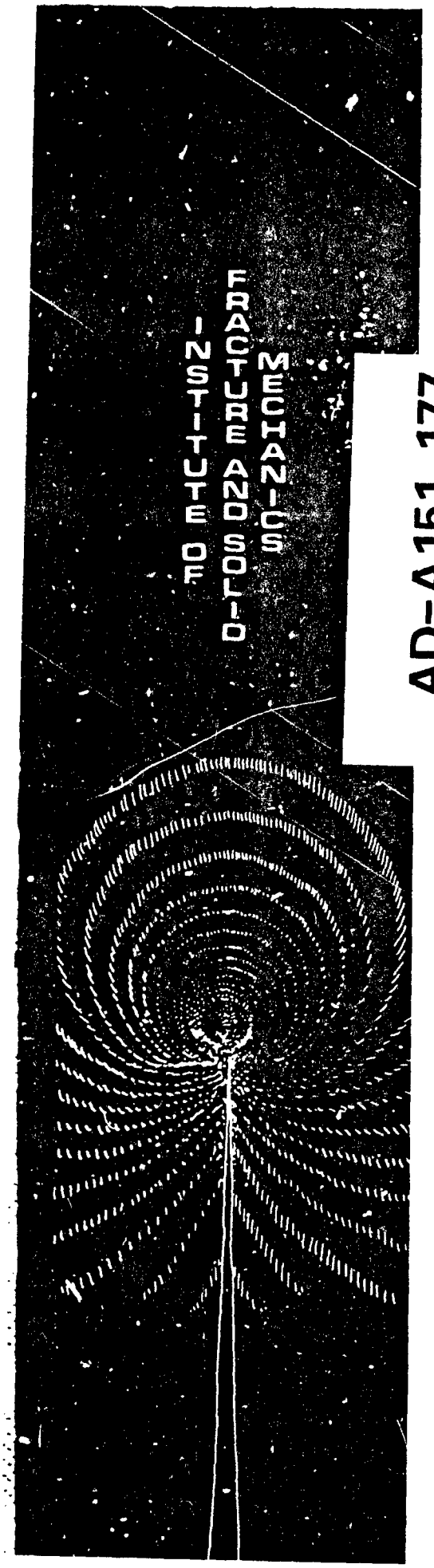

LEHIGH UNIVERSITY

AD-A151 177

MECHANISMS OF CORROSION FATIGUE IN HIGH STRENGTH I/M AND P/M ALUMINUM ALLOYS

by

20030115038

R. P. Wei
Lehigh University

and

P. S. Pao
McDonnell Douglas Research Laboratories

DTIC FILE COPY

DTIC
ELECTE
MAR 13 1985
S D
E

November, 1984

Approved for public release;
distribution unlimited.

Final Technical Report

Air Force Office of Scientific Research

Contract No. F49620-81-K-0004

MECHANISMS OF CORROSION FATIGUE IN HIGH STRENGTH I/M AND P/M ALUMINUM ALLOYS

by

R. P. Wei
Lehigh University

and

P. S. Pao
McDonnell Douglas Research Laboratories

Accession For	
NTIS GRA&I	☒
DTIC TAB	☐
Unannounced	☐
Justification	
By	
Distribution/	
Availability Codes	
Dist	Avail and/or Special
A-1	

November, 1984

Final Technical Report

AIR FORCE OFFICE OF SCIENTIFIC RESEARCH

(Contract No. F49620-81-K-0004)

DTIC COPY INSPECTED

This document has been approved for public release; its distribution is unlimited.

AIR FORCE OFFICE OF SCIENTIFIC RESEARCH (AFSC)
NOTICE OF TRANSMITTAL TO DTIC
This technical report has been reviewed and is approved for public release IAW AFR 190-12.
Distribution is unlimited.
MATTHEW J. KERPER
Chief, Technical Information Division

UNCLASSIFIED

SECURITY CLASSIFICATION OF THIS PAGE (When Data Entered)

Caplan

REPORT DOCUMENTATION PAGE		READ INSTRUCTIONS BEFORE COMPLETING FORM
1. REPORT NUMBER ~~FRGM-85-163~~ AFOSR-TR- 85-0163	2. GOVT ACCESSION NO. AD-A153	3. RECIPIENT'S CATALOG NUMBER 177
4. TITLE (and Subtitle) MECHANISMS OF CORROSION FATIGUE IN HIGH STRENGTH I/M AND P/M ALUMINUM ALLOYS		5. TYPE OF REPORT & PERIOD COVERED Final Technical Report 1 Jan 81 - 30 Sep 84
		6. PERFORMING ORG. REPORT NUMBER Final Technical Report
7. AUTHOR(s) R. P. Wei, Lehigh University P. S. Pao, McDonnell Douglas Research Laboratories		8. CONTRACT OR GRANT NUMBER(s) Contract No. F49620-81-K-0004
9. PERFORMING ORGANIZATION NAME AND ADDRESS Lehigh University Bethlehem, PA 18015		10. PROGRAM ELEMENT, PROJECT, TASK AREA & WORK UNIT NUMBERS 61102F, 2306, A1
11. CONTROLLING OFFICE NAME AND ADDRESS Air Force Office of Scientific Research/NE Bolling Air Force Base, DC 20332		12. REPORT DATE November, 1984
		13. NUMBER OF PAGES 147
14. MONITORING AGENCY NAME & ADDRESS(if different from Controlling Office)		15. SECURITY CLASS. (of this report) Unclassified
		15a. DECLASSIFICATION/DOWNGRADING SCHEDULE

16. DISTRIBUTION STATEMENT (of this Report)

This document has been approved for public release; its distribution is unlimited.

17. DISTRIBUTION STATEMENT (of the abstract entered in Block 20, if different from Report)

18. SUPPLEMENTARY NOTES

19. KEY WORDS (Continue on reverse side if necessary and identify by block number)

Aluminum alloy; corrosion fatigue; fracture mechanics; microstructure; environmental effects.

20. ABSTRACT (Continue on reverse side if necessary and identify by block number)

High strength aluminum alloys are employed extensively in the primary structure of current and projected Air Force and civilian aircraft. The service lives and reliability of these aircrafts depend to a great extent on the corrosion fatigue resistance of the structural alloys. Significant efforts are underway to develop powder metallurgy (P/M) alloys that would provide improved corrosion fatigue resistance along with improvements in other mechanical properties. The objective of this

DD FORM 1 JAN 73 1473 EDITION OF 1 NOV 65 IS OBSOLETE S/N 0102-014-6601

UNCLASSIFIED

SECURITY CLASSIFICATION OF THIS PAGE (When Data Entered)

study was to understand the chemical and metallurgical aspects of environmentally assisted fatigue crack growth (or corrosion fatigue) that can serve (i) as a basis for guiding the development of new and improved alloys, and (ii) as a basis for developing rational design procedures for service life predictions. A coordinated fracture mechanics, surface chemistry and materials science approach was used. The research was performed by Lehigh University with technical support by McDonnell Douglas Research Laboratories.

The kinetics of fatigue crack growth, as a function of water vapor pressure and for water vapor-oxygen mixtures, and the accompanying fractographic observations on 7050-T7451, 7050-T651 and 7075-T651 (I/M) alloys and on 7091-T7E69 and 7091-T7E70 (P/M) alloys are described and discussed. Comparison between the I/M and P/M alloys are given, and indicates that the micromechanisms for crack growth are similar and that the environmental enhancement of crack growth is consistent with embrittlement by hydrogen. Based on this study, a revision of the superposition model for corrosion fatigue was made to give recognition to the fact that fatigue and corrosion fatigue can proceed by different micromechanisms and in parallel. Critical evaluations and improvements in understanding of a model for transport controlled crack were accomplished. The important role of yield strength and microstructure-controlled fracture surface roughness was identified. The chemical role of segregated magnesium in influencing the susceptibility of 7000 series (AlMgZn and AlMgZnCu) alloys to corrosion fatigue crack growth have been established. Needs for further work to capitalize on the research findings and to develop further understanding are discussed.

TABLE OF CONTENTS

	Page
FORWARD	i
ABSTRACT	ii
1.0 INTRODUCTION	1
2.0 MATERIAL AND EXPERIMENTAL WORK	6
2.1 Material	6
2.1.1 7075-T7451 (I/M) Alloy	6
2.1.2 7075-T651 (I/M) Alloy	8
2.1.3 7091-T7E69 and 7091-T7E70 (P/M) Alloy	9
2.2 Fatigue Crack Growth Tests	10
2.2.1 Specimen and K Calibration	10
2.2.2 Test Environment	12
2.2.3 Fatigue Testing Procedure	12
2.2.4 Crack Monitoring System	13
2.3 Fractography	14
2.4 Surface Reaction Kinetics	15
3.0 RESULTS	18
3.1 Kinetics of Fatigue Crack Growth	18
3.1.1 7050-T7451 and 7050-T651 (I/M) Aluminum Alloys	18
3.1.2 7075-T651 (I/M) Aluminum Alloy	19
3.1.2.1 Room Temperature (295K)	19
3.1.2.2 "High" Temperature (354K)	21
3.1.3 7091-T7E69 and 7091-T7E70 (P/M) Aluminum Alloys	22
3.1.4 Inhibition by Oxygen	23
3.2 Fractographic Analysis	24
3.2.1 7050-T7451 (I/M) Alloy	25
3.2.2 7050-T651 (I/M) Alloy	26
3.2.2.1 Fractographic Observations	26
3.2.2.2 Micro-Etch-Pit Analyses	30
3.2.3 7091 (P/M) Alloy	31
3.2.4 Comparison between I/M and P/M Alloys	32

3.3 Surface Segregation and Surface Reaction Kinetics 33

4.0 DISCUSSIONS 36

4.1 Comparison between I/M and P/M Alloys 36

4.2 Reconsideration of the Superposition Model 38

4.3 Modeling of the Effect of Load Ratio 41

4.4 Critical Assessment of the Model for Transport-Controlled Fatigue Crack Growth 42

4.5 Role of Magnesium in Corrosion Fatigue 48

5.0 SUMMARY 53

6.0 REFERENCES 57

7.0 DEGREES, PRESENTATIONS AND PUBLICATIONS 59

TABLES 61

FIGURES 63

FORWARD

This research was conducted by Lehigh University (LU) and the McDonnell Douglas Research Laboratories (MDRL) as a technical team, with Lehigh serving as the lead laboratory (prime contractor), and was originally planned for three (3) years. A 9-month extension was granted to allow for a fuller exploration of the chemical role of magnesium in influencing corrosion fatigue susceptibility of 7000 series aluminum alloys. Dr. Robert P. Wei from Lehigh and Dr. Peter S. Pao from MDRL were the principal personnel involved with this program. Dr. Gary W. Simmons of Lehigh provided support for the surface chemistry portions of the program. Mr. Ming Gao, a Ph.D. candidate in Metallurgy and Materials Engineering, participated in this program as a Research Assistant, and received his Ph.D. degree in 1983.

The 7091-T7E69 (P/M) and 7050-W (I/M) alloys were provided to this program by ALCOA through the courtesy of the ALCOA Foundation. The kind assistance of Phil Bretz, Robert Bucci and Walt Cebulak of ALCOA, with material procurement and in providing material property data, is gratefully acknowledged.

FINAL TECHNICAL REPORT
(AFOSR Contract No. F49620-81-K-0004)

MECHANISMS OF CORROSION FATIGUE IN HIGH STRENGTH I/M AND P/M ALUMINUM ALLOYS

by

R. P. Wei
Lehigh University
and
P. S. Pao
McDonnell Douglas Research Laboratories

ABSTRACT

High strength aluminum alloys are employed extensively in the primary structure of current and projected Air Force and civilian aircraft. The service lives and reliability of these aircrafts depend to a great extent on the corrosion fatigue resistance of the structural alloys. Significant efforts are underway to develop powder metallurgy (P/M) alloys that would provide improved corrosion fatigue resistance along with improvements in other mechanical properties. The objective of this study is to understand the chemical and metallurgical aspects of environmentally assisted fatigue crack growth (or corrosion fatigue) that can serve (i) as a basis for guiding the development of new and improved alloys, and (ii) as a basis for developing rational design procedures for service life predictions. A coordinated fracture mechanics, surface chemistry and materials science approach is used. The research is being performed by Lehigh University with technical support by McDonnell Douglas Research Laboratories.

The kinetics of fatigue crack growth, as a function of water vapor pressure and for water vapor-oxygen mixtures, and the accompanying fractographic observations and surface reaction kinetics, on 7050-T7451, 7050-T651 and 7075-T651 (I/M) alloys and on 7091-T7E69 and 7091-T7E70 (P/M) alloys are described and discussed. Comparison between the I/M and P/M alloys are given, and is discussed in relation to the micromechanisms for crack growth and environmental response. Based on this study, a revision of the superposition model for corrosion fatigue was made. This revision and its implication are described and discussed. Critical evaluations of a model for transport controlled crack were made, and improvements in understanding were obtained. The important role of yield strength and microstructure-controlled fracture surface roughness was identified. The chemical role of segregated magnesium in influencing the corrosion fatigue susceptibility of 7000 series alloys was established. The implications of these findings on alloy development are discussed.

1.0 INTRODUCTION

This report describes work performed on "Mechanisms of Corrosion Fatigue in High Strength I/M and P/M Aluminum Alloys". High-strength aluminum alloys are used extensively in the primary structures of military and commerical aircraft. These alloys are based on either the Al-Cu system (2000 series alloy) or the Al-Zn-Mg or Al-Zn-Mg-Cu systems (7000 series alloys). Because these aircraft parts are exposed to chemically-active service environments, such as moisture and runway salt sprays, their useful lives and reliability depend on the corrosion fatigue resistance of the structural alloys. The need for improved performance, greater structural reliability, and longer service lives in advanced aircraft designs have called for new and improved alloys that combine high strength, good fracture toughness, and improved corrosion fatigue resistance. Significant improvements in these properties have been achieved on alloys produced by ingot metallurgy (I/M alloys) during the past decade through better ingot processing, improved compositions, and the use of thermo-mechanical treatments.

In recent years, powder metallurgy (P/M) or rapid solidification processing (RSP) have emerged as alternative routes for the optimization of aluminum alloy properties and for the development of new alloys. High solidification rates associated with the production of P/M alloys minimize segregation, reduce significantly the size and volume fraction of constituent particles, and refine and homogenize the microstructures. Rapid solidification processing also offers considerable freedom in alloying and

thus permits the processing of new and novel compositions that cannot be handled readily by ingot (I/M) techniques. These alloys promise to provide high strength, along with good fracture, fatigue and stress corrosion cracking resistances, and are undergoing considerable development. The alloy development effort is expected to accelerate in the coming years.

The resistance of high-strength I/M and P/M aluminum alloys to crack growth under fatigue loads is known to be influenced by moisture in the surrounding air. Water vapor can significantly accelerate fatigue crack growth and thereby speed the failure of structural components. This effect of water vapor is strongly coupled to the frequency of load fluctuations over a critical range of water vapor pressures. Fatigue crack growth can also be influenced by alloy composition and microstructure, the presence of oxygen, temperature, load ratio (R), material thickness (or thickness in relation to plastic zone size), stress intensity range, and the processes used in preparing the alloys. It is recognized that the interactions among these variables complicate the proper interpretation and extrapolation of experimental data and introduce additional uncertainties with respect to damage-tolerant design and failure analysis.

A systematic investigation has been conducted of the effects of environmental, mechanical, and metallurgical variables on the fatigue crack growth characteristics of high strength I/M and P/M aluminum alloys. The program was directed towards (i) the development of a quantitative understanding of the influence of

metallurgical variables on the rates and mechanisms of surface reactions of water vapor with I/M and P/M aluminum alloys, and the chemical, metallurgical and mechanical interactions responsible for environmentally assisted fatigue crack growth, and (ii) the formulation and evaluation of improved models for predicting crack growth response. It utilized the combined fracture mechanics, surface chemistry and materials science approach that had been applied successfully to elucidate environmentally assisted crack growth in steels and titanium alloys, and capitalized on models that had already been developed (see [1-3] and other references cited therein).

The specific research objectives were to:

(1) Quantify the influences of composition and microstructure (including precipitate type and distribution, impurities, etc.) on chemical reaction kinetics and fatigue crack growth rates and response, with particular emphasis on comparisons between I/M and P/M alloys.

(2) Verify the proposed model [1-3] for a range of aluminum alloys, with different compositions and microstructures, by measuring both fatigue crack growth response as a function of water vapor pressure and frequency, and the appropriate chemical reaction rates.

(3) Modify the proposed model [1-3] to incorporate other significant variables (such as load ratio, waveform, and thickness), and verify the model for a broad range of loading and environmental variables.

(4) Develop a quantitative mechanism for embrittlement and formulate a model for estimating the rates of environmentally assisted fatigue crack growth that incorporates the significant chemical, metallurgical and mechanical variables.

Fracture mechanics techniques, quantitative metallography (including scanning and transmission electron microscopy), and surface analysis techniques (such as Auger electron and x-ray photoelectron spectroscopy) are used.

2219-T851, 7050-T7451 (formerly 7050-T73651) and 7075-T651 aluminum alloys were included in this study to represent 2000 and 7000 series I/M alloys that are or may be used in current and advanced Air Force aircraft. Alloy 7091, the most probable 7000 series P/M alloy to be utilized and to be available in quantity, was selected as the representative 7000 series P/M alloy. Since no suitable 2000 series P/M alloy was available, a small quantity of P/M alloy was made to the 2219 alloy composition for use in the third year of this study. This experimental 2000 series P/M alloy, however, failed to meet specifications, and was not included in further studies. The other alloys provided a reasonable range of composition and microstructure for evaluation and comparison. Two aging treatments were used on the 7050 (I/M) and 7091 (P/M) alloys to further investigate the influence of temper and microstructure. Results from this study are compared with available data on other 2000 and 7000 alloys to broaden the basis of understanding corrosion fatigue mechanisms. Adequate numbers

of replicate tests were carried out for selected alloys and test conditions to assess inter-laboratory and intra-laboratory variability and to ensure statistical significance of the test results. The results from this program are summarized and discussed. Modeling of crack growth response is also considered.

2.0 MATERIAL AND EXPERIMENTAL WORK

2.1 Material

7050-T7451 (formerly 7050-T73651) and 7075-T651 aluminum alloys are included in this study, in conjunction with 2219-T851 alloy used in a previous study [1], to represent 2000 and 7000 series I/M alloys that are or may be used in current and advanced Air Force aircraft. Alloy 7091, the most probable 7000 series P/M alloy to be utilized and to be available in quantity, was selected as the representative 7000 series P/M alloy. Since no suitable 2000 series P/M alloy was available, a small quantity of P/M alloy was made to the 2219 alloy composition for use in the third year of this study. Because of manufacturing difficulties, this experimental P/M alloy proved to be unsatisfactory and was not examined further.

The remaining alloys provided a reasonable range of compositions and microstructures for evaluation and comparison. Two aging treatments were used on the 7050 (I/M) and 7091 (P/M) alloys to further investigate the influence of temper and microstructure. In addition a 7075-T7351 alloy was included in the surface chemistry studies to examine the effects of heat treatment on segregation and on reaction kinetics. Qualification and characterization of the principal alloys used are described in the following subsections.

2.1.1 7050-T7451 (I/M) Alloy

Qualification and microstructural characterization of the 25.4 mm thick 7050-T7451 aluminum alloy plate were carried out. Chemical composition and tensile properties of this plate are

given in Table 1, and conform with specifications [4,5]. Fracture toughness measurements were made using 12.7 mm thick compact tension (CT) specimens in the LT orientation in accordance with ASTM Method E-399. The indicated values (K_Q) are also given in Table 1. The specimen thickness was not sufficient for these values to qualify as "valid" plane strain fracture toughness (K_{Ic}), but the values suggest the level of fracture toughness of this plate is consistent with that of the 7050-T7451 alloy.

Texture for this plate was determined from distributions of the {200}, {220} and {111} poles at the surface and mid-thickness plane of the plate (see Figs. 1 and 2). The results indicate a strong preferred orientation for this plate, with a $(110)[\bar{2}\bar{1}1]$ rolling texture. In other words, most of the grains are aligned with their {110} planes nearly parallel to the plate surface and their <211> directions along the rolling direction. The transverse direction coincides with one of the <111> directions in the crystal.

Optical and transmission electron micrographs for the 7050-T7451 alloy are shown in Figs. 3 and 4. The optical micrographs (Fig. 3) shows a partially recrystallized structure that is typical of this heat treatment or temper. The transmission electron micrographs (Fig. 4) indicate a dense distribution of precipitates and a high density of dislocations in this alloy. The precipitates have been identified, and are composed of the hexagonally shaped equilibrium $\eta(MgZn_2)$phase and the intermediate η'

phase [6]. Both types of precipitates are present at the grain boundaries, and there does not appear to be a clearly discernible precipitate-free (or "denuded") region adjacent to the grain boundaries.

Selected area diffraction (SAD) analyses have been made (see Fig. 5), and show that the coarse hexagonal η precipitates can be indexed as shown in Fig. 5c. The lattice parameters of this phase are determined to be a = 0.52 nm and c = 0.85 nm. The crystallographic relationship between the precipitate and the matrix is as follows:

$$(\bar{1}100)\eta//(011\bar{1})_{Al};\quad [0001]\eta//[011]_{Al}$$

Hence, these η precipitates correspond to η_9 in the classification scheme of Gjønnes and Simensen [7]. The plate-like precipitates are tentatively identified as the transitional η' phase. SAD analyses showed that the lattice parameters are a = 0.51 nm and c = 0.67 nm. These values are close to but are not in complete agreement with those reported by Gjønnes and Simensen [7]. Additional work to better identify these precipitates is needed.

2.1.2 <u>7075-T651 (I/M) Alloy</u>

A 12.7 mm thick plate of commercial 7075-T651 aluminum alloy was used. The nominal composition and mechanical properties of this alloy are given in Table 1 [4,5]. Representative optical and transmission electron micrographs of the alloy microstructure are shown in Figs. 6 and 7. The overall grain structure of this alloy is similar to that of the 7050-T7451 alloy. The anisotropic nature of the uncrystallized grains is evident in Fig. 1,

with "packets" of grains elongated along the rolling direction (L) of the plate. Transmission electron micrographs indicate the typical microstructure of 7075-T651 alloy contains a high density of η' precipitates and of dislocations. A number of large "constituent" particles (some as large as 1 μm) are also present.

2.1.3 7091-T7E69 and 7091-T7E70 (P/M) Alloy

38 mm by 114 mm (1.5 in. by 4.25 in.) extrusions of 7091-T7E69 and 7091-T7E70 (P/M) alloys were obtained from ALCOA. The T7E69 designation refers to an over-aging treatment of 4 h, while T7E70 refers to over-aging for 14 h. Chemical composition and tensile properties of these extrusions were supplied by ALCOA and are given in Table 1 [8]. Fracture toughness of these extrusions was measured with the use of 24.7 mm (0.97 in.) thick wedge-opening-load (WOL) specimens. For 7091-T7E69, the plane strain fracture toughness, K_{Ic} was determined to be 44.6 MPa$\sqrt{m}$. The measured fracture toughness for 7091-T7E70 of 58.7 MPa$\sqrt{m}$ failed to satisfy the specimen thickness requirement and is not considered to be a "valid" K_{Ic} measurement.

The crystallographic texture of 7091-T7E70 alloy was again determined from the distributions of {200}, {220} and {111} poles at the surface and mid-thickness planes of the extrusion (see Figs. 8 and 9). The results indicate that the 7091-T7E70 alloy has a $(110)[1\bar{1}2]$ type texture. This texture is similar to that observed in the 7050-T7451 alloy plate, except that the texture is sharper in the 7091-T7E70 alloy extrusion. Texture determination was not made on the 7091-T7E69 alloy extrusion. It is

expected, however, that the texture for the two extrusions would be similar.

Representative optical micrographs of the 7091-T7E70 alloy are shown in Fig. 10, and show the extremely fine-grained structure of this P/M alloy. Transmission electron micrographs of 7091-T7E70 alloy are shown in Figs. 11 and 12. Figure 11 shows typical grains or subgrains of this alloy, which are on the order of 1 to 3 μm in dimension. The pair of bright-field and dark-field transmission electron micrographs in Fig. 12 show the precipitates in this alloy. The precipitates in the matrix and along the grain boundaries are the equilibrium η ($MgZn_2$) and intermediate η' phases [6,7]. Some coarse precipitates are present at the boundaries, and there appears to be a narrow precipitate free zone adjacent to the grain boundaries. Unlike the I/M alloys, large constituent particles were not observed in this 7091 (P/M) alloy.

2.2 Fatigue Crack Growth Tests

2.2.1 Specimen and K Calibration

Compact tension (CT) and modified wedge-opening-load (WOL) specimens, with thickness (B) of 12.7 mm (0.5 in.) and width (W) of 63.5 mm (2.5 in.), were used. The CT specimens were used for the I/M alloys, and the WOL specimens were used for the P/M alloys to conserve material. The specimens were oriented in the longitudinal (LT) orientation, that is, with the crack plane perpendicular and the crack growth direction transverse to the rolling (or extrusion) direction.

An initial (or crack starter) notch, 15.9 mm (0.625 in.) in length, was introduced into each specimen by electrodischarge machining (EDM). Each specimen was precracked in fatigue, while exposed to the test environment, through a decreasing sequence of loads that terminated at the desired load level (or initial K) for the actual experiment. The precracking procedure provided a fatigue crack of about 2.5 mm (0.1 in.) in length from the starter notch, corresponding to a crack length of about 18.4 mm at the start of each experiment. This precracking procedure ensured that the subsequent fatigue crack growth would be through material that had not been altered by the notch preparation procedure, and would be unaffected by the starter notch geometry.

The stress intensity factor, K, for the CT specimen was computed from Eqn. (1) [9]:

$$K = (P/BW^{1/2})\{(2 + a/W)/(1-a/W)^{3/2}\}\{0.886 + 4.64(a/W) - 13.32(a/W)^2 + 14.72(a/W)^3 - 5.6(a/W)^4\} \quad (1)$$

P = applied load; B = specimen thickness, W = specimen width, and a = crack length. Both specimen width and crack length are measured from the line of loading. The stress intensity factor for the modified WOL specimen was computed from Eqn. (2) [9]:

$$K = (Pa^{1/2}/BW)\{30.96 - 195.8(a/W) + 730.6(a/W)^2 - 1186.3(a/W)^3 + 754.6(a/W)^4\} \quad (2)$$

The terms in Eqn. (2) are defined in the same way as those in Eqn. (1).

2.2.2 Test Environment

Crack growth experiments were performed inside a modified commercial ultrahigh vacuum chamber using a static environment. The test environment included pure argon, pure oxygen, vacuum and high purity water vapor. Experiments in vacuum were made at pressures below 1.3×10^{-6} Pa. Experiments in argon, oxygen and water vapor were made by back-filling the chamber with the selected gases from sources attached to the chamber. Purification of argon and oxygen was achieved by passing the high purity gases through a cold-trap at about 77 K, principally to remove residual water vapor. High purity water vapor was obtained from a source containing triply distilled water that had been subjected to alternate cycles of freezing, and thawing and pumping to remove dissolved gases. Prior to each experiment, the chamber was baked out and evacuated to about 1.3×10^{-6} Pa. The test environment was then admitted into the chamber to the prescribed pressure. Pressure was monitored by a capacitance manometer. Purity was checked with the aid of a quadrupole residual gas analyzer.

2.2.3 Fatigue Testing Procedure

The fatigue crack growth experiments were carried out principally under constant amplitude loading in a closed-loop electrohydraulic testing machine operated in load control at a load ratio (R) of 0.1, and at a frequency of 5 Hz. Load control was estimated to be better than ± 1 pct. Some experiments were carried out under constant stress intensity range conditions, where ΔK was maintained constant by computer-controlled load shedding.

To investigate the effects of temperature, some experiments were carried out at 353 K (80°C). The test temperature was achieved by heating the entire environmental chamber with electrical heating tapes, and was maintained constant to within ± 2 K.

2.2.4 Crack Monitoring System

An ac electrical potential system was used for monitoring crack growth [10-12]. For the CT specimen used, an analytical calibration equation, relating crack length to the ac potential, was not available, and a calibration relationship had to be established experimentally. Calibration was accomplished by making concurrent visual and electric potential measurements of crack lengths on specimens fatigued in air. The visual measurements were made from plastic replicas of the cracks taken from both specimen surfaces.

The experimental calibration results can be represented by Eqn. (3) as a least-squares-error fit to the crack length (a) versus the normalized potential (V*) data.

$$a = 15.9 + A_1V^* + A_2V^{*2} \qquad \text{(in mm)} \qquad (3)$$

where $V^* = (V-V_r)/V_r$, $V = V(a)$ = the potential corresponding to crack length a, and V_r = the reference potential corresponding to the initial notch. The coefficients A_1 and A_2 were determined experimentally for each specimen geometry.

Because of specimen to specimen variations, some deviations from this crack length-potential relationship were observed. Post fracture corrections to the empirical constants in Eqn. (3)

were made, therefore, for each specimen by using the average initial (precrack) and final crack lengths measured from the fatigue fracture surface markings. Accuracy of crack length measurement with the ac system, after this correction, was estimated to be better than 1 pct, for crack lengths from 18.5 to 44.5 mm (0.725 to 1.75 in.). The resolution was better than 0.025 mm (0.001 in) based on 12.5 nV resolution in electrical potential.

2.3 Fractography

Characterizations of the fracture surface morphology were made by scanning electron microscopy (SEM). Entire broken halves of the specimens were placed inside the microscope for examination. The specimens were tilted 15 degrees about an axis parallel to the direction of crack growth. In addition, the chemical compositon of particles found on the fracture surfaces was determined qualitatively with the aid of an EDX microprobe attached to the scanning electron microscope.

Micro-etch-pitting technique is a simple method for identifying the crystallographic orientation of a fracture surface, and has been used successfully in the study of mechanisms of fatigue crack growth. This technique has been utilized recently, in conjunction with TEM or STEM techniques, to make more detailed studies of fracture surfaces produced by fatigue in various environments [13], and is used here.

According to Nix et al. [13] and Pelloux [14], etching reagents, with the composition of 50% H_2O, 50% HNO_3, 32% HCl and 2% HF, and of 1.5% HCl, 2.5% HNO_3, and 0.5% HF by volume, would

preferentially attack the {100} planes, and produce well-defined etch pits. Fracture surfaces of 7075-T651 aluminum alloy produced by fatigue in air at room temperature with 42% relative humidity (or a partial pressure of water vapor of 1100 Pa) and in water vapor at a pressure of 67 Pa were studied using the etch pit method. The first of the etching reagents, with 50 H_2O, 50 HNO_3, 32 HCl, and 2 HF, was selected for use and an etching time of about 6 s was utilized.

2.4 Surface Reaction Kinetics

Auger electron spectroscopy (AES) was used to determine the kinetics of the reactions of water vapor with aluminum and magnesium alloy surfaces at room temperature. For AES analyses, clean surfaces were produced by in situ impact fracture of notched round specimens [11]. Exposures of these clean surfaces to water vapor were achieved by back-filling the spectrometer chamber from a high purity water source attached as a side arm to the spectrometer. Again, purification was achieved by alternately freezing and thawing triply distilled water, and pumping away the dissolved gases.

For the surface reaction studies, background pressure inside the spectrometer was typically 6.7 x 10^{-8} Pa (5 x 10^{-10} torr), as measured on an ionization gage. Water vapor was admitted into the chamber to pressures below 6.7 x 10^{-4} Pa (5 x 10^{-6} torr) to effect the desired exposure. The chamber was then re-evacuated to below 2.67 x 10^{-7} Pa (2 x 10^{-9} torr) prior to each analysis.

At these low pressures (below 1.33×10^{-4} Pa), reactions induced by species created by the ionization gage filament were minimal.

To minimize reactions and adsorption induced by the primary electron beam, and to minimize the variations in the observed amplitudes of Auger signals caused by differences in surface roughness, a large, fixed area of the sample surface was analyzed after each exposure. A primary electron beam of 5 keV energy at 10^{-6} A was used to excite the Auger transitions. Typically the electron beam was scanned over an area of 6.8×10^{-5} mm^2 during recording of an Auger spectrum. By using this procedure, it was possible to make AES analysis with a relatively low primary beam density of 1.5×10^{-6} A/mm^2. Even at this low primary electron beam current density, the primary beam was observed to induce reactions between residual water vapor and the aluminum alloy surfaces at a system pressure above about 1×10^{-6} Pa. This effect was minimized by operating the electron beam only when the pressures were reduced to below 2.6×10^{-7} Pa (2×10^{-9} torr), and by recording a complete Auger spectrum within 4 minutes (as compared with more than 8 minutes that were needed to change the scanning area after each exposure).

The extent of reactions of water vapor with the alloy surfaces was determined by measuring the oxygen Auger (510 eV) electron peak-to-peak height (APPH) as a function of exposure (pressure x time). To compare the results of several different experiments, the oxygen Auger electron signal (measured for constant instrumental parameters) was normalized with respect to the APPH of the aluminum (1396 eV) signal from a clean aluminum alloy

surface (for the aluminum alloys), or with the APPH of the magnesium (1186 eV) signal from a clean magnesium alloy surface (for the magnesium alloy).

3.0 RESULTS

3.1 Kinetics of Fatigue Crack Growth

The kinetics of fatigue crack growth in 7050-T7451, 7050-T651 and 7075-T651 (I/M) aluminum alloys and in 7091-T7E69 and 7091-T7E70 (P/M) aluminum alloys at room temperature have been determined, for a frequency of 5 Hz and a load ratio (R) of 0.1; and in selected cases for R = 0.5. Test environments included vacuum, pure argon, pure oxygen at 266 Pa, and pure water vapor (over a range of pressures from 0.13 to 1330 Pa, or 0.001 to 10 torr). Tests in argon and in oxygen were carried out to provide additional reference data and for comparison. To examine the possible role of oxygen in inhibiting the influence of water vapor on fatigue crack growth, tests were also conducted in oxygen-water vapor binary mixtures. A fixed water vapor partial pressure of 67 Pa (0.5 torr) was selected, while the oxygen partial pressure covered a range from 0.466 to 200 kPa (3.5 to 150 torr). Principal results from these tests are summarized separately for the I/M and P/M alloys in the following subsections. The effect of test temperature is considered in conjunction with the results on 7075-T651 alloy, and the influence of oxygen is described in a separate subsection.

3.1.1 7050-T7451 and 7050-T651 (I/M) Aluminum Alloys

The kinetics of fatigue crack growth have been determined for the 7050-T7451 alloy at room temperature. Two load ratios (R = 0.1 and 0.5) were used. Tests were carried out in vacuum ($<10^{-6}$ Pa), water vapor and distilled water at a loading frequency of 5 Hz. Data from the different tests are shown in Figs. 13

to 15, and trend lines (or least-squares regression lines) for the data are shown for R = 0.1 and R = 0.5 in Fig. 16. To examine the role of aging treatment and the effects of magnesium on fatigue crack growth, additional tests were carried out on this alloy in the peak-aged (T651) condition. Crack growth rate data on the 7050-T651 alloy are summarized in Fig. 17 as a function of water vapor pressure at two ΔK levels. Data on the 7050-T7451 alloy are also shown in Fig. 17 to demonstrate the effect of water vapor pressure and to provide for direct comparison.

These results indicate that water vapor/water produced less than a factor of two increase in the rate of fatigue crack growth, over that observed in vacuum, for the 7050-T7451 alloy. The initial increase in growth rate in the 7050-T651 alloy was comparable to the 7050-T7451 alloy. At water vapor pressures above about 67 Pa, however, there was approximately another factor of two increase in growth rate. The reason for this additional increase in rate is discussed in Section 4.0.

3.1.2 <u>7075-T651 (I/M) Aluminum Alloy</u>

3.1.2.1 Room Temperature (295K)

Fatigue crack growth data for 7075-T651 (I/M) aluminum alloy tested in vacuum, pure argon and pure oxygen, and in air (relative humidity = 42%) and distilled water are shown in Figs. 18 and 19, respectively. Data for tests in water vapor, for pressures ranging from 1.3 to 665 Pa, at R = 0.1 and R = 0.5 are shown in Figs.20 to 23. To facilitate comparisons, representative data for the "inert" environments and for water vapor at 1.3

and 2.0 Pa are shown in Fig. 24, and those for water vapor (including moist air) at R = 0.1 and 0.5 are shown in Figs. 25 and 26, respectively. The influence of water vapor on fatigue crack growth in this I/M alloy, at R = 0.1, is shown explicitly in Fig. 27 for two ΔK levels. Data in Figs. 18, 20 and 23 illustrate the reproducibility of these tests.

The results shown in Figs. 24, 25 and 27 indicate that the crack growth rates in vacuum and in argon were faster than those observed in pure water vapor at the lowest vapor pressures (1.3 and 2 Pa). The rates were also faster than those observed in oxygen. The crack growth rates in oxygen, however, were comparable to those in water vapor at 1.3 and 2 Pa. The reasons for the faster growth rates in vacuum and in argon are not yet fully understood. Fractographic results to be described later, however, do indicate a difference in the micromechanism for crack growth in vacuum and in argon from that in oxygen and low pressure water vapor. For the interpretation of data in terms of the model for transport controlled crack growth [1-3], it appears appropriate to use the data in pure oxygen as the reference rates, i.e., $(da/dN)_r$.

From Fig. 27 it is seen that at low water vapor pressures, fatigue crack growth rates are strongly dependent on pressure, and conform to the model for transport controlled crack growth as indicated by the solid lines in the figure. The "saturation" water vapor pressure is estimated to be about 4.7 Pa [2,3]. Above the saturation pressure, crack growth rates are essentially independent of water vapor pressure up to about 100 Pa.

At higher vapor pressures (above 600 Pa) and in liquid water, the crack growth rates exceeded those of the "saturation" level (see Fig. 27). The rates at 1.3 kPa and in distilled water are about twice higher than the "low pressure" saturation rates. The observed further increase in growth rate is consistent with the results reported by Dicus [15] for 7475-T651 aluminum alloy. Taken together, these results indicate that there might be a second transition in crack growth rate with water vapor pressure. The cause for this transition has been attributed now to a slower step in the reactions of water with the segregated magnesium in this alloy, and is discussed separately later.

3.1.2.2 "High" Temperature (354K)

To investigate the effect of temperature on fatigue crack growth response, crack growth measurements were made at 353 K (80 °C) in water vapor at pressures from 1.3 to 665 Pa, and in pure oxygen at 267 Pa. Data for the individual tests are shown in Figs. 28 to 31, and are summarized in Fig. 32. The crack growth response at 354 K is similar to that at room temperature (see Fig. 27). The crack growth rates increased with increasing water vapor pressure at low pressures, then became independent of pressure after a "saturation" pressure, of about 5.0 Pa, had been reached. The "saturation" pressure at 353 K is slightly higher than that for the room temperature tests. Unlike the response at room temperature, a second transition in crack growth with increasing water vapor pressure was not observed over the range of pressures from 1.3 to 670 Pa.

3.1.3 7091-T7E69 and 7091-T7E70 (P/M) Aluminum Alloys

Wedge-opening-load (WOL) specimens, with LT orientation, were used to determine the kinetics of fatigue crack growth in the 7091 (P/M) alloys. In the early tests, it was found that the fatigue crack deviated by more than 10 degrees from the plane of symmetry (or the intended crack plane) in about 50 pct of the cases. This large deviation rendered the test data invalid [9].

To alleviate this problem, face grooving of the specimens was employed. A face groove, with depth equal to 5 or 10 pct of the specimen thickness, was introduced into each face of the test specimen along the desired crack growth direction, and was found to be effective in confining the fatigue crack to the plane of symmetry. Fatigue data reported herein were obtained either from the face grooved specimens or from the ungrooved specimens that were deemed to be acceptable [9].

Representative fatigue crack growth data for 7091-T7E69 and 7091-T7E70 alloys tested in vacuum and in water vapor are shown in Figs. 33 and 34. (The data in Fig. 33 serve to illustrate the interlaboratory reproducibility of results.) Composite trend lines for these alloys are shown in Fig. 35. Comparison of Figs. 35a and 35b shows that fatigue crack growth rates are comparable for the 7091-T7E69 and 7091-T7E70 alloys, although the latter alloy was overaged for a longer period of time (14 h vs. 4 h). Depending on the ΔK level, enhancement of fatigue crack growth rates by water vapor is as much as a factor of 2 over that observed in vacuum.

The influence of water vapor pressure on the rate of fatigue crack growth in these alloys is shown more explicitly in Fig. 36 at three ΔK levels. Test data from both 7091-T7E69 and 7091-T7E70 alloys have been combined in this figure. It is seen, from Fig. 36, that fatigue crack growth rate started to increase when the water vapor pressure exceeded a threshold level of about 0.13 Pa. Above this threshold pressure, crack growth rate increased with increasing vapor pressure, and reached a maximum and then remained constant above a "saturation" pressure. The observed response is again consistent with the model for transport controlled fatigue crack growth [2,3]. The saturation pressure for the 7091 (I/M) alloys is estimated to be about 0.67 Pa, and the range of pressure over which fatigue crack growth rates remained essentially unchanged in this study extended from about 0.67 to 66.7 Pa.

3.1.4 Inhibition by Oxygen

To investigate the possible inhibiting effects of oxygen on the enhancement of fatigue crack growth by water vapor, crack growth measurements were made in binary mixtures of water vapor and oxygen for the 7075-T651 (I/M) alloy. The ratio of partial pressures of water vapor to oxygen was varied from 1:7 to 1:300, while the water vapor pressure was maintained constant at 67 Pa. A test was also carried out in air, at 42 pct relative humidity, to provide for comparison.

No inhibiting effect of oxygen was observed under these test conditions (see Fig. 37). These results are not in agreement with model predictions [3], and are at variance with convincing

evidence in support of the inhibition of crack growth by oxygen [16,17], at least for sustained loading. Plausible explanations for the observed response and additional studies are considered in Section 4.0.

Tests in mixtures of water vapor and oxygen were also carried out on 7091-T7E70 (P/M) alloy, with a fixed water vapor partial pressure of 67 Pa and water vapor to oxygen partial pressure ratios from 1:21 to 1:300. The test results are shown in Fig. 38. Again, in agreement with similar results on the 7075-T651 (I/M) alloy, there was no apparent inhibiting effect of oxygen under these test conditions. The implications of these results are also considered in Section 4.0.

3.2 Fractographic Analyses

To assist in understanding the role of metallurgical and chemical variables on environmentally assisted fatigue crack growth, fractographic analyses were performed on fatigue fracture surfaces of the 7050-T7451 and 7075-T651 (I/M) alloys, and of the 7091 (P/M) alloys. Principal attention was directed to the 7075-T651 (I/M) alloy. Systematic observations were made of the changes in fracture surface morphology as a function of water vapor pressure to assist in elucidating the mechanism for embrittlement. In addition, micro-etch-pit analysis was applied to the 7075-T651 alloy to assist in the identification of fracture planes. This information, along with fractographic data obtained from specimens tested in inert environments, serves as a basis for the formulation of a quantitative model for estimating the

rates of environmentally assisted fatigue, which would incorporate the significant chemical, metallurgical and mechanical variables. Fractographic results from the 7050-T7451, 7075-T651 and 7091 alloys are presented and discussed separately.

3.2.1 7050-T7451 (I/M) Alloy

Representative scanning electron (SEM) microfractographs from the fatigue crack growth specimens for R = 0.1 and R = 0.5, corresponding to a ΔK of 10 MPa$\sqrt{m}$, are shown in Figs. 39 and 40, respectively. These micrographs indicate the crack path to be transgranular, irrespective of the test environment.

The morphology of fracture surfaces for specimens tested in water vapor and distilled water are similar, but are different from that for specimens tested in vacuum. Fracture surfaces in vacuum (Figs. 39(a) and 40(a)) show evidence of ductile tearing and fatigue striations. Fracture surfaces of specimens tested in water vapor (Figs. 39(b,c) and 40(b)) and in water (Fig. 39(d)), on the other hand, are characterized by flat featureless regions, regions that contain "brittle" striations, and small areas of ductile tearing.

Comparisons of striation spacings on the microfractographs indicated little difference in the rate of fatigue crack growth for this alloy exposed to the different environments. This observation is consistent with the data on fatigue crack growth kinetics, which showed only a small effect of environment. These fractographic observations will be considered in relation to those for the 7075 (I/M) and 7091 (P/M) alloys.

3.2.2 7075-T651 (I/M) Alloy

Representative scanning electron (SEM) microfractographs taken from specimens tested in vacuum, pure oxygen and pure water vapor are shown in Figs. 41 to 52. Fractographs and stereo pairs from mating fracture surfaces were obtained to provide more detailed information on the fracture processes (see Figs. 42, 43, 44, 46, 51 and 52). Because the effect of water vapor pressure on fracture surface morphology is of special interest, particularly in the low pressure region where the crack growth rates are controlled by gas transport, microfractographs representing five different water vapor pressures (that is, 1.3, 2.7, 4.6, 67, and 665 Pa) have been included (see Figs. 47 to 50). Results from micro-etch-pit analyses of specimens tested in air (42% relative humidity) and in water vapor are shown in Figs. 53 to 55.

3.2.2.1 Fractographic Observations

Comparisons of Figs. 41 to 44 with Figs. 45 to 52 show that the morphology of fracture surface produced in vacuum is clearly different from those produced in pure oxygen and in water vapor. Figure 41 shows that the fracture surface is composed of regions that are associated with (constituent) particles and regions that appear relatively featureless at low magnifications. More detailed nature of the fracture surfaces may be seen in the SEM microfractographs and stereo pairs of the mating surfaces (Figs. 42 to 44).

A close match between mating surfaces is seen. Holes on one surface are closely matched to particles or protrusions on the other surface. Every ridge on the one surface has a correspon-

ding valley on the other. This correspondence indicates the "brittle nature" of fatigue cracking in 7075-T651 as compared to the more "ductile", void coalescence mode found in over-load fracture; where ridges correspond to ridges, and valleys to valleys. The featureless regions at low magnifications are actually composed of a large number of slip steps, which always exhibited striation-like features. Slip steps are more pronounced on one surface than the other (Figs. 42 to 44), and their spacings are much larger than those that would be indicated by the macro-crack growth rates. Extensive amounts of plastic deformation (ductile tearing), with "patch" steps, were also observed. The patch steps reflect a crack having passed through "patches" that were at different levels.

Representative SEM microfractographs for the specimen tested in 267 Pa pure oxygen are shown in Figs. 45 and 46. It can be seen that the fracture surface morphology of the specimen tested in oxygen is clearly different from that produced in vacuum, but is nearly identical to that of the specimen tested in 1.3 Pa water vapor; (compare Figs. 45 and 47). Instead of slip steps, the surface is composed principally of dense clusters of dimples that are associated with large constituent particles. Energy dispersive x-ray (EDAX) analyses showed that these particles are rich in iron and in copper. Regions of extensive plastic deformation (ductile tearing) and a small amount of flat featureless facets were also observed.

Because of the differences in fracture surface morphology and in crack growth rates between specimens tested in vacuum and those tested in oxygen and at the lowest water vapor pressure, there is reason to believe that the mechanism of fatigue cracking in vacuum is different. The reason for this difference is unclear, and may be associated with either the influence of surface oxides on slip (i.e., deformation) or local heating at the crack tip. It appears, therefore, that the fatigue crack growth rates in vacuum should not be used as a reference in evaluating the models for environmentally assisted crack growth.

The changes in surface morphology as a function of water vapor pressure are illustrated in Figs. 47 to 50. Figure 47 shows representative microfractographs taken from a specimen that had been tested in water vapor at 1.3 Pa and at 665 Pa. The micrographs clearly show two regions with completely different fracture surface morphology.

The fracture surface produced in 665 Pa water vapor (region A in Fig. 47(a), and Fig. 47(b)) is flat and appears to be brittle. The brittle nature of cracking in water vapor at the higher pressures is confirmed by stereo pairs of SEM microfractographs obtained from mating fracture surfaces of 7075-T651 alloy tested in 133 Pa water vapor (Figs. 27 and 52). Brittle striations or slip steps are clearly discernible in each of the mating surfaces, and the various microscopic facets are closely keyed with each other across the crack plane. The surface produced in 1.3 Pa water vapor (region B in Fig. 47(a), and Fig. 47(c)), on the other hand, appears to be rougher and more "ductile"; exhibiting

extensive amounts of ductile tearing and dimpled rupture. The surface produced at the lower pressure is comparable to that produced in pure oxygen. Because of the similarity in fracture surface morphology hence, micromechanism of cracking in crack growth rates for these two environments (pure oxygen and 1.3 Pa water vapor), it is reasonable to use pure oxygen as the reference environment for analyzing fatigue crack growth data in water vapor.

The marked contrast in microscopic fracture appearance of specimens tested in water vapor at 1.3 Pa and 665 Pa suggests the operation of at least two different micromechanisms, and provides a basis for the interpretation and correlation of fractographic data. As an initial effort, one may choose to identify the fracture morphology for 665 Pa water vapor (Fig. 47(b)) with the micromechanism for "pure" corrosion fatigue. The morphology shown by the tests in 1.3 Pa water vapor (Fig. 47(c)) and in pure oxygen is identified with "pure" mechanical fatigue.

Based on these premises, it can be seen clearly from Figs. 47 to 50 that the fraction of fracture surface created by "corrosion fatigue" increased rapidly as the water vapor pressure increased from 1.3 to 67 Pa, The fracture surface morphology of specimens tested at pressures higher than 4.7 Pa was essentially identical to that of specimens tested at 665 Pa; i.e., 100 pct by corrosion fatigue.

3.2.2.2 Micro-Etch-Pit Analyses

Figure 53 shows well-defined etch pits on the fatigue fracture surfaces of 7075-T651 alloy produced in air. The etch pits conform to that shown in the accompanying sketch with the side faces corresponding to {100} planes and the base to another (100) plane. The edges of the pit, or of the basal plane, are parallel to the <100> directions. For this case, the striations are parallel to the edges of the pits, which indicate that fatigue crack growth had occurred along a (100) plane and in the <100> direction.

Based on the examination of a large number of fatigue fracture surfaces of 7075-T651 aluminum alloy produced in air (RH = 42%) and in water vapor at 67 Pa, the following observations can be made:

(i) The fracture planes were predominantly of {100}.

(ii) The striations on these {100} planes were either parallel to <100> or approximately parallel to <110>, Figs. 54 and 55. The striation orientation, however, varied slightly from one adjacent subgrain to another.

(iii) Very small amounts of cracking along {110} planes, with striations aligned parallel to <111>, were also found.

These results, however, must be interpreted with care. The shape of the etch pits may or may not be the same between very slightly etched and well-etched surfaces. For well-etched fracture surfaces, the shape of etch pits is only related to the orientation of the main crack plane, whereas the etch pits on slightly etched surfaces would reflect the orientations of individual striations. It may be necessary, therefore, to examine the shape of etch pits at the early stage of etching, and couple the observations

with other techniques (such as transmission electron microscopy and sectioning) to better identify the micromechanisms of crack growth.

3.2.3 7091 (P/M) Alloy

Representative SEM microfractographs from 7091-T7E69 alloy tested in vacuum and in 13.3 Pa water vapor, at ΔK of 11 MPa$\sqrt{m}$, are compared in Fig. 56. Representative SEM microfractographs from 7091-T7E70 alloy tested in pure oxygen at 267 Pa, also at ΔK of 11 MPa$\sqrt{m}$, are shown in Fig. 57. These microfractographs indicate that the fracture path in all three environments is primary transgranular and is typical of high strength aluminum alloys fractured in fatigue. No clearly discernible fatigue striations can be found for any of the test environments.

The morphology of fracture surfaces for specimens tested in water vapor is different from that for specimens tested in vacuum and in oxygen. Fracture surfaces in vacuum and in oxygen exhibited finer features and more ductile tearing than those in water vapor. Regions showing the presence of constituent particles were also observed on the fracture surfaces exposed in oxygen, although the density and size of these particles are much smaller than those in the ingot-processed 7075-T651 alloy. Fracture surfaces of specimens tested in water vapor are characterized by many flat patches and smaller areas of ductile tearing. Some slip steps are discernible in the flat patches. This type of fracture surface morphology is a good indication that the fatigue crack had propagated through previously

"embrittled" zones, as envisioned in the proposed model for environmentally assisted fatigue crack growth.

3.2.4 Comparison between I/M and P/M Alloys

Comparisons of the SEM microfractographs for the 7075 (I/M) and 7091 (P/M) alloys, for the respective environments, show that, overall, the micromechanisms for fatigue crack growth are essentially similar. The constituent particles are smaller and far fewer in the powder processed alloy. Being much finer in grain (and subgrain) size, the detailed fracture surface features are much more difficult to discern in the P/M alloys, vis-à-vis, the I/M alloy.

A more direct comparison of the fracture surface morphology of powder-processed 7091-T7E69 and ingot-processed 7050-T7451 alloys is given in Fig. 58. Both specimens were tested in water vapor and the SEM microfractographs were taken from regions of fracture surfaces that correspond to a ΔK of 11 $MPa\sqrt{m}$.

Since fatigue crack propagated primarily along crystallographic planes in both 7091 (P/M) and 7050 (I/M) alloys, the crack path (hence, the fracture surface morphology) would be influenced strongly by the orientation and the size of the grains encountered by the crack. During fatigue, a crack that followed one set of slip bands in one grain (or subgrain) would be forced to continue on another set of slip bands and change orientation when it encountered the neighboring grain or subgrain boundary, thus forming a zig-zag crack path.

In the 7050-T7451 (I/M) alloy (Fig. 58(b)), this zig-zag crack pattern or macroscopic fracture surface roughness is much

more pronounced, when compared to the 7091-T7E69 (P/M) alloy, because of the much larger grain (or subgrain) size of the I/M alloy. As the crack follows the zig-zag path, it deviates locally from the plane of symmetry. As a result, the effective stress intensity factor at the crack tip is slightly reduced and thereby lowers the corresponding crack growth rate. The more pronounced zig-zag crack path in the large-grain 7050-T7451 (I/M) alloy may be partially responsible for the lower observed fatigue crack growth rates as compared to the 7091-T7E69 (P/M) alloy.

3.3 Surface Segregation and Surface Reaction Kinetics

As a part of the study of surface reaction kinetics, Auger analyses of impact fracture surfaces alloys used in this study were made. Auger mapping of impact fracture surfaces of the 7075-T651 alloy showed pronounced segregation of magnesium; an example of the extent of magnesium segregation is shown in Fig. 59. Quantitative AES analyses indicated that the maximum concentration of magnesium in the segregation area is about five times higher than the average concentration in the bulk [18]. This finding suggested that the surface reactions of water vapor with the segregated magnesium in this alloy may be important, and an AZ-31 (96Mg-3Al-1Zn, wt pct) magnesium alloy was added to the surface reaction and fatigue crack growth studies.

Typical Auger electron spectra from impact fracture surfaces of 7075-T651 aluminum alloy and AZ31 magnesium alloy, before and after exposure to water vapor, are shown in Figs. 60 to 63. Figures 60 and 62 were taken from the clean surfaces, and indi-

cate the presence of the principal alloying elements in the two alloys. Typical changes in these spectra after exposure to water vapor are shown in Figs. 61 and 63 for the 7075-T651 and AZ31 alloys, respectively. In these figures, peak-to-peak heights of the oxygen Auger (510 eV) transition signal may be taken as a measure of oxygen concentration*.

The kinetics of the reactions of water vapor with the clean surfaces of 7075-T651 and AZ31 alloys at room temperature are shown in terms of the normalized oxygen Auger peak intensities, or APPH, versus exposure in Figs. 64 and 65. The results showed that an initial saturation value was reached following an exposure of approximately 1.9×10^{-2} Pa-s (1.5×10^{-4} torr-s) for the 7075-T651 alloy and 1.3×10^{-2} Pa-s (1×10^{-4} torr-s) for the AZ31 alloy. Data on a 7075-T7351 alloy showed similar response and that an initial saturation value was reached at a comparable exposure of about 2.6×10^{-2} Pa-s (2.0×10^{-4} torr-s). The limited reactions with water vapor at the initial stage are consistent with previous results on a 2219-T851 aluminum alloy (see Fig. 66) [1].

It is significant to note that, beyond the initial saturation, there was an additional increase in the reaction of water

---

*This procedure is not strictly valid, because of the attenuation of Auger electrons by atoms in the overlayers (adsorbed layer or reaction products) [1,19]. For the initial stage of reactions (i.e., at low exposures), this effect is small and may be neglected. For higher exposures, however, signal attenuation needs to be considered. In addition, the change in the shape of aluminum and magnesium spectra reflects changes in the chemical state of the surface layers; (suggesting oxidation of the surface), and needs to be taken into consideration in quantifying the reaction kinetics.

vapor with all three alloys. This increase occurred at an exposure of about 1.3 Pa-s (1 x 10^{-2} torr-s). The reactions then continued to increase with increasing exposure up to the highest exposure applied to each alloy; namely, 19.9 Pa-s for 7075-T651, 13 Pa-s for 7075-T7351, and 60 Pa-s for AZ31.

A comparison of the aluminum Auger (68 eV) peak from the clean surface with the corresponding peak following 7.3 Pa-s (5.5 x 10^{-2} torr-s) exposure to water vapor is given in Fig. 61 for the 7075-T651 aluminum alloy. The change in the aluminum Auger (68 eV) peak is significant and suggests oxidation of the surface. No further noticeable changes in the aluminum Auger (68 eV) peak were observed for exposures above 7.3 Pa-s. Similar changes in this peak were observed also for the 7075-T7351 alloy.

For the AZ31 magnesium alloy, the magnesium Auger (45 eV) peak changed continuously with increased exposure to water vapor. The changed shape of this peak, following 60 Pa-s (4.45 torr-s) exposure to water vapor, Fig. 63, is similar to that reported by Davis, et al. [20] for bulk MgO, with a characteristic peak at about 32 eV. This change in peak shape indicates possibly the initiation of oxidation. Noticeable changes in the shape and intensity (or APPH) of the magnesium Auger (1186 eV) peak were also observed. The APPH of the magnesium (1186 eV) signal decreased quickly at first, became essentially constant with increasing exposure up to about 6.6 Pa-s, and then increased rapidly with further increases in exposure, (see Fig. 65). The significance of these observations is discussed later in connection with the influence of magnesium on fatigue crack growth response.

4.0 DISCUSSIONS

The results from this study have provided additional insight into the mechanisms of environmentally assisted fatigue crack growth in high-strength aluminum I/M and P/M alloys. These results also formed a basis for critical assessments of the models for environmentally assisted fatigue crack growth [2,3], and have led to refinements of these models. In addition, the role of magnesium in determining the corrosion fatigue (and stress corrosion) cracking susceptibilty of 7000 series (AlMgZn) alloys was identified. The implications of these results, and their impact on modeling and on understanding the role of alloying elements are discussed separately in the following subsections.

4.1 Comparison between I/M and P/M Alloys

Because the various portions of the fatigue crack growth experiments were carried out at two different laboratories (Lehigh and MDRL), it is important to assess inter-laboratory variability before comparison of data are made. Figure 33 shows the results of replicate fatigue crack growth tests in vacuum on 7091-T7E70 (P/M) alloy conducted at the two laboratories. Agreement between the results results indicates good inter-laboratory (i.e., between laboratories) reproducibility of data, using comparable but different systems and procedures [21,22]. An additional indication of reproducibility can be seen by comparing the test results for water vapor (obtained at MDRL) with those in the water vapor-oxygen mixture (obtained at Lehigh) in Fig. 35 and 38. Intra-laboratory (i.e., within laboratory) reproducibility

may be seen by replicate tests in several of the environmental conditions and alloys (see Figs. 18, 20 and 23). Based on these results, reproducibility of data was estimated to be within 10 pct between the two laboratories and within each laboratory. It is reasonable, therefore, to make direct and quantitative comparisons between the various data sets.

Comparison of Figs. 27 and 36 shows that the crack growth response of 7091 (P/M) alloys closely resembles that of 7075-T651 (I/M) alloy. The susceptibility of 7075-T651 alloy to moisture, as measured by the ratio between the "saturation" growth rate and the "reference" rate, however, is greater than that of the 7091 alloys. The difference in saturation pressures, at a given test frequency, between the alloys (4.7 vs. 0.67 Pa) cannot be fully accounted for by their differences in yield strength [2,3,23]. This difference may be attributed to differences in fracture surface roughness and is discussed in greater detail in Section 4.4.

A comparison between the crack growth kinetics for 7091-T7E69 (P/M) and 7050-T7451 (I/M) alloys, which contain similar major alloying elements, is shown in Fig. 67. It is seen that fatigue crack growth rates are faster in the P/M alloy for both water vapor and vacuum, particularly in the lower ΔK region. The faster growth rates in the powder processed 7091-T7E69 alloy are attributed to its finer grain/subgrain size, which reduces slip reversibility and produces less zig-zag in crack path. At high ΔK, the effect of grain size diminishes and the fatigue crack

growth rates in 7091-T7E69 alloy become comparable to those in 7050-T7451.

The apparent absence of inhibition of crack growth by oxygen in the binary water vapor-oxygen mixtures for both the I/M and P/M alloys is puzzling. An indication of this behavior was seen in the data of Bradshaw and Wheeler [24], particularly at the lower ΔK levels. A plausible explanation is that water vapor condenses at the crack tip and thereby effectively shields the crack tip from exposure to oxygen. This possibility needs to be tested by examining the crack growth response at lower water vapor partial pressures (that is, well below 67 Pa used in the present experiments) over the same range of partial pressure ratios. Another possibility is that the kinetics of reactions of oxygen and water vapor with the 7000 series alloys are considerably different from those of the 2000 series alloys [1], which may be associated in part with the reactions of segregated magnesium with water vapor (see Section 4.5). Additional surface chemistry experiments are needed to resolve these issues.

4.2 Reconsideration of the Superposition Model

Fractographic analyses of specimens tested during this study have confirmed that there are at least two concurrent micromechanisms in the corrosion fatigue process. The first, pure mechanical fatigue, may be represented by fatigue in pure oxygen for the 7075-T651 aluminum alloy. The second, a pure corrosion fatigue micromechanism, may be represented by fatigue in water vapor above the initial saturation pressure. The fraction of fracture surface created by "corrosion fatigue" increased rapidly as the

water vapor pressure was increased from 1.3 to 4.7 Pa. Measurements were made of the areal fraction of each component on the fracture surface as a function of water vapor. The results are shown as data points in Fig. 68.

A modification of the superposition model [25] for corrosion fatigue has been made to give explicit recognition to the fact that mechanical fatigue and corrosion fatigue can proceed by different micromechanisms and occur concurrently or in parallel [26]. The modified model [26] provided a firmer and more consistent basis for the interpretation of fractographic results, but is otherwise fully consistent with (that is, does not invalidate) the transport and surface reaction controlled models for fatigue crack growth [2,3,23].

In the original formulation, crack growth rate was assumed to be the sum of three terms [25]:

$$(da/dN)_e = (da/dN)_r + (da/dN)_{cf} + (da/dN)_{scc} \qquad (4)$$

The first two terms represent the contributions of mechanical fatigue and cycle-dependent corrosion fatigue, and the last term, the contribution of sustained-load growth or SCC. Because the first two processes occur concurrently or in parallel, simple summation of rates is not appropriate even though Eqn. (4) correctly represents the experimental data. The addition of the third term is appropriate, since SCC contribution is considered to be sequential. But, because SCC contribution is not important to the consideration of aluminum alloys in the LT and TL orien-

to the consideration of aluminum alloys in the LT and TL orientations, this term is not included in the subsequent discussions.

To give recognition to the concurrent processes, Eqn. (4) is rewritten into the following form:

$$(da/dN)_e = (da/dN)_r\ (1 - \phi) + (da/dN)^*_{cf,s}\ \phi \qquad (5)$$

$(da/dN)_r$ is the mechanical fatigue rate, $(da/dN)^*_{cf,s}$ is the "pure" corrosion fatigue rate, and ϕ is the fractional area of crack that is undergoing pure corrosion fatigue. In the limit, for $\phi = 0$ or for test in an inert environment, $(da/dN)_e = (da/dN)_r$, which corresponds to pure fatigue. For $\phi = 1$, corresponding to saturation [2,3], $(da/dN)_e = (da/dN)_{e,s} = (da/dN)^*_{cf,s}$ or the pure corrosion fatigue rate. By rearranging Eqn. (5) and recognizing the correspondence between ϕ and θ (the fractional surface coverage [2,3]), it is clear that the modified model is identical to the original version [25], where $[(da/dN)^*_{cf,s} - (da/dN)_r] = (da/dN)_{cf,s}$.

Modified: $$(da/dN)_e = (da/dN)_r + [(da/dN)^*_{cf,s} - (da/dN)_r]\phi \qquad (6)$$

Original: $$(da/dN)_e = (da/dN)_r + (da/dN)_{cf}$$
$$= (da/dN)_r + (da/dN)_{cf,s}\ \theta \qquad (7)$$

The relationship between the two models and the various terms are illustrated schematically in Fig. 69.

The implications of the modified model are that the partitioning of hydrogen to the various microstructural sites would not be uniform. The fractional area of fracture surface (ϕ) produced by pure corrosion fatigue would be equal to θ, and would

conform to one of the models for corrosion fatigue [2,3]. Statistically reliable experimental verification is difficult. Preliminary support for the proposed modification has been obtained from fractographic analyses of this 7075-T651 aluminum alloy; (compare model prediction, represented by the solid line, with the experimental observations in Fig. 68). Additional crack growth experiments and more detailed fractographic analyses are needed, however, to provide additional quantitative support.

4.3 Modeling of the Effect of Load Ratio

It was recognized early in this program that the possible influence of load ratio (R) on crack growth response had not been explicitly considered in the initial formulation of the model for transport-controlled fatigue crack growth [2,3]. Load ratio can affect gas transport to the crack tip through its influence on the effective crack opening and the effective length over which gas flow is restricted. A modification of the model for transport-controlled fatigue crack growth was proposed and has been tested using a 2219-T851 aluminum alloy [23].

In essence, the root-mean-squared (r.m.s.) value of the crack opening during each loading cycle and the cyclic plastic zone are used to scale the effective opening and flow length, in place of the corresponding quantities at maximum load used in the original formulation [2,3,23]. Because there is less constriction in gas flow at the higher load ratios (i.e., at higher mean loads), environmental effect is expected to extend down to lower pressures or exposures (pressure/frequency). In other words, the

so-called "saturation" exposure, $(p_o/2f)_s$, is expected to decrease with increasing R. The functional form of this dependence, for sinusoidally varying loads, is given by the following relationship [23]:

$$(p_o/2f)_s \propto [f(R)]^{-1} = \{0.25[((1+R)/(1-R))^2 + 0.5]\}^{-1} \qquad (8)$$

Data on 2219-T851 aluminum alloy tested in water vapor at room temperature provided support for this proposed relationship (see Fig. 70).

In formulating the model [2,3], it was assumed that the enhancement of fatigue crack growth resulted from embrittlement by hydrogen that was produced by the reactions of water vapor with the clean crack surfaces. Because the extent of reactions of water vapor with aluminum is limited, the extent of enhancement of fatigue crack growth would also be limited and would be independent of R at a given ΔK. Data on 2219-T851 also provided support for this corollary to the model [23]. Data on the 7075-T651 alloy are also in support of this corollary.

4.4 Critical Assessment of the Model for Tranport-Controlled Fatigue Crack Growth

Fatigue crack growth data obtained from this investigation cover a range of aluminum alloying with different yield strengths and microstructures, and can serve as a basis for making critical assessments of the model for environmentally assisted fatigue crack growth, such as the model for transport controlled crack growth [2,3,23]. In the model, enhancement of fatigue crack growth is assumed to result from embrittlement by hydrogen that

is produced by the reaction of water vapor with the freshly produced fatigue crack surfaces. The rate of reaction, and hence the extent of reaction and the amount of hydrogen production per cycle, is controlled by the rate of supply of water vapor to the crack tip.

By assuming that the transport of water vapor is by Knudsen (molecular) flow at low pressures, the corrosion fatigue component of crack growth rate, $(da/dN)_{cf}$, and the "saturation" exposure, $(p_o/2f)_s$, were obtained and are described by Eqns. (9) and (10), respectively [2,3,23].

$$\frac{(da/dN)_{cf}}{(da/dN)_{e,s}} \propto \frac{\beta^*}{\alpha} \frac{\sigma_{ys}^2}{N_o kTE^2} (T/M)^{1/2} (p_o/2f) \quad (9)$$

$$(p_o/2f)_s \propto \frac{\beta^*}{\alpha} \frac{N_o kTE^2 (M/T)^{1/2}}{\sigma_{ys}^2} \quad (10)$$

In Eqns. (9) and (10), f = cyclic load frequency; M = molecular weight of the gas; N_o = density of surface sites; p_o = pressure of the deleterious gas in the surrounding environment; k = the Boltzmann's constant; T = absolute temperature; E = Young's modulus; and σ_{ys} = yield strength. The constants α and β^* are empirical parameters for surface roughness and for flow, respectively [2,3,23]. The β^* parameter for flow depends on the geometry of the flow path and hence is expected also to be related to surface roughness. The precise dependence of β^* on surface roughness, however, is not known.

The influences of water vapor pressure (p_o) and frequency (f) on the fatigue crack growth rate as predicted by the model (Eqn. (9)) have been reasonably well established by experimentation [1,3,23,27,28]. A truly critical assessment of the model has not been made, and may be achieved by examining the predicted effects of yield strength and fracture-surface roughness (as affected by microstructure and environment) on the saturation exposure, defined through Eqn. (10). Specifically, Eqn. (10) shows that the value of the saturation exposure, $(p_o/2f)_s$, is proportional to the roughness related parameter, β^*/α, and is inversely proportional to the square of the yield strength. The yield strengths were determined from independent measurements, and the surface roughness of the fatigue fractured surfaces for each alloy was measured using a Tally Surf 4 profilometer. These data were used to determine the relative changes in $(p_o/2f)_s$ from one alloy to another.

For this assessment, data on the 7000 series I/M and P/M alloys are used. Comparisons of these alloys in terms of the influences of water vapor pressure on fatigue crack growth rates are shown in Figs. 71 to 74. Figures 71 to 73 show comparisons between a reference alloy, overaged 7050-T7451 (I/M) alloy, and the fatigue crack growth responses of 7091-T7E69 (P/M), peakaged 7050-T651 (I/M) and peakaged 7075-T651 (I/M) alloys, respectively. A comparison between the 7091 (P/M) alloys in the T7E69 and T7E70 conditions is shown in Fig. 74.

The general response for the different alloys is similar and can be divided into several regions as illustrated schematically in Fig. 75. In the low vapor pressure region (Region I), the rate of fatigue crack growth conforms to the model for transport controlled crack growth [2,3,23], and exhibits a saturation level (Region II). Above the saturation pressure, fatigue crack growth rates for the overaged alloys (7050-T7451, 7091-T7E69 and 7091-T7E70) remained essentially independent of water vapor pressure (Figs. 71 and 74). For the peakaged 7050-T651 and 7075-T651 alloys, however, there was a definite further increase in crack growth rate with increasing water vapor pressure above a certain pressure, reaching an apparent second plateau, or saturation level (Region III) (Figs. 72 and 73). The occurrence of Region III growth in the peakaged 7000 series alloys is attributed to the segregation of magnesium at the fracture surface and is discussed in Section 4.5 and [29].

It is important to note the significant difference in saturation vapor pressure at the onset of Region II among the different alloys. Figure 71 shows that the saturation vapor pressure for the 7091-T7E69 (P/M) alloy is less than one-tenth of that for the 7050-T7451 (I/M) alloy. The difference in saturation vapor pressure between the 7000 series (I/M) aluminum alloys is significantly less, and is negligible between the 7091-T7E69 and 7091-T7E70 (P/M) alloys. For transport-controlled crack growth, the saturation exposure, $(p_o/2f)_s$, is given by Eqn. (10). Since the 7000 series aluminum alloys have comparable Young's

moduli, the saturation water vapor pressures for two alloys, at the same test frequency and temperature, are related as follows:

$$(p_o)s_2 \cong \frac{(\beta^*/\alpha)_1 \ \sigma^2_{ys1}}{(\beta^*/\alpha)_2 \ \sigma^2_{ys2}}(p_o)s_1 \qquad (11)$$

Subscripts 1 and 2 denote the values for alloys 1 and 2, respectively. Thus, the saturation water vapor pressure of alloy 2 can be predicted from that of alloy 1, if the yield strength and the roughness-related term β^*/α for both alloys are known.

The roughness of fatigue fracture surfaces of the 7000 series aluminum alloys, tested at or above the saturation water vapor pressure, was measured using a Tally Surf 4 profilometer. The average fracture surface roughness for these alloys are listed in Table 2, along with the measured and predicted saturation pressure and the alloy yield strength. The results indicate very good agreement between the measured and predicted values of saturation pressure, provided that the roughness related parameter, β^*/α, is assumed to be directly proportional to surface roughness. For the 7050 and 7091 alloys, whose fracture surface roughness were essentially unaffected by the two different aging treatments, the saturation pressures reflected correctly the influence of yield strength. For 7050-T651 and 7091-T7E69, at comparable yield strength, the saturation pressure reflected the linear dependence on surface roughness. The other alloy combinations, correctly reflected in combined effects of roughness and yield strength. Data on the 7075-T851 at room temperature

(295 K) and at 354 K confirm the predicted effect of temperature, including that associated with the temperature related change in yield strength.

Quantitatively, it is unclear why β^*/α should vary directly with surface roughness. The constant α is modeled as an empirical constant for surface roughness and is related to surface roughness through increases in surface area. The overall effect, however, would result in a relatively small change in saturation pressure (about 30%). The constant β^* is a composite empirical flow parameter, which depends the effective crack opening and flow length. It is strongly dependent on the geometry of the flow path and is surface roughness related. Rougher fracture surfaces mean greater crack surface area (hence more surface reaction sites) and appear to provide more severe constriction in flow (slower water vapor transport rate to the crack tip), and result in higher saturation water vapor pressures. A more detailed study is required to fully understand the complex role of surface roughness in influencing environmentally assisted fatigue crack growth response.

The foregoing discussion dealt specifically and solely with the changes in fatigue crack growth rate when the environmental conditions are altered. The model, however, does not address the significant differences in the absolute fatigue crack growth rates and in response among the different alloys. For example, the powder metallurgy 7091-T7E69 alloy exhibited higher fatigue crack growth rates than the ingot metallurgy 7050-T7451 alloy at the same ΔK level (Fig. 71). While aging treatment produced

little effect on the Region I and Region II fatigue crack growth rate in the 7050 alloy, the peakaged 7050-T651 alloy exhibited Region III behavior and had higher fatigue crack growth rate at the higher exposures (see Fig. 72). Peakaged 7075-T651 alloy also had higher fatigue crack growth rates than the overaged 7050-T7451 alloy, Fig. 73. The crack growth rates in Region I and II are believed to depend on a number of metallurgical parameters; such as strength, toughness, microstructure, deformation mode, and texture. Because of the complex nature of the fatigue process, there is no accepted theoretical or empirical model that can quantitatively predict the absolute fatigue crack growth rate. The development of such a model is needed, but is beyond the scope of this study.

4.5 Role of Magnesium in Corrosion Fatigue

As a part of this study, the kinetics of fatigue crack growth of 7000 series I/M and P/M aluminum alloys were determined as a function of water vapor pressure or equivalent exposure ($p_o/2f$); (see Section 3.1). The reactions of water vapor with these alloys were also determined as a function of exposure (Section 3.3). Correlations between the fatigue crack growth and surface reaction results were made in terms of a model for transport-controlled crack growth proposed by Weir et al. [2] and Wei and Simmons [3].

Unlike the previous results on 2219-T851 (AlCu) alloy [1], 7075-T651 (AlMgZn) alloy exhibited further increases in fatigue crack growth rate beyond an initial "saturation" level with

increasing water vapor pressure or exposure (beginning at about 40 Pa or 4 Pa-s) as shown in Figs. 75 (to facilitate comparison, fatigue crack growth data on the 7075-T651 alloy, shown in Fig. 73, have been replotted in semi-logarithmic coordinates in Fig. 75). The response is similar to that reported by Dicus [15] for 7475-T651 alloy. Comparable increases in rates, however, were not observed on the overaged and 7091 (P/M) alloys. Analyses of impact-fracture surfaces of these alloys by Auger electron spectroscopy showed significant segregation (or enrichment) of magnesium over regions of the surfaces for the 7075-T651 (I/M) alloy (Fig. 59), and no apparent segregation in the overaged 7091 (P/M) alloys. Segregation of magnesium in peak-aged aluminum alloys has been reported by Pickens et al. [30].

These observations suggested that the commonly acknowledged environmental susceptibilty of 7000 series alloys in the peak-aged condition [16] might be attributed to further reactions of water vapor with the segregated magnesium or with magnesium in the enriched regions. Further Auger measurements of the reactions of water vapor with the 7075-T651 alloy, to include higher exposures (up to 15 Pa-s), and surface reaction and fatigue crack growth experiments on an AZ31 magnesium alloy were added to the original program to explore this possibility, and the surface reaction results are described in Section 3.3 and are shown in Figs. 64 and 65, respectively. The data have been normalized to the level in the intermediate plateau region. Surface reaction data for the 2219-T851 alloy [1,29] are shown in Fig. 66 for comparison.

Figure 64 shows clearly further increases in reaction of 7075-T651 aluminum alloy with water vapor, beginning at about 1 Pa-s. A similar increase is observed for the AZ31 magnesium alloy at about the same exposure (compare Fig. 65 to Fig. 64). On the other hand, there was no apparent increase in reactions with the 2219-T851 aluminum alloy (Fig. 66) at comparable exposures. These results strongly suggested that the additional reactions in the 7075-T651 alloy are associated with the presence of magnesium on the fracture surfaces.

Fatigue crack growth data for the AZ31 magnesium alloy are shown in Fig. 76. The results show an additional increment of increase in crack growth rate over the same range of pressures or exposures as that observed on the 7075-T651 alloy. Comparisons between the surface reaction data with the results on fatigue crack growth (Figs. 64, 65, 75 and 76) show that the increases in reaction occurred in the same range of exposures as that for the observed increases in fatigue crack growth rates (i.e., from about 1 to 10 Pa-s). No such increase in the extent of surface reaction or in fatigue crack growth rate was observed in the 2219-T851 (Al-Cu) alloy [1,29].

To further verify the role of magnesium in enhancing fatigue crack growth, additional experiments were carried out on a 7050-T651 alloy. The results (Fig. 72) clearly show the similarity in response between the peakaged 7050-T651 and 7075-T651 alloys. These results strongly suggest that the additional enhancement in fatigue crack growth rate and the further reactions in the peak-

aged 7000 series alloys are associated with the presence of magnesium on the fracture surfaces. The observed increases in fatigue crack growth rates in the 7050-T651 and 7075-T651 aluminum alloys (i.e., from about 1 to 10 Pa-s), in Fig. 72 and 75, are to be attributed to the reactions of water vapor with this magnesium. Limited information in the literature [31] suggests that the reactions of interest are likely to be the initial formation of $Mg(OH)_2$ and the subsequent formation of MgO. More complete studies are needed, however, to fully confirm these findings.

Although segregation of magnesium has been reported recently by Pickens et al. [30], it is believed that the data presented herein are the first evidence that link magnesium chemically to the corrosion fatigue and stress corrosion cracking susceptibility of 7000 series (AlMgZn and AlMgZnCu) alloys.

This explanation based on magnesium, however, is not wholly adequate, because 7075 aluminum alloy in the overaged (T73) condition showed magnesium segregation and enhanced reactions at the higher exposures. Yet no additional increases in fatigue growth rates were observed. It is apparent, therefore, that the presence of segregated magnesium and its reactions with water vapor provided a source of additional hydrogen for crack growth enhancement. While necessary, the availability of additional hydrogen is not sufficient in itself to produce embrittlement. The susceptibility of the microstructure needs to be considered also. Further work to examine the interactions of hydrogen and

microstructure is needed, and the possible contribution of zinc to the reactions with water vapor also needs to be clarified.

Although further research is needed to explore more fully the chemical role of magnesium in the susceptibility of 7000 series aluminum alloys, clearly its presence as a necessary condition for this susceptibility has been demonstrated. Efforts should now be made to capitalize on this important new finding in the development of improved alloys.

5.0 SUMMARY

The influence of water vapor on the kinetics of fatigue crack growth has been systematically determined for 7050-T7451, 7050-T651 and 7075-T651 (I/M) and 7091-T7E69 and 7091-T7E70 (P/M) aluminum alloys. The possible influence of oxygen in inhibiting the enhancement of fatigue crack growth by water vapor was also examined. Detailed fractographic analyses were performed on these alloys to provide information on the micromechanisms of corrosion fatigue crack growth and on the role of metallurgical variables. Surface chemistry studies were carried out to develop further understanding of the influence of water vapor on fatigue crack growth in aluminum alloys. The study has provided significant additional understanding and has led to improvements in the modeling of environmentally assisted fatigue crack growth.

Fatigue crack growth responses of the 7091 (P/M) alloys and of the 7000 series (I/M) alloys in water vapor are similar, although the behavior for the peakaged (T6) alloys differs somewhat from the overaged (T7) alloys. In the low pressure region, crack growth rate increased with water vapor pressure, for all of the alloys, up to some critical (or "saturation") pressure. The rate then remained essentially constant with further increases in pressure of the overaged (T7) alloys. For the peakaged (T6) alloys, on the other hand, there were additional increases in rate with further increases in pressure above a certain value.

The low-pressure region response for all alloys could be quantitatively described by a model of transport controlled crack growth, which in turn provided confirmation for the adequacy of

the proposed model for a range of aluminum alloys with differing composition and microstructure. The mechanism for crack growth enhancement in the second region, however, is less clear. Fatigue crack growth and surface chemistry studies carried out on the aluminum alloys and an AZ31 magnesium alloy showed clearly that the enhancement in growth is attributable to the further reactions of water vapor with segregated magnesium in this alloy.

Fractographic examinations suggested that the crack growth mechanism in oxygen and at low water vapor pressures may be different from that in vacuum for these aluminum alloys. The fracture surface morphology, typified by that of the 7075-T651 (I/M) alloy, varied continuously as water vapor pressure was increased. At low water vapor pressures and in oxygen, the fracture surfaces of 7075-T651 alloy contained dense clusters of dimples, associated with large constituent particles, and regions of extensive deformation. At the higher water vapor pressures, the fracture surfaces were essentially brittle. Stereographic analyses of the mating surfaces of 7075-T651 alloy indicate the close match between the surfaces and the limited extent of (ductile) deformation on the gross scale. Micro-etch-pit analyses showed that the fatigue fracture surfaces were predominately {100}, with striations parallel to approximately the <100> and <110> directions. The fracture surface morphology of the P/M alloys are similar to that of the I/M alloys, but on a much finer scale. The observed higher fatigue crack growth rates in the 7091 (P/M) alloys, as compared to those in the I/M alloys over

the low and intermediate ΔK range, is attributed to the effects of grain size on slip reversal and on fracture surface roughness.

Based in part on these fractographic observations, a modification of the superposition model for corrosion fatigue has been made to give explicit recognition to the fact that mechanical fatigue and corrosion fatigue can proceed by different micromechanisms and in parallel. Fractographic data, principally on the 7075-T651 alloy, from this study provided support this modification. In addition, revision of the model for transport controlled fatigue crack growth was made to account for the changes in effective crack opening with load ratio.

Data from this study permitted a critical assessment of the model for transport controlled crack growth through an examination of the effects of yield strength and fracture surface roughness. Both were found to be significant parameters in influencing the fatigue crack growth response of 7000 series P/M and I/M aluminum alloys in relation to water vapor pressure. The saturation water vapor pressure was found to vary inversely with the second-power of yield strength and directly with the fracture surface roughness, and is consistent with the model predictions. Because the yield strength of 7000 series aluminum alloys ranged between 400 to 600 MPa, its effect on the saturation water vapor pressure was relatively small. Fracture surface roughness, on the other hand, had a strong influence; changing the saturation water vapor pressure by more than an order-of-magnitude between selected powder metallurgy alloys, with their very fine microstructure and smooth fracture surfaces, and the coarser and

rougher ingot metallurgy alloys. Peakaged 7000 series aluminum alloys tended to have slightly lower saturation water vapor pressure because of their higher yield strengths. The transport-controlled model for fatigue crack growth and its applicability to high strength aluminum alloys have been demonstrated.

Identification of the chemical role of magnesium in corrosion fatigue and stress corrosion cracking susceptibility of 7000 series (Al-Mg-Zn and Al-Mg-Zn-Cu) alloys represents one of the key findings of this study. The evidence, although limited, strongly supports the further reactions of magnesium with water as being the cause for environmental cracking (CF and SCC) susceptibility of 7000 series aluminum alloys. This explanation is very different from the current hypotheses that are based solely on deformation (e.g., slip planarity), and opens up new avenues for improving the environmental cracking resistance of high strength aluminum alloys.

For a water vapor partial pressure of 67 Pa (with a load ratio of 0.1), oxygen appeared to exert no inhibiting effect on fatigue crack growth in the 7075-T651 and 7091 aluminum alloys for oxygen-water vapor partial pressure ratios from 4 to 300. This apparent disagreement with expectation and model prediction is probably caused by capillary condensation of water vapor at the crack tip, thereby preventing access by oxygen, of by the influence of magnesium. Additional research is needed to fully resolve this issue.

6.0 REFERENCES

1. R. P. Wei, P. S. Pao, R. G. Hart, T. W. Weir, and G. W. Simmons, Met. Trans. A, 11A, 151-158 (Jan., 1980).

2. T. W. Weir, R. G. Hart, G. W. Simmons, and R. P. Wei, Scripta Met., 14, 357-364 (1980).

3. R. P. Wei and G. W. Simmons, in FATIGUE: Environment and Temperature Effects, John J. Burke and Volker Weiss, eds., Sagamore Army Materials Research Conference Proceedings, 27, 59-70 (1983).

4. "Wrought P/M Alloys - A Balance of Properties For Demanding Aerospace Application", ALCOA, p. 4.

5. "Aluminum Standards and Data", Aluminum Assoc., Inc., pp. 15 and 111 (1979).

6. R. P. Wei and P. S. Pao, "Mechanisms of Corrosion Fatigue in High Strength I/M and P/M Aluminum Alloys", Air Force Office of Scientific Research, Technical Report No. 1 (First Annual Report) (January 1982).

7. J. Gjønnes and Chr. J. Simensen, Acta Metallurgica, 18, 881-890 (1970).

8. ALCOA Test Data on X7091-T7E69 alloy (Lot G86176-A1) and X7091-T7E70 alloy (Lot G86515-A1).

9. ASTM E647-81, Standard Test Method for Constant-Load-Amplitude Fatigue Crack Growth Rates Above 10^{-8} m/cycle.

10. H. H. Johnson, Mater. Res. & Stand., 5, 422 (1965).

11. Che-Yu Li and R. P. Wei, Mater. Res. & Stand., 6, 392 (1966).

12. R. P. Wei and R. L. Brazill, in Fatigue Crack Growth Measurement and Data Analysis, ASTM STP 738, S. J. Hudak and R. J. Bucci, eds., Am. Soc. Testing & Matls., Philadelphia, PA, p. 103 (1981).

13. K. J. Nix and H. M. Flower, Acta. Met., 30, 1549, (1982).

14. R. M. N. Pelloux, Trans. Am. Soc. Metals, 62, 281 (1975).

15. Dicus, Dennis L., NASA Technical Memorandum 84477 (May 1982).

16. M. O. Speidel, in The Theory of Stress Corrosion Cracking in Alloys, ed. J. C. Scully, NATO, Brussels, 289 (1971).

17. R. P. Wei, in Hydrogen Effects in Metals, I. M. Bernstein and Anthony W. Thompson, eds., The Metallurgical Society of AIME, Warrendale, PA 15086, 677-690 (1981).

18. M. Gao, R. P. Wei and G. W. Simmons, unpublished results, (1983).

19. G. W. Simmons, Lehigh University, unpublished results (1982).

20. L. E. Davis, N. C. MacDonald, P. W. Palmberg, G. E. Riach and R. E. Weber, "Handbook of Auger Spectrocopy", Physical Electronics Industries, Inc. (1976).

21. J. Mandel, Standardization News, STDNA, 5, No. 3, 17, (1977).

22. J. T. Fong and N. E. Dowling, in Fatigue Crack Growth Measurements and Data Analysis, S. J. Hudak, Jr. and R. Bucci, eds., ASTM STP 738, 171 (1981).

23. True-Hwa Shih and R. P. Wei, Engr. Fract. Mech., 18, 827 (1983).

24. F. J. Bradshaw and C. Wheeler, Intl. J. Fract. Mech., 5, 255 (1969).

25. R. P. Wei, in Fatigue Mechanisms, Proceedings of an ASTM-NBS-NSF Symposium, Kansas City, MO, May 1978, J. T. Fong, ed., ASTM STP 675, American Society for Testing and Materials, 816-840 (1979).

26. R. P. Wei and Ming Gao, Scripta Met., 17, pp. 959-962, 1983.

27. S. J. Gao, G. W. Simmons and R. P. Wei, Matls. Sci. & Engr., 62, pp. 65-78, 1984.

28. R. Brazill, G. W. Simmons, and R. P. Wei, J. Eng. Mater. Techn., 1979, vol. 101, p. 199.

29. R. P. Wei, Ming Gao and P. S. Pao, Scripta Met., 18, pp. 1195-1198, 1984.

30. J. R. Pickens, T. J. Langan, C. D. Davis, L. Christodoulou and L. Struble, "The Delayed Fracture of Aluminum Alloys", Rept. MML TR 83-11c, Martin Marrietta Laboratories, Baltimore, MD (Mar. 1983).

31. S. Affrossman, Surface Sci., 49, 61-76 (1975).

7.0 DEGREES, PRESENTATIONS AND PUBLICATIONS

Degrees Granted

True-Hwa Shih, M. S. in Applied Mechanic, Lehigh University, Bethlehem, Pa, 1981.

Ming Gao, Ph. D. in Metallurgy and Materials Engineering, Lehigh University, Bethlehem, Pa., 1983.

Presentations

"Reconsideration of the Superposition Model For Environmentally Assisted Fatigue Crack Growth", R. P. Wei and M. Gao, presentation at the 1983 TMS-AIME Annual Meeting, Atlanta, GA, March 7, 1983.

"Influence of Water Vapor on Fatigue Crack Growth in 7075-T651 Aluminum Alloy: Kinetics and Fracture Morphology", M. Gao, P. S. Pao and R. P. Wei, presentation at the 1983 TMS-AIME Annual Meeting, Atlanta, GA, March 7, 1983.

"Environmentally Assisted Fatigue Crack Growth in I/M and P/M Aluminum Alloys", R. P. Wei, P. S. Pao and M. Gao, presentation at the 1983 TMS-AIME Annual Meeting, Atlanta, GA, March 7, 1983.

"Synergism of Mechanics, Mechanisms and Microstructure in Environmentally Assisted Crack Growth", R. P. Wei, Annual Meeting of TMS-AIME, Los Angeles, CA, February 27, 1984.

"Role of Micromechanism in Corrosion Fatigue Crack Growth in a 7075-T651 Aluminum Alloy", R. P. Wei, Annual Meeting of TMS-AIME, Los Angeles, CA, February 27, 1984.

"Environmentally Assisted Fatigue-Crack Growth in 7075 and 7050 Aluminum Alloys, P. S. Pao, M. Gao and R. P. Wei, Annual Meeting of TMS-AIME, Los Angeles, CA, February 27, 1984.

"Critical Assessment of the Model for Transport-Controlled Fatigue Crack Growth", P. S. Pao, Ming Gao and R. P. Wei, International Symposium on Fundamental Questions and Critical Experimentson Fatigue, DFW Airport, TX, October 18-23, 1984.

"Environment-Assisted Fatigue Crack Growth Behavior of Structural Aluminum Alloys", P. S. Pao and R. P. Wei, Fall Meeting of TMS-AIME, Detroit, MI, September 16-20, 1984.

Publications

R. P. Wei and P. S. Pao, "Mechanisms of Corrosion Fatigue In High Strength I/M and P/M Alloys", Technical Report No. 1, Contract No. F49620-81-K-0004, Lehigh University, Bethlehem, PA, January, 1982.

R. P. Wei and P. S. Pao, "Mechanisms of Corrosion Fatigue in High Strength I/M and P/M Alloys", Technical Report No. 2, Contract No. F49620-81-K-0004, Lehigh University, Bethlehem, PA, February, 1983.

True-Hwa Shih and R. P. Wei, "The Effects of Load Ratio on Environmentally Assisted Fatigue Crack Growth", J. Eng. Fract. Mech., 18, pp. 827-837, 1983.

R. P. Wei and Ming Gao, "Reconsideration of the Superposition Model for Environmentally Assisted Fatigue Crack Growth", Scripta Met., 17, pp. 959-962, 1983.

R. P. Wei, Ming Gao and P. S. Pao, "The Role of Magnesium in CF and SCC of 7000 Series Aluminum Alloys", Scripta Met., 18, pp. 1195-1198, 1984.

M. Gao, P. S. Pao and R. P. Wei, "Role of Micromechanism in Corrosion Fatigue Crack Growth in a 7075-T651 Aluminum Alloy", in Proceedings of Conference on Fracture: Interactions of Microstructure, Mechanisms and Mechanics, TMS-AIME, Warrendale, PA (to be published) 1984.

P. S. Pao, M. Gao and R. P. Wei, "Environmentally Assisted Fatigue-Crack Growth in 7075 and 7050 Aluminum Alloys", Scripta Met. (to be published) 1984.

P. S. Pao, Ming Gao and R. P. Wei. "Critical Assessment of the Model for Transport-Controlled Fatigue Crack Growth", Proceedings of International Symposium on Fundamental Questions and Critical Experiments on Fatigue, Dallas, TX, October 18-23, 1984, (to be published).

R. P. Wei and P. S. Pao, "Mechanisms of Corrosion Fatigue in High Strength I/M and P/M Aluminum Alloys", Final Technical Report, Contract No. F49620-81-K-0004, Lehigh University, November, 1984.

Papers Being Prepared

"The Chemical Role of Magnesium in Corrosion Fatigue of 7000 Series Aluminum Alloys", M. Gao, P. S. Pao and R. P. Wei.

"Comparison of Corrosion Fatigue Response of 7000 Series I/M and P/M Aluminum Alloys", P. S. Pao, M. Gao and R. P. Wei.

"Mechanism of Environmentally Assisted Fatigue Crack Growth in 7075-T651 Aluminum Alloy", M. Gao, P. S. Pao and R. P. Wei.

Table 1

Chemical Composition and Mechanical Properties of 7091, 7050, and 7075 Aluminum Alloys [4-6,8]

(a) Chemical composition (wt pct)

Alloy	Zn	Mg	Cu	Zr	Cr	Mn	Co	Ti	Fe	Si	O	Al
P/M 7091	5.6-6.9	2.0-3.0	1.1-1.8				0.3-0.5		0.15 (Max)	0.12 (Max)	0.2-0.5	Bal
I/M 7050	5.95	2.04	2.41	0.1	0.018	0.016		0.041	0.1	0.07		Bal
I/M 7075	5.1-6.1	2.1-2.9	1.2-2.0		0.18-0.28	0.3		0.2	0.5	0.4		Bal

(b) Mechanical properties

Alloy	Yield Strength MPa(ksi)	Yield Strength MPa(ksi)	Elongation pct	Young's Modulus (GPa)	K_{Ic} MPa$\sqrt{m}$ ksi$\sqrt{in.}$
P/M 7091-T7E69	563(81.7)	622(90.2)	11.5	71	47.9(43.5)
P/M 7091-T7E70	508(73.7)	566(82.1)	14.0	71	58.7(53.4)*
I/M 7050-T7451	456(66.2)	515(74.8)	14.2	71	42.0(38.2)*
I/M 7075-T651	469(68)	538(78)	7.0	72	29.7(27.0)

*Fracture toughness does not satisfy plane strain criterion.

Table 2

Measured and Predicted Saturation Vapor Pressure

Material	Yield strength (MPa)	Fracture surface roughness (μm)	Measured saturation pressure (Pa)	Predicted saturation pressure (Pa)
7050-T7451	456	8.9	8.0	—
7050-T651	561	10.2	5.3	6.0
7075-T651	469	2.9	2.9	2.5
7091-T7E69	563	1.5	0.67	0.88

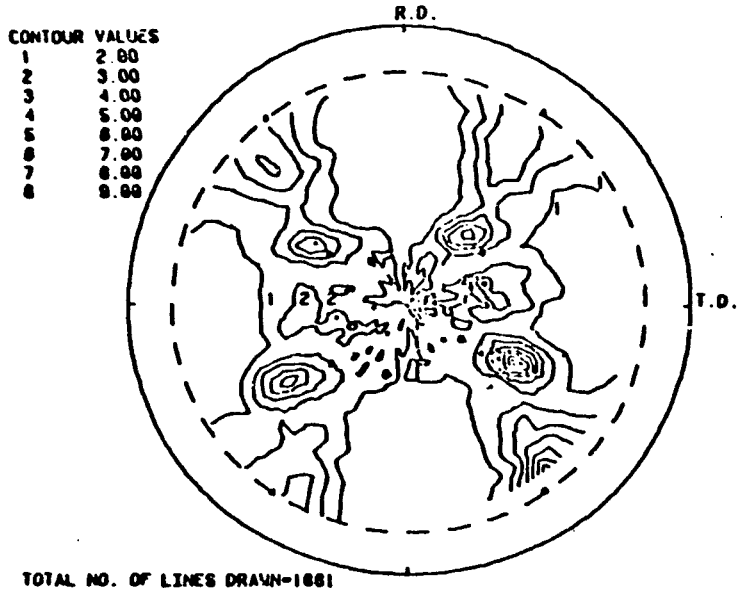

(a) (200) poles

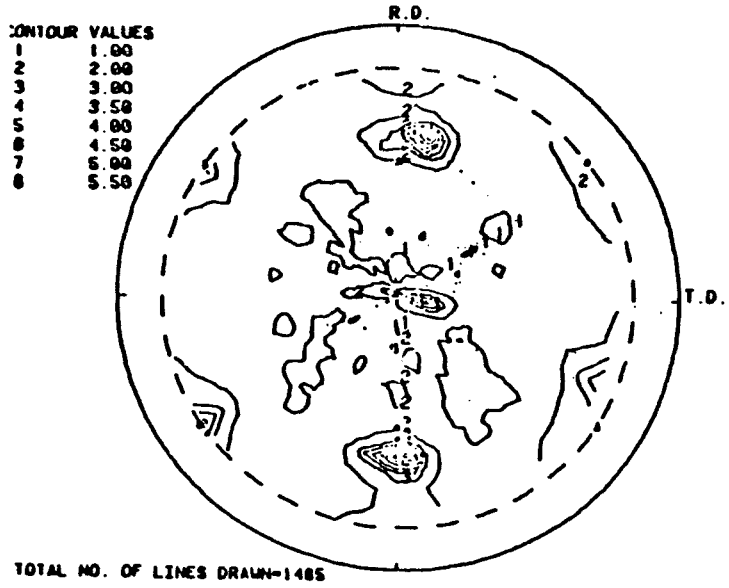

(b) (220) poles

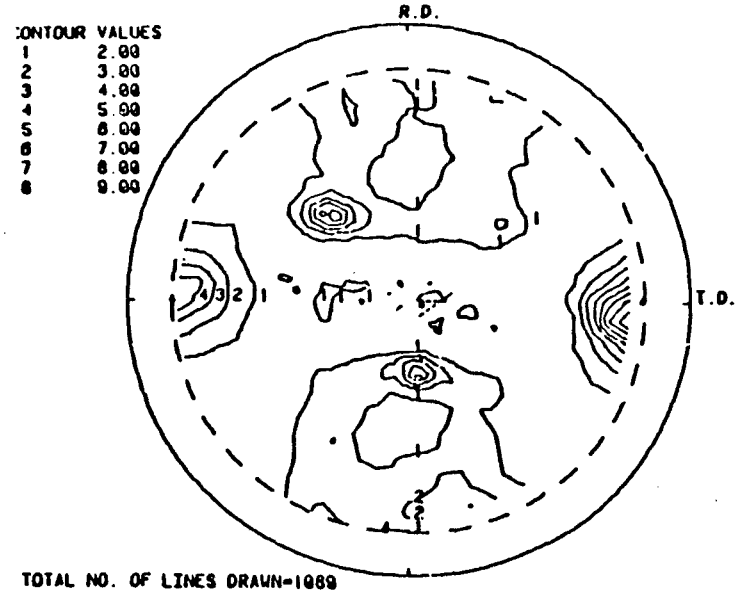

(c) (111) poles

Fig. 1: Pole figures for the rolling plane of 7050-T7451 aluminum alloy plate taken at the plate surface: (a) (200); (b) (220), and (c) (111).

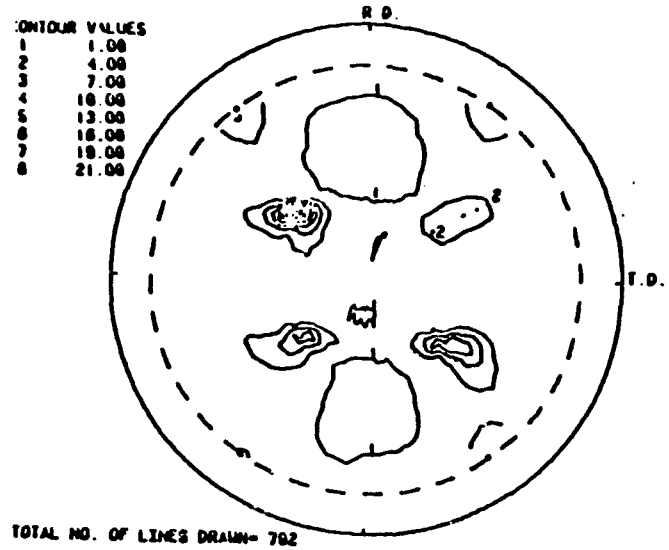

(a) (200) poles

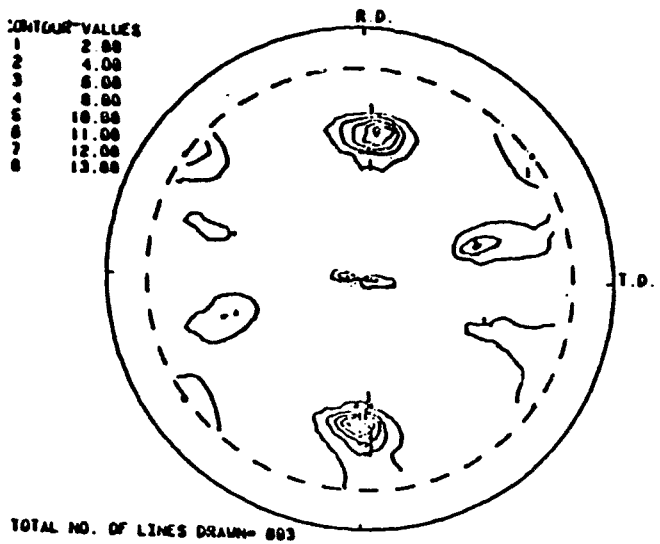

(b) (220) poles

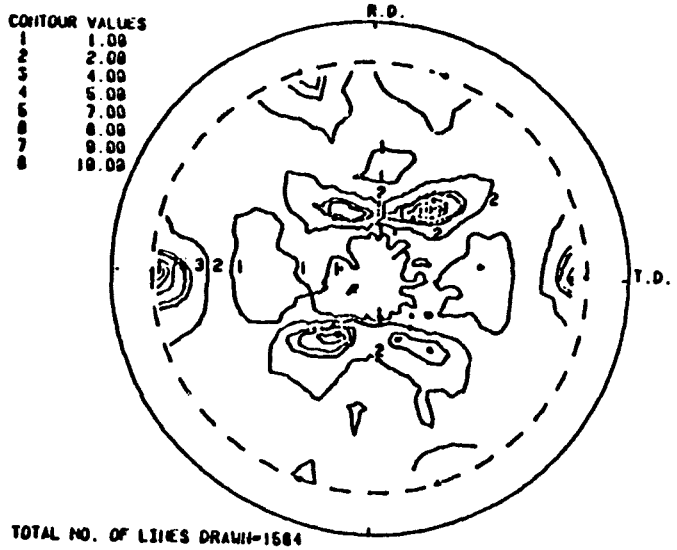

(c) (111) poles

Fig. 2: Pole figures for the rolling plane of 7050-T7451 aluminum alloy plate taken at the mid-thickness plane of the plate: (a) (200); (b) (220), and (c) (111).

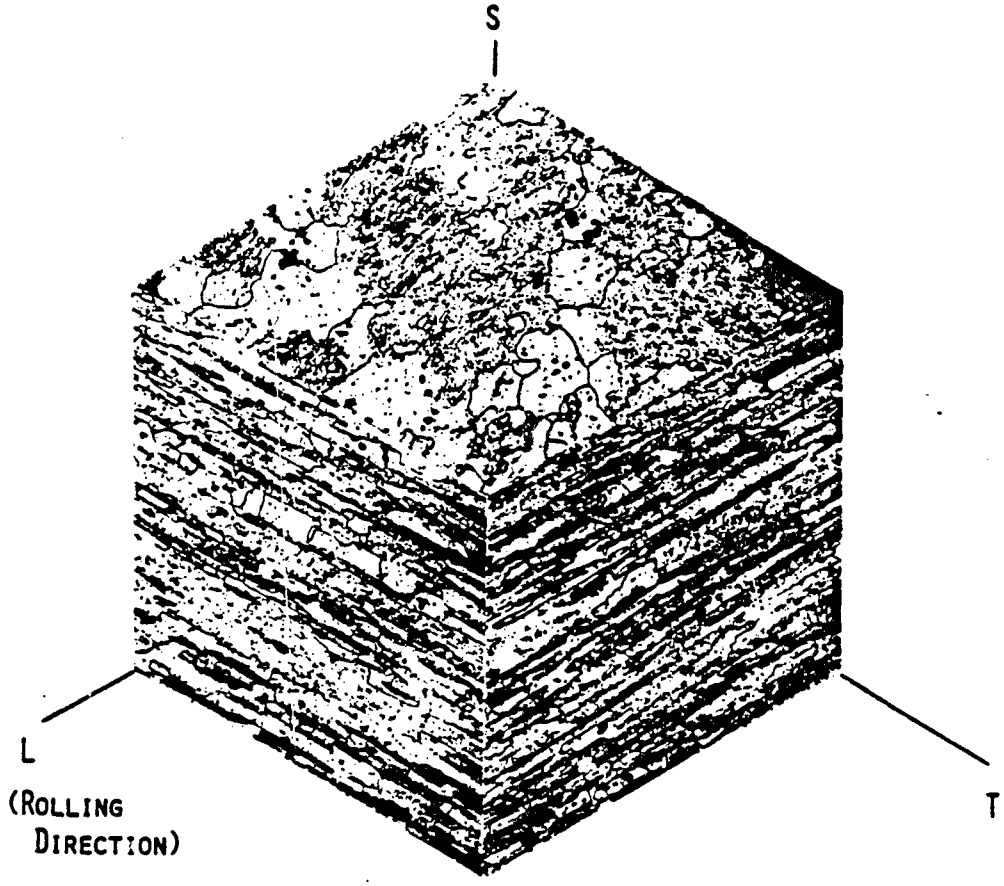

Fig. 3: Representative microstructure of 7050-T7451 aluminum alloy, 80X.

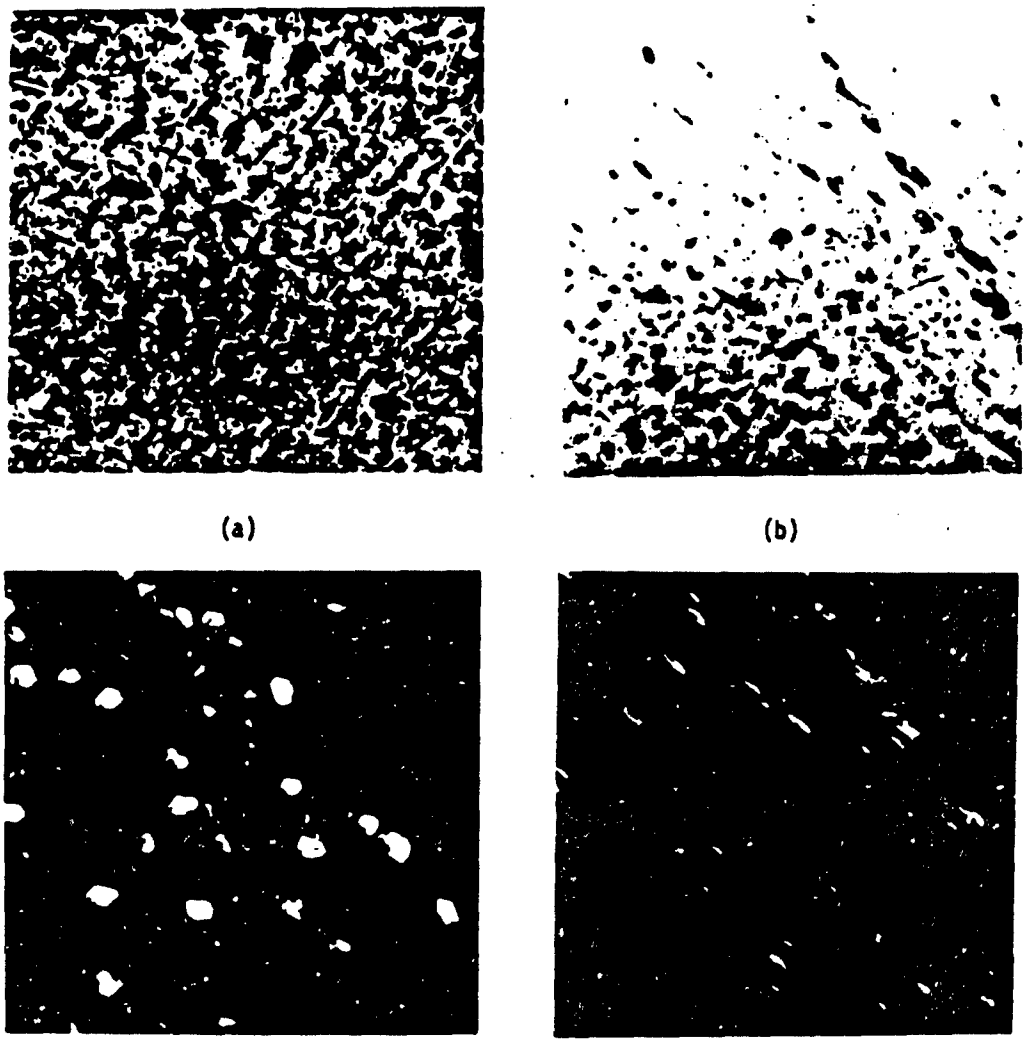

Fig. 4: Transmission electron micrographs of 7050-T7451 aluminum alloy: (a) and (b) bright field images; (c) dark field image showing equilibrium η phase, and (d) dark field image showing intermediate η' phase. Micrographs (b), (c) and (d) are from the same area. (Magnification: 100,000X.)

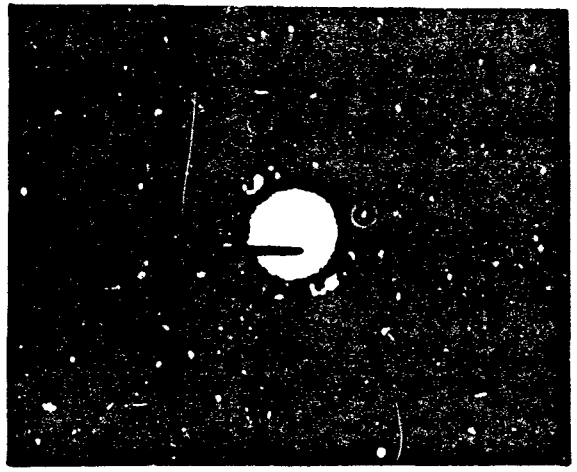

(a) SAD

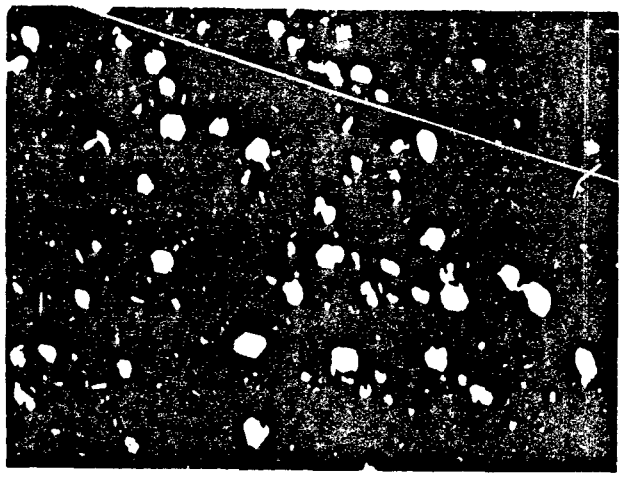

(b) Dark field image

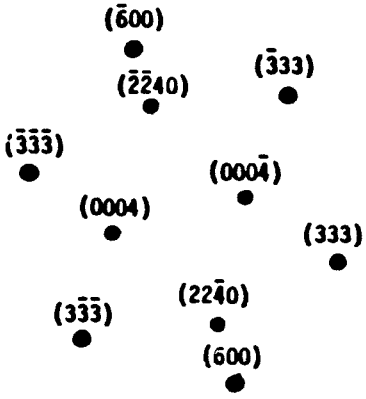

(c) Schematic

Fig. 5: Selected area diffraction (SAD) pattern showing the orientation relationship between the equilibrium η phase with the aluminum matrix. $\vec{B} = [110]_{Al}$.

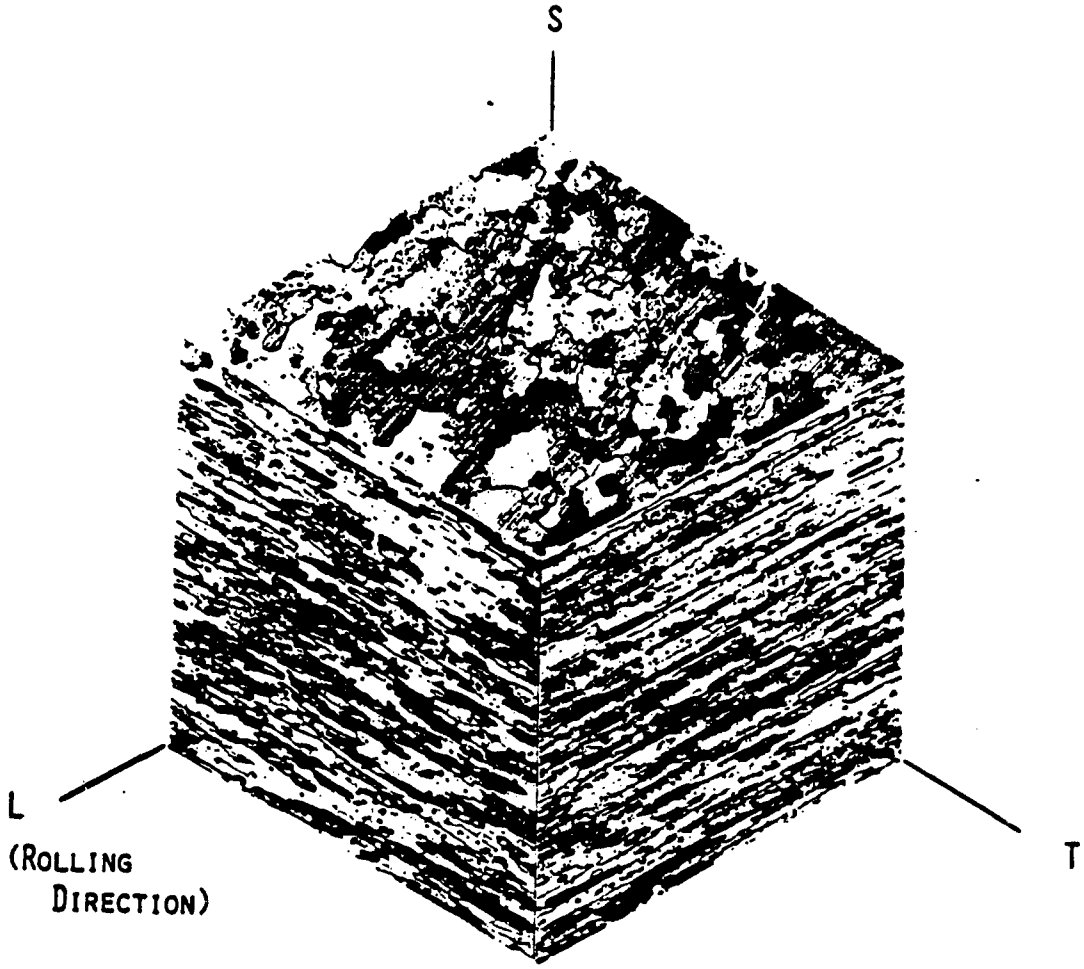

Fig. 6: Representative microstructure of 7075-T651 aluminum alloy, 80X.

132757

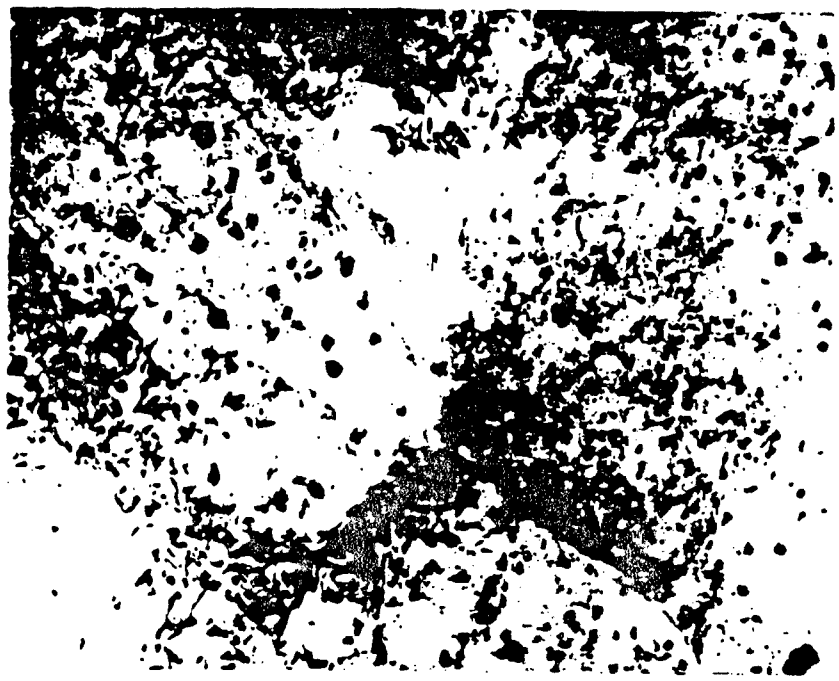

132744

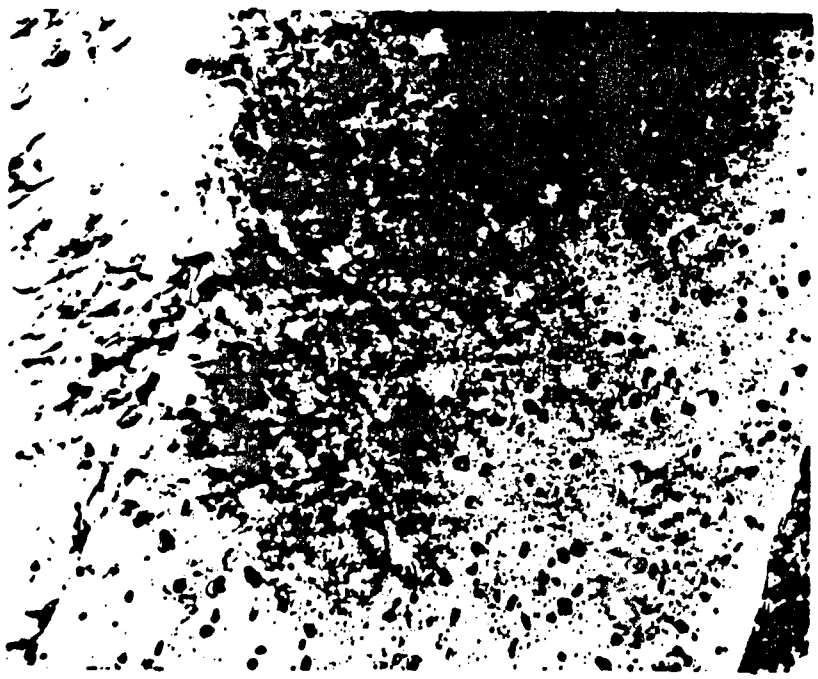

Fig. 7: Transmission electron micrographs of 7075-T651 aluminum alloy, 26,000X.

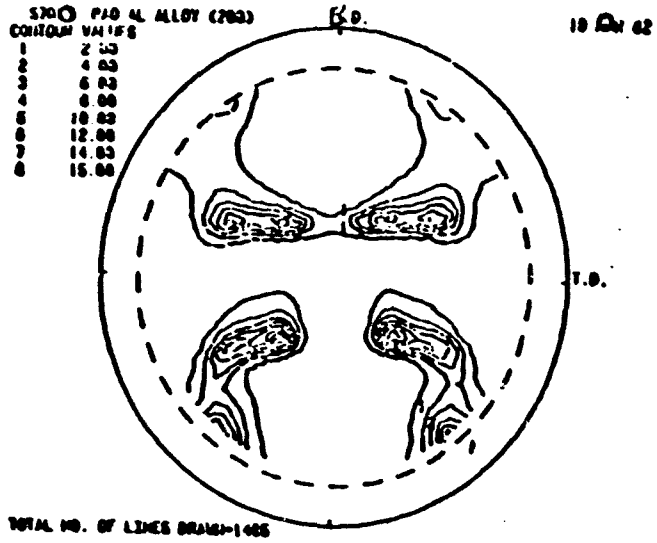

(a) (200) pole

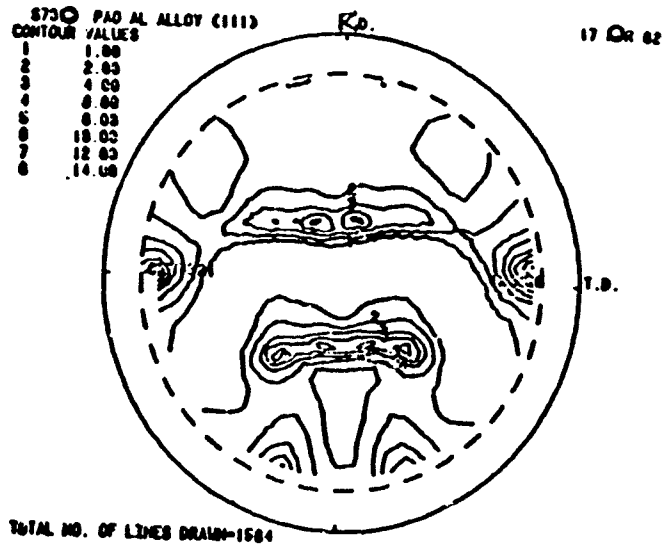

(c) (111) pole

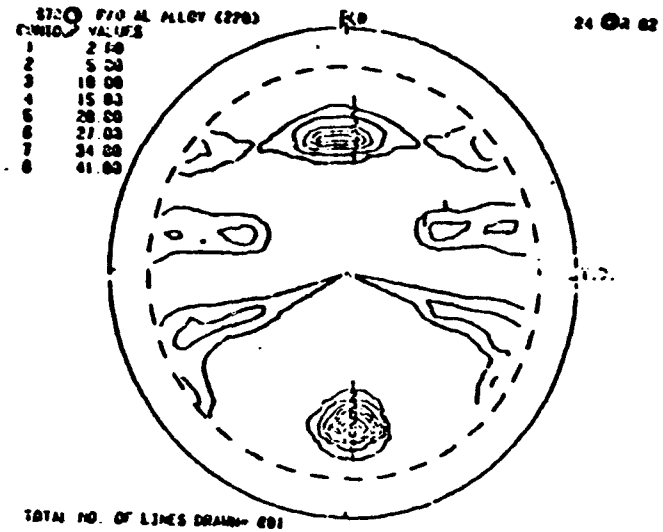

(b) (220) pole

Fig. 8: Pole figures for the rolling plane of P/M 7091-T7E70 plate taken at the plate surface: (a) (200), (b) (220), and (c) (111).

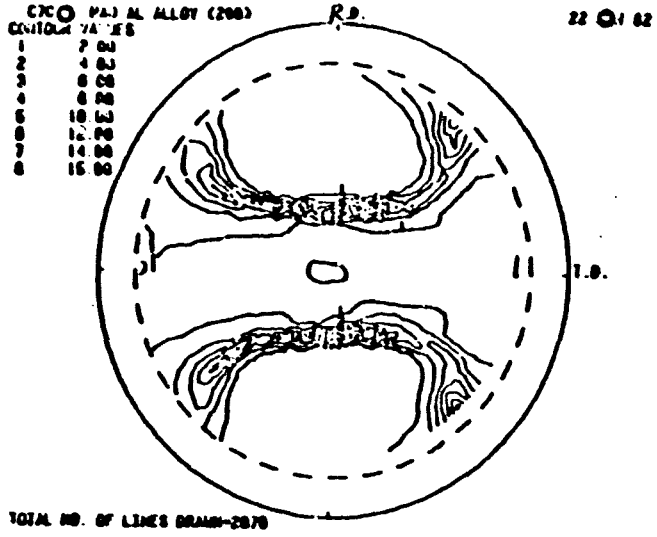

(a) (200) pole

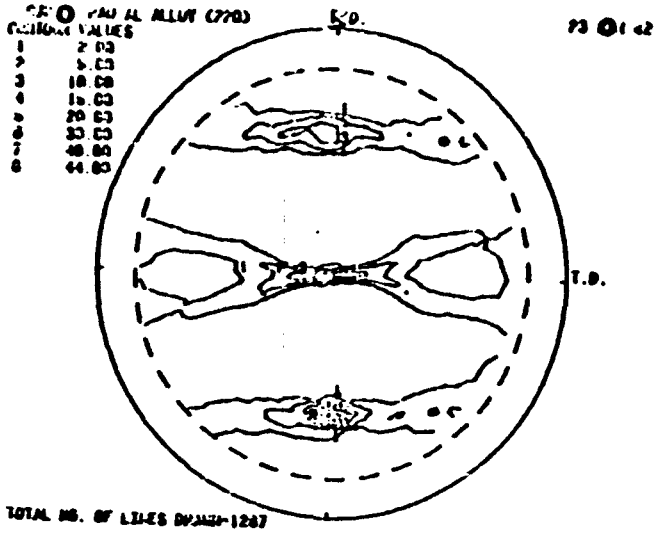

(b) (220) pole

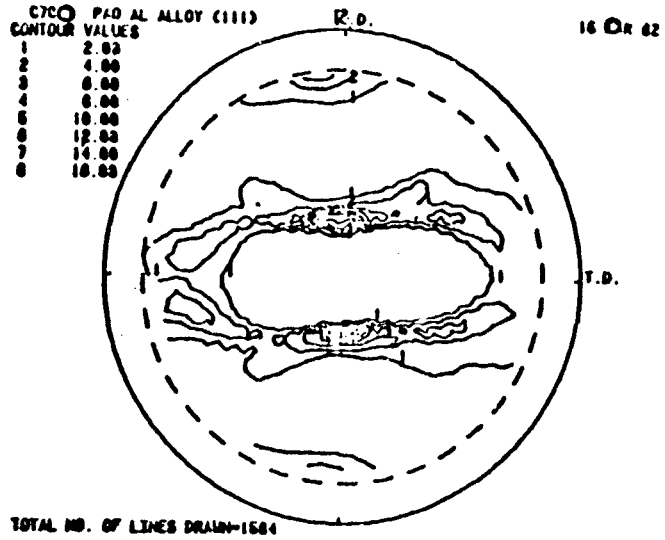

(c) (111) pole

Fig. 9: Pole figures for the rolling plane of P/M 7091-T7E70 plate taken at the mid-thickness plane of the plate: (a) (200), (b) (220), and (c) (111).

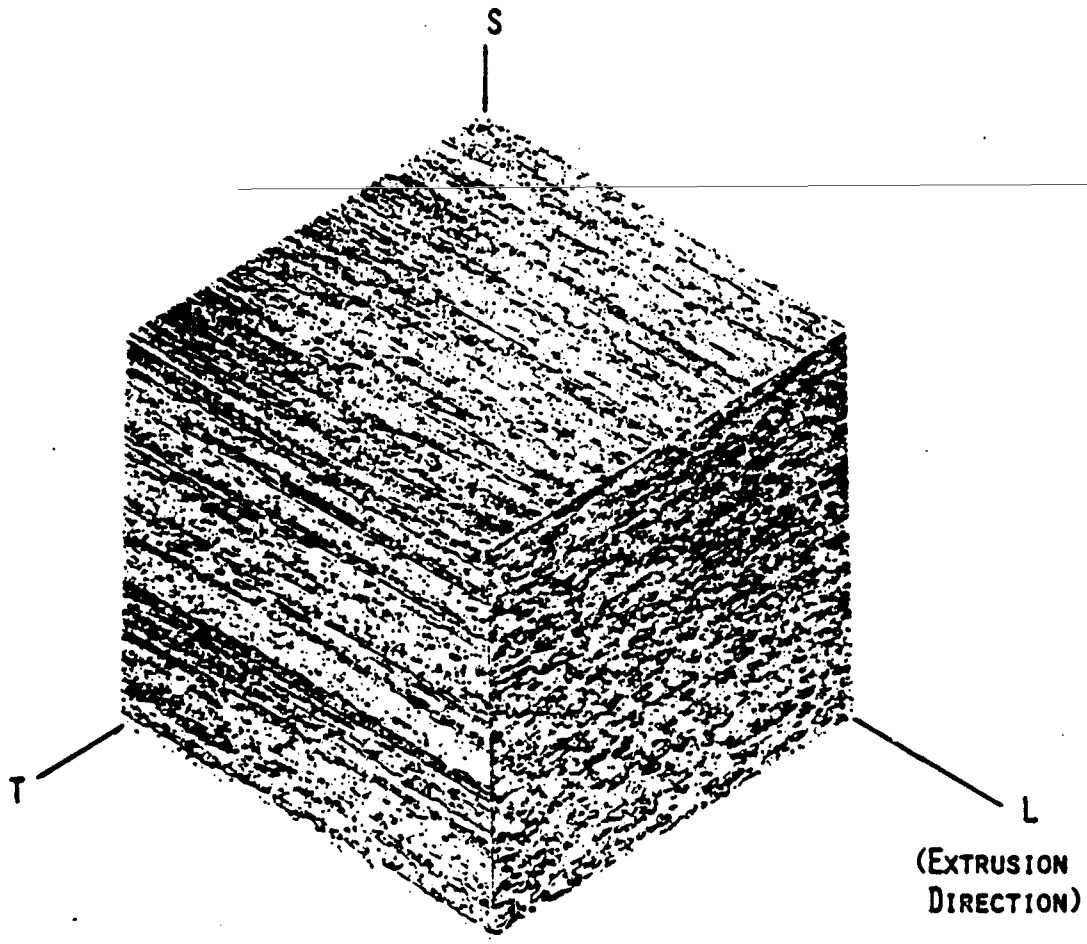

Fig. 10: Representative microstructure of P/M 7091-T7E70 aluminum alloy, 420X.

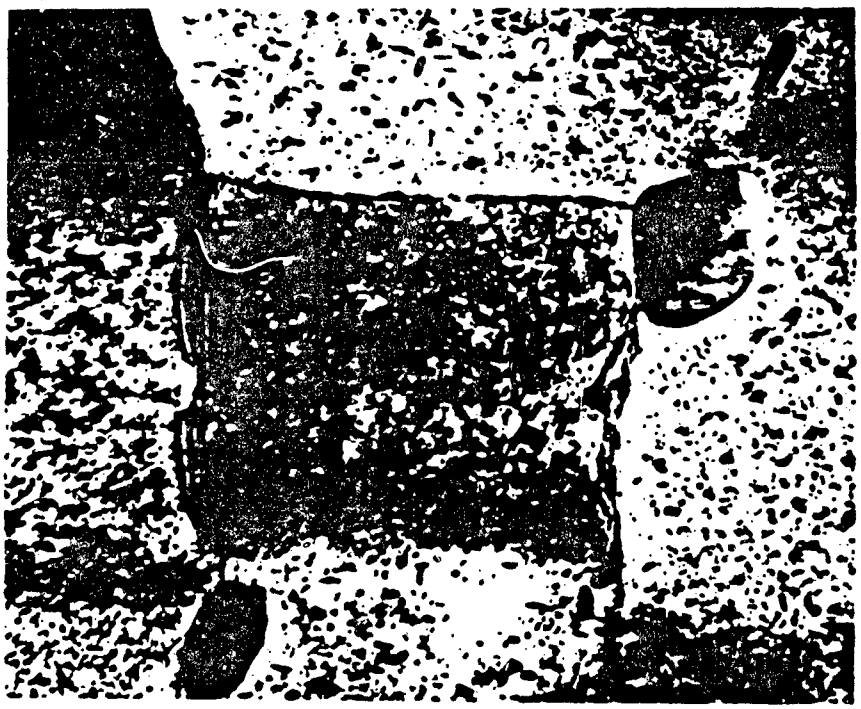

Fig. 11: Transmission electron micrograph of P/M 7091-T7E70, 110,000X.

(a)

(b)

Fig. 12: Transmission electron micrographs of P/M 7091-T7E70: (a) bright field, and (b) dark field images, 65,000X.

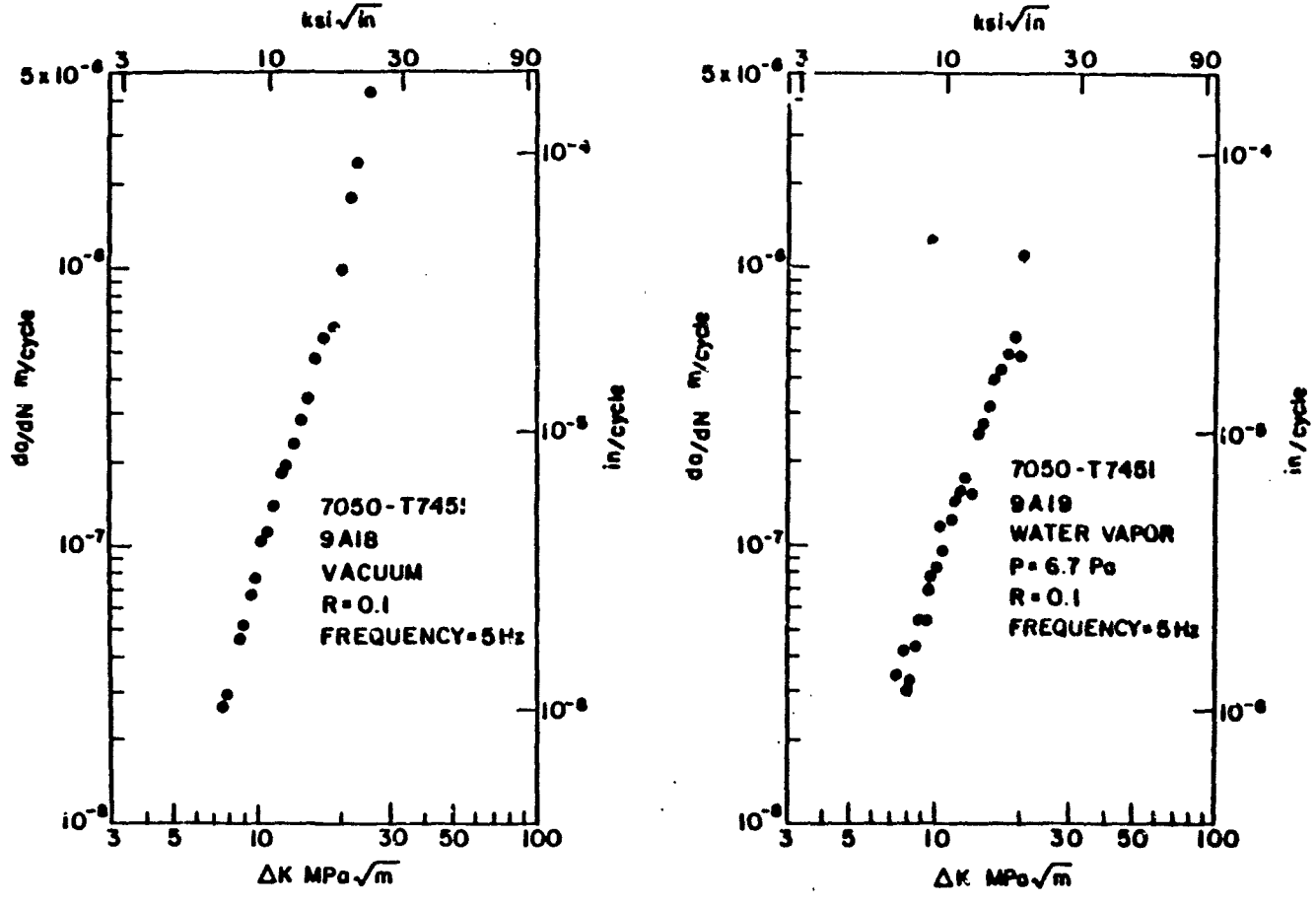

Fig. 13: Kinetics of fatigue crack growth for 7050-T7451 aluminum alloy at room temperature (R = 0.1 and f = 5 Hz) in vacuum ($<10^{-6}$ Pa) and in water vapor at 6.7 Pa.

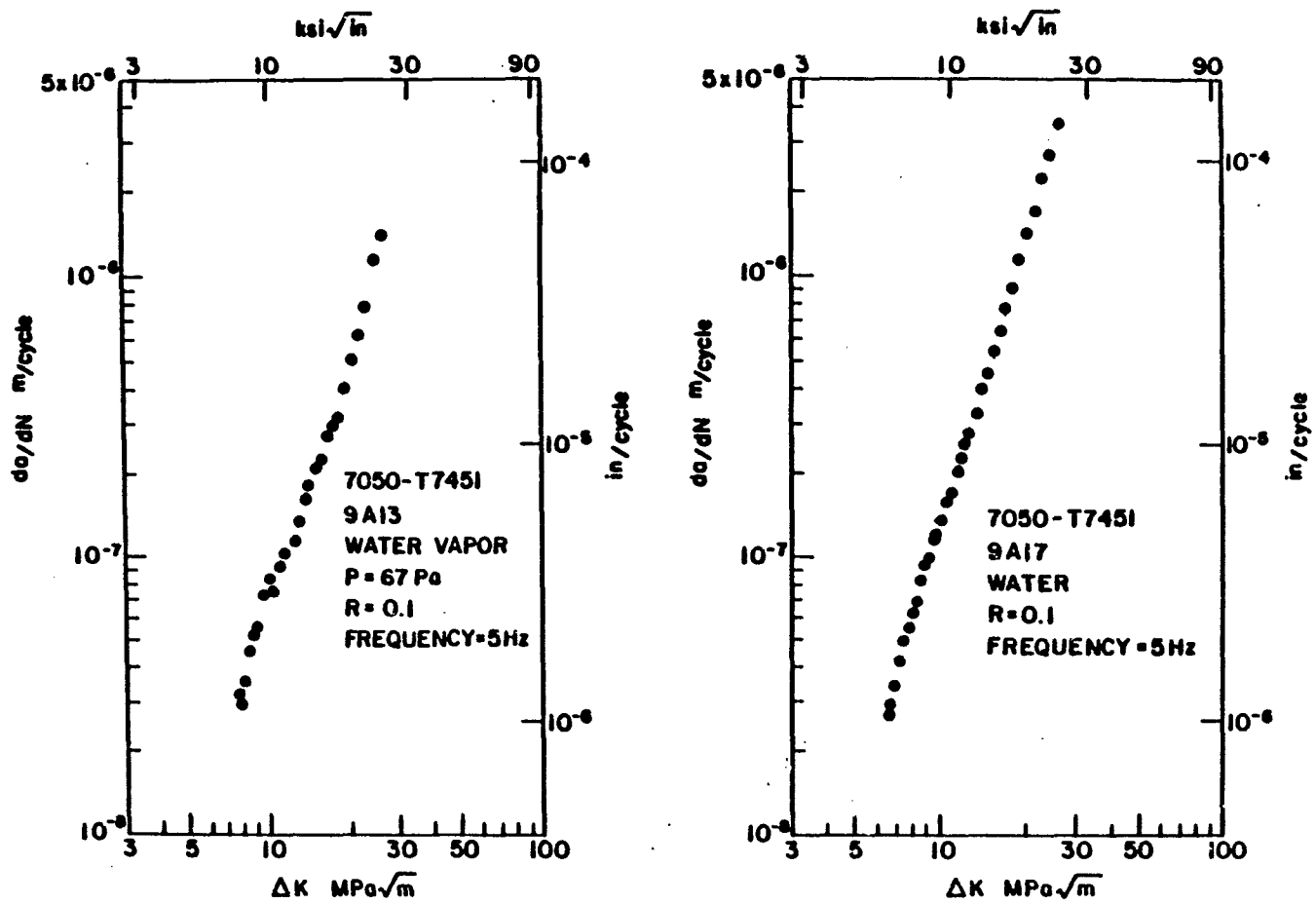

Fig. 14: Kinetics of fatigue crack growth for 7050-T7451 aluminum alloy at room temperature (R = 0.1 and f = 5 Hz) in water vapor at 67 Pa, and in distilled water.

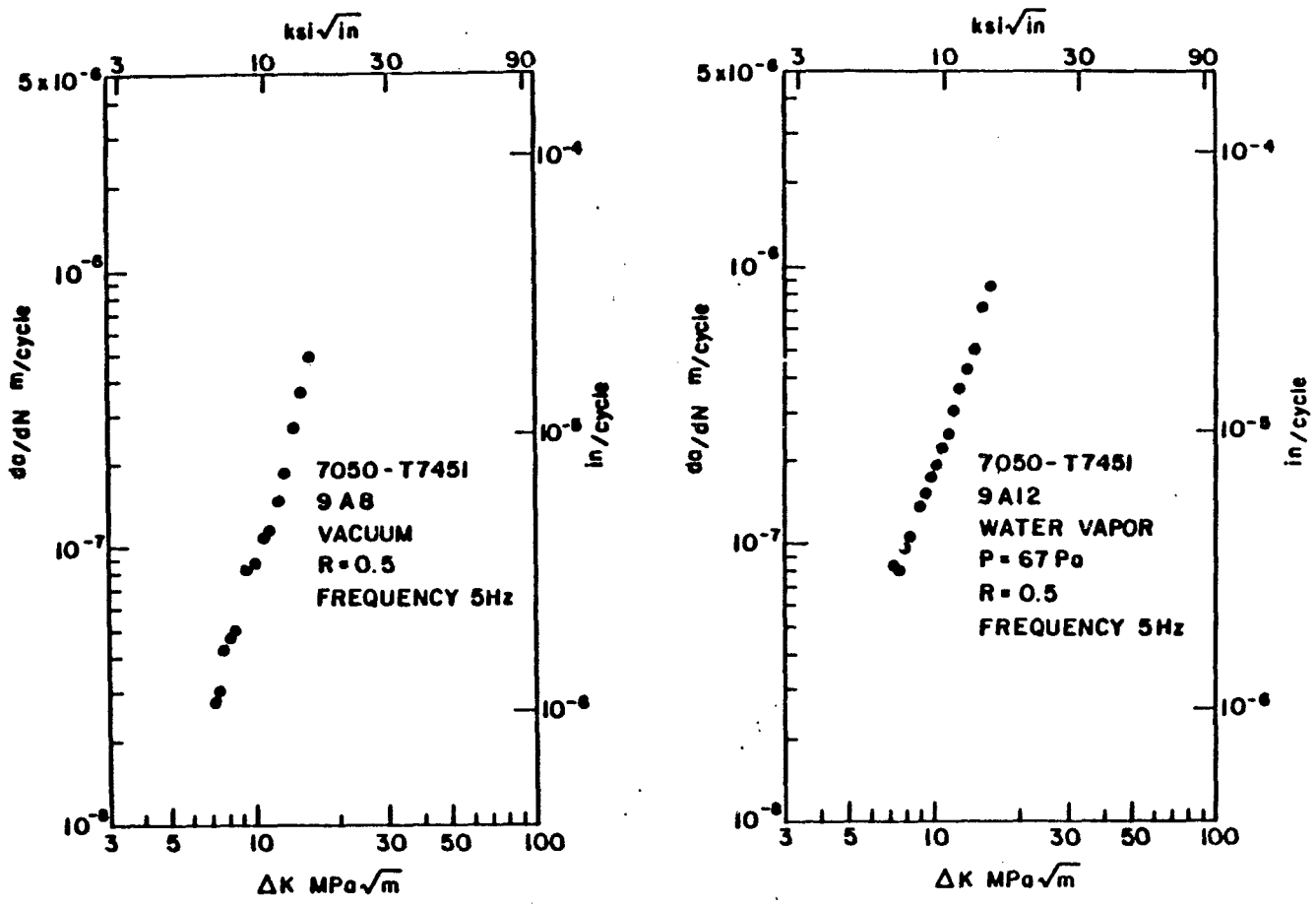

Fig. 15: Kinetics of fatigue crack growth for 7050-T7451 aluminum alloy at room temperature (R = 0.5 and f = 5 Hz) in vacuum ($<10^{-6}$ Pa) and in water vapor at 67 Pa.

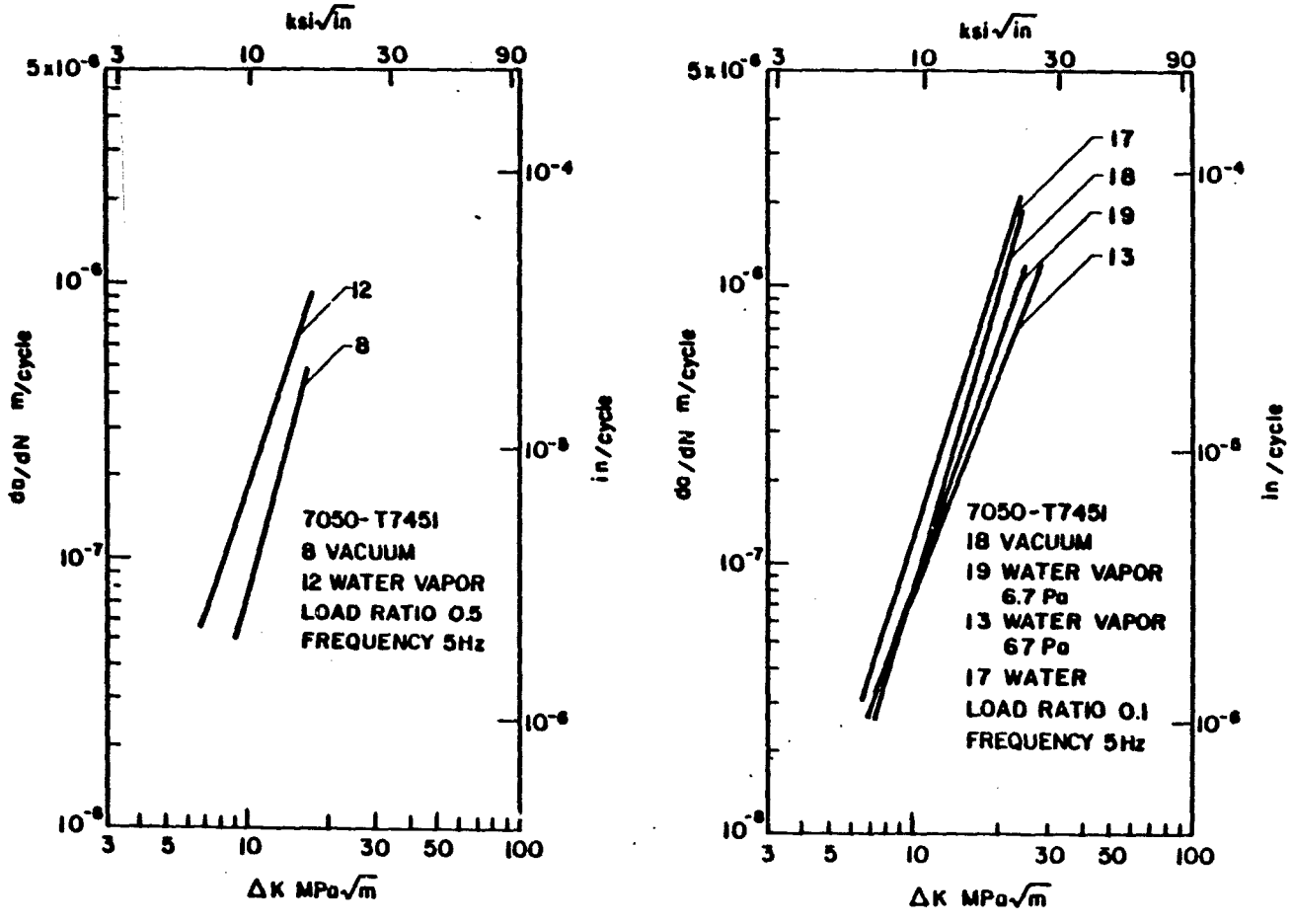

Fig. 16: Comparison of the kinetics of fatigue crack growth in 7050-T7451 aluminum alloy tested in vacuum, water vapor and water at R = 0.1 and 0.5. (Lines represent data shown in Figs. 13-15.)

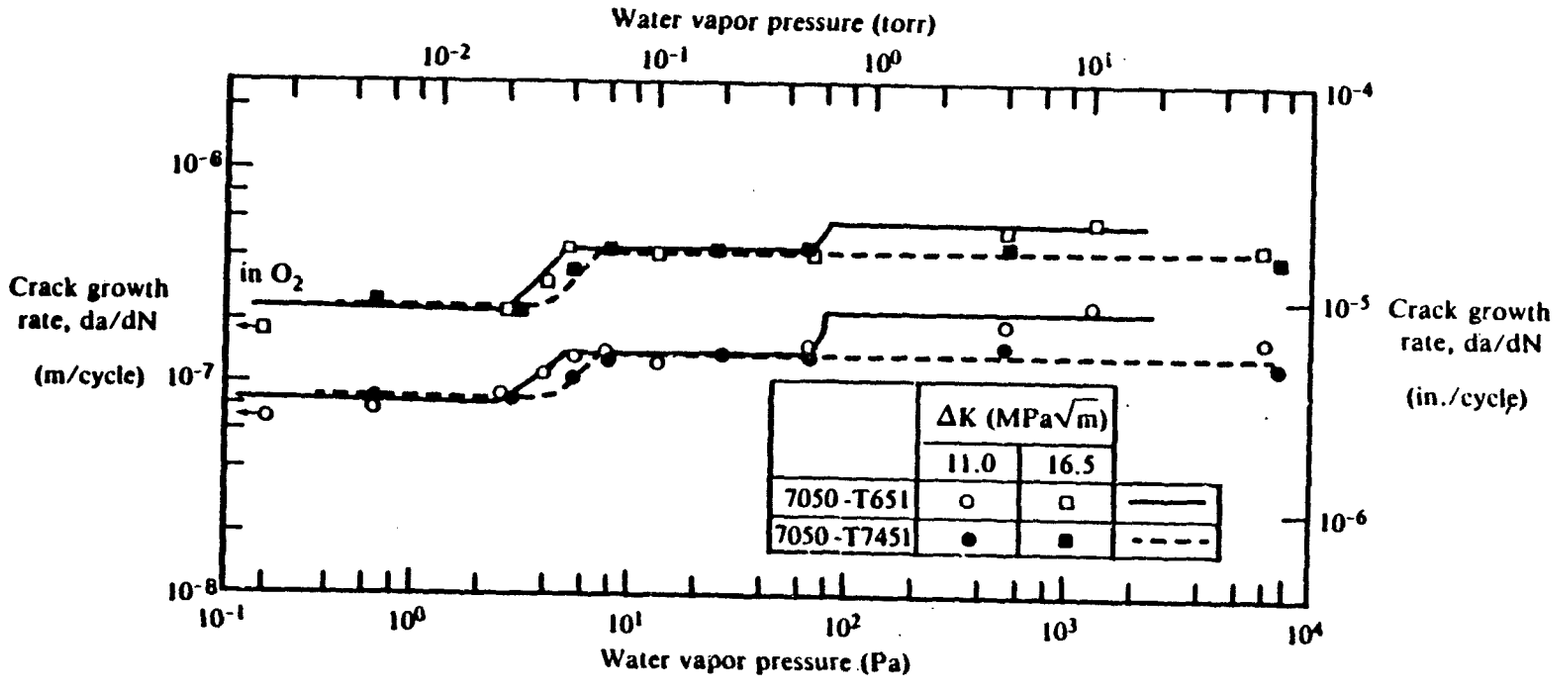

Fig. 17: The influence of water vapor pressure on the fatigue crack growth rate in I/M 7050 aluminum alloys at room temperature (R = 0.1 and f = 5 Hz).

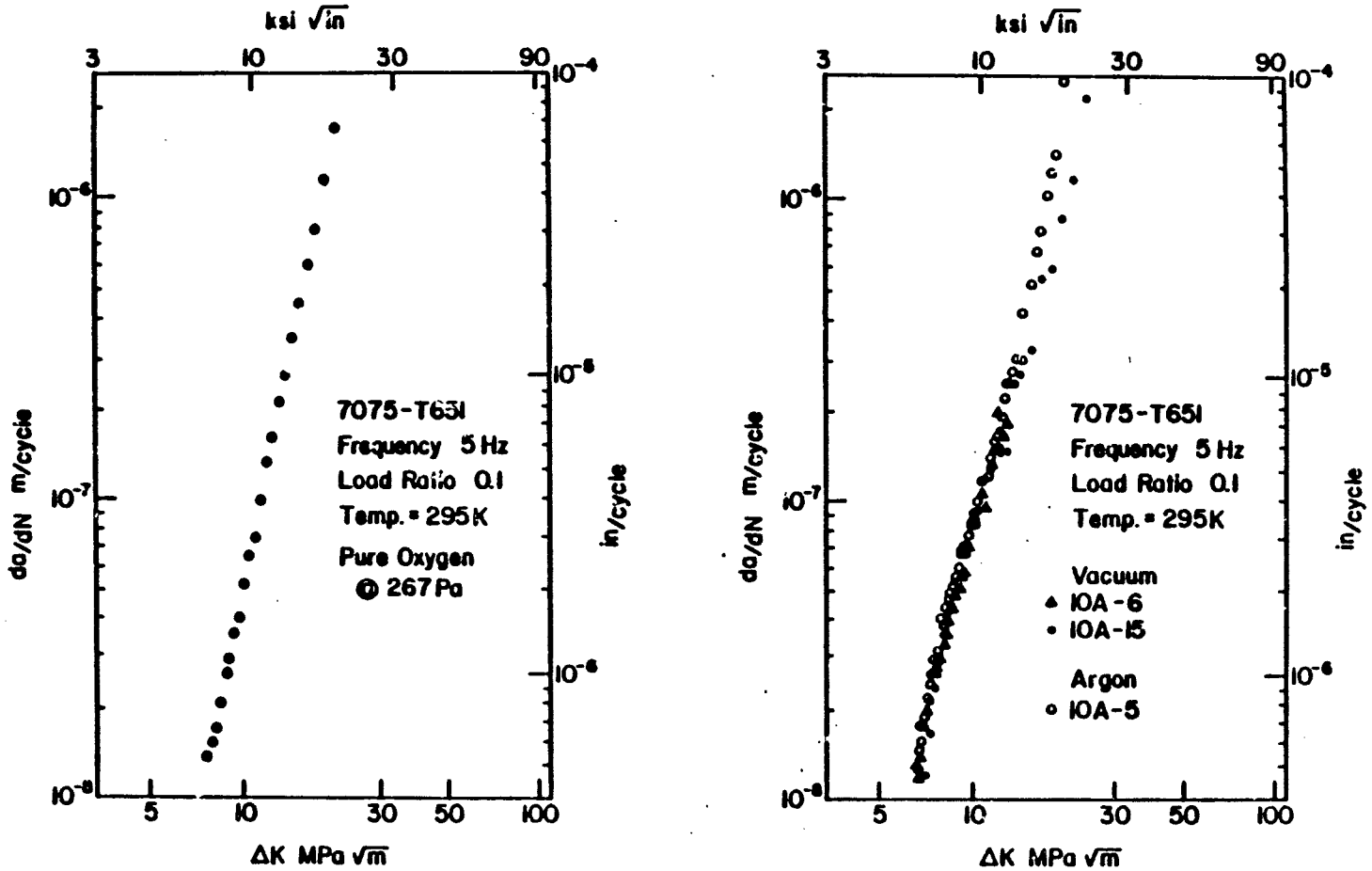

Fig. 18: Kinetics of fatigue crack growth for 7075-T651 aluminum alloy at 295K (R = 0.1 and f = 5 Hz) in pure oxygen at 267 Pa, and in vacuum ($<10^{-6}$ Pa) and argon.

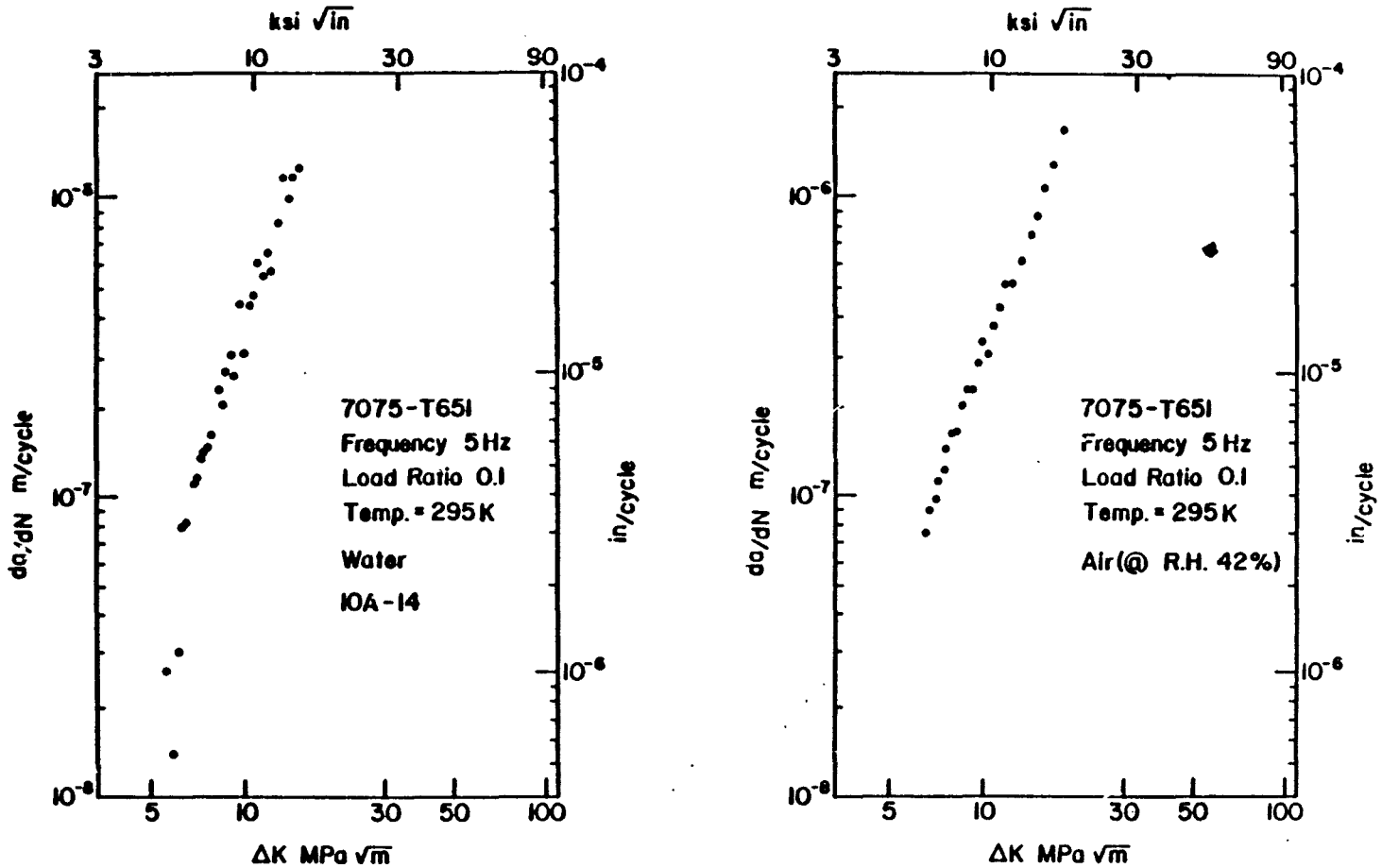

Fig. 19: Kinetics of fatigue crack growth for 7075-T651 aluminum alloy at 295K (R = 0.1 and f = 5 Hz) in water and in air at 42% relative humidity.

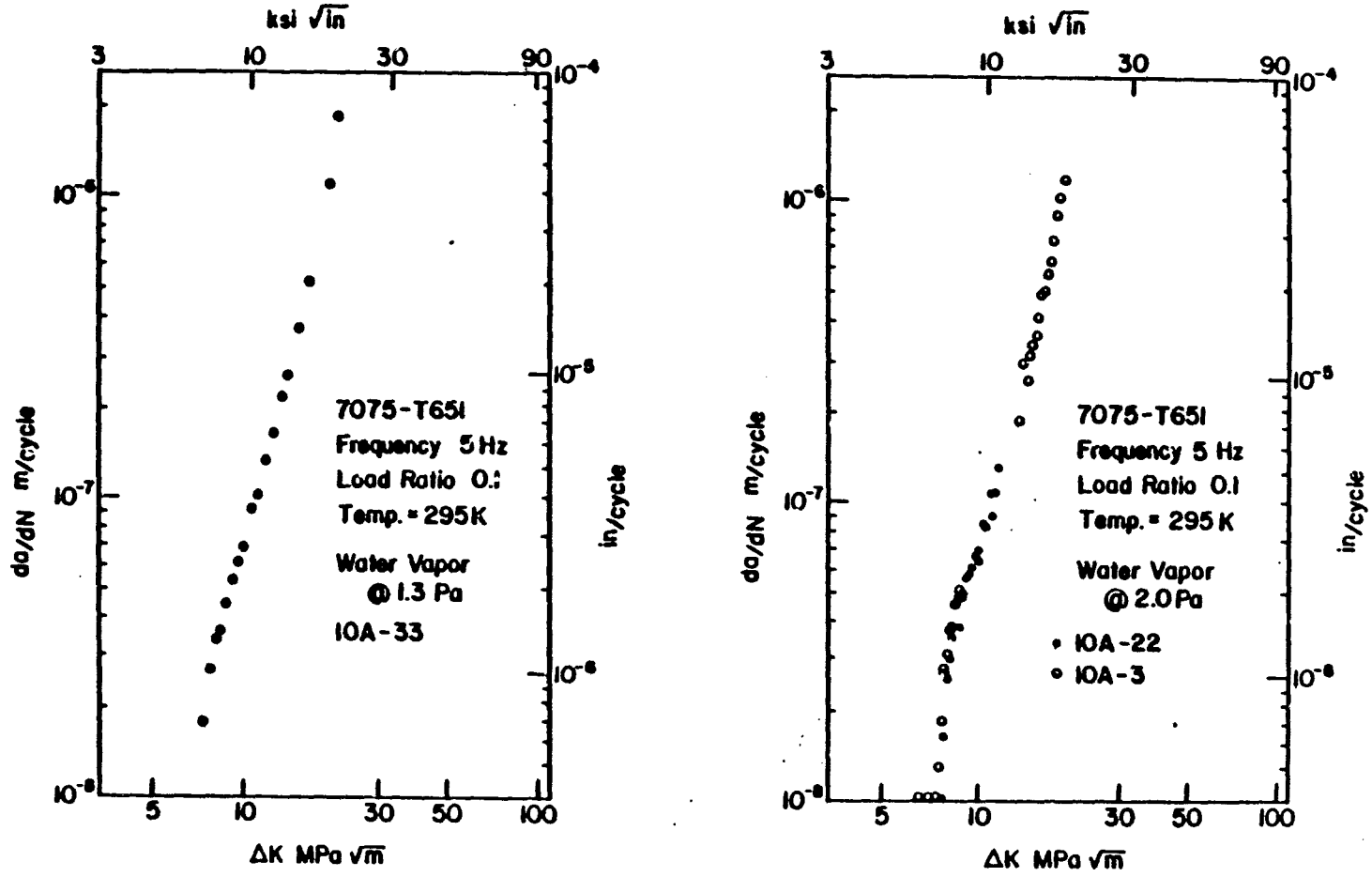

Fig. 20: Kinetics of fatigue crack growth for 7075-T651 aluminum alloy at 295K (R = 0.1 and f = 5 Hz) in water vapor at 1.3 Pa and 2.0 Pa.

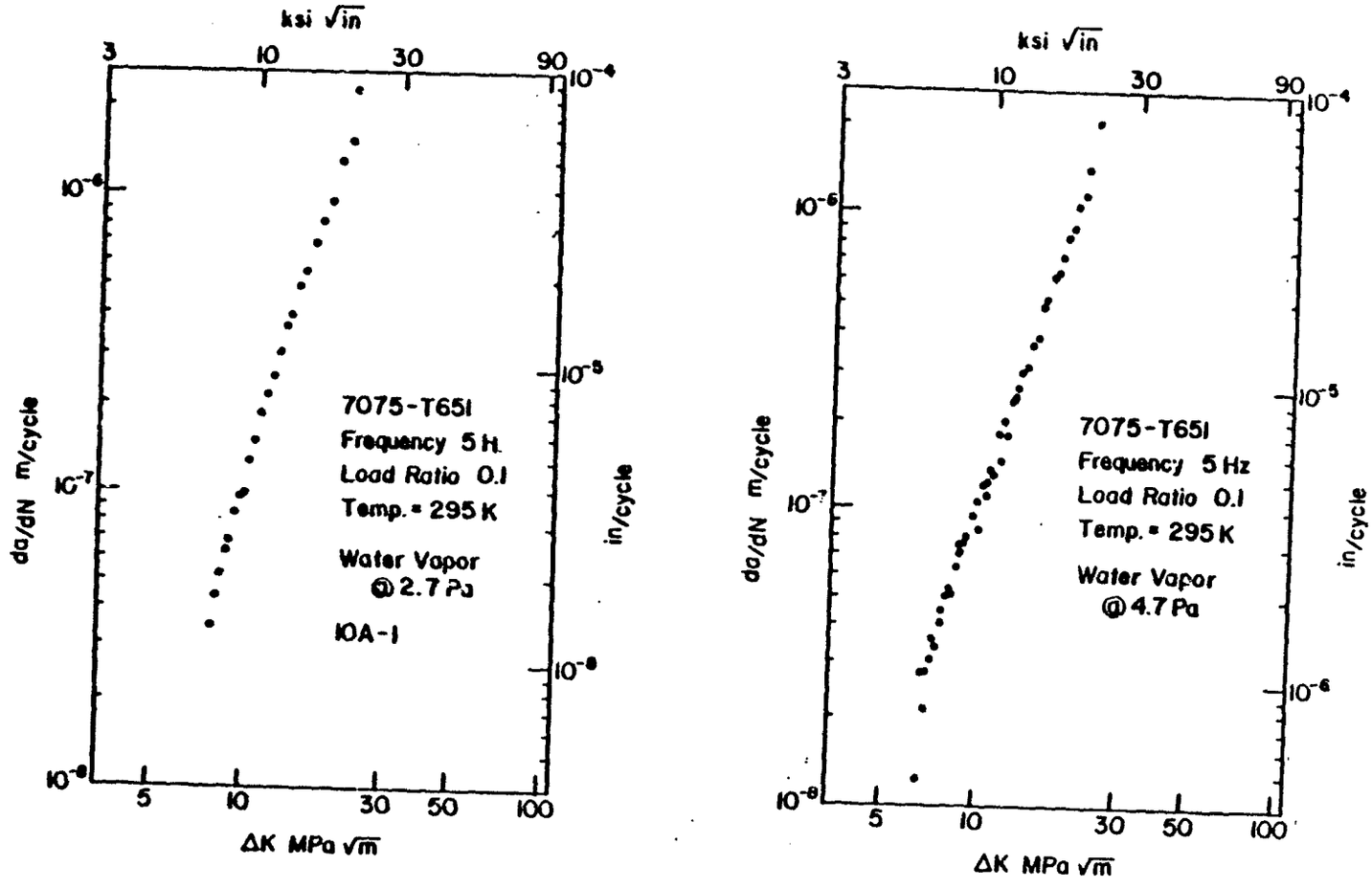

Fig. 21: Kinetics of fatigue crack growth for 7075-T651 aluminum alloy at 295K (R = 0.1 and f = 5 Hz) in water vapor at 2.7 Pa and 4.7 Pa.

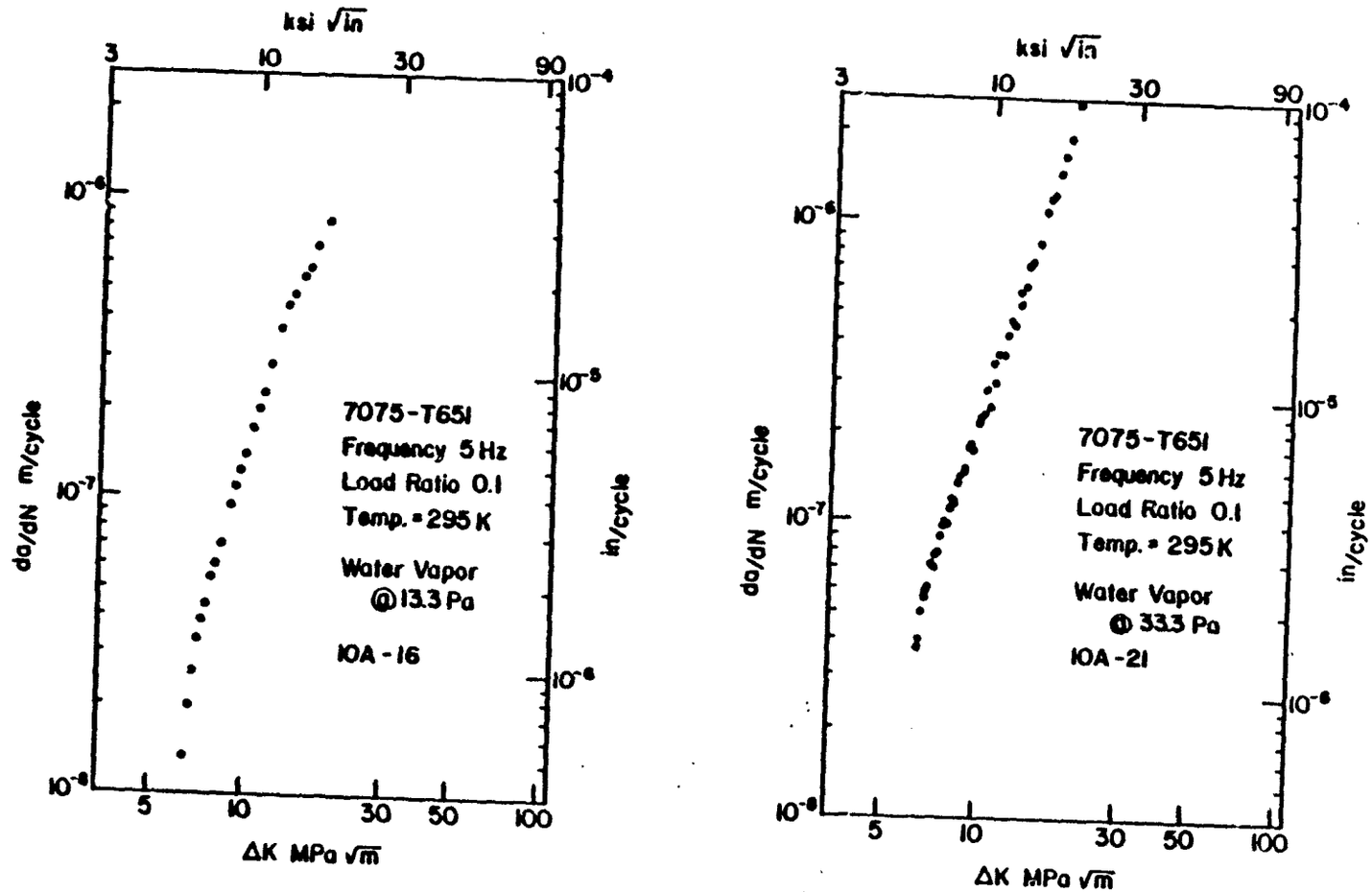

Fig. 22: Kinetics of fatigue crack growth for 7075-T651 aluminum alloy at 295K (R = 0.1 and f = 5 Hz) in water vapor at 13.3 Pa and 33.3 Pa.

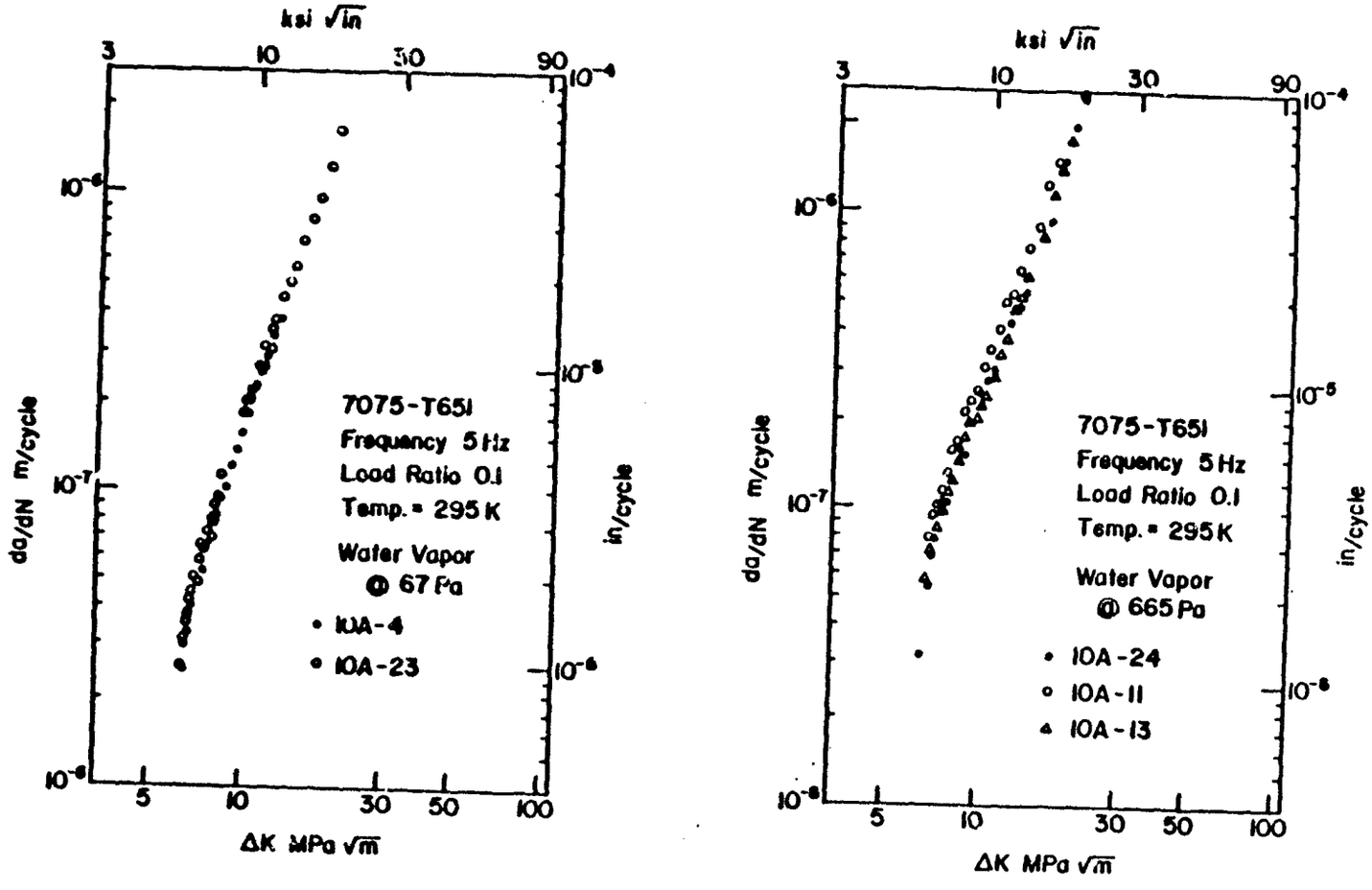

Fig. 23: Kinetics of fatigue crack growth for 7075-T651 aluminum alloy at 295K (R = 0.1 and f = 5 Hz) in water vapor at 67 Pa and 665 Pa.

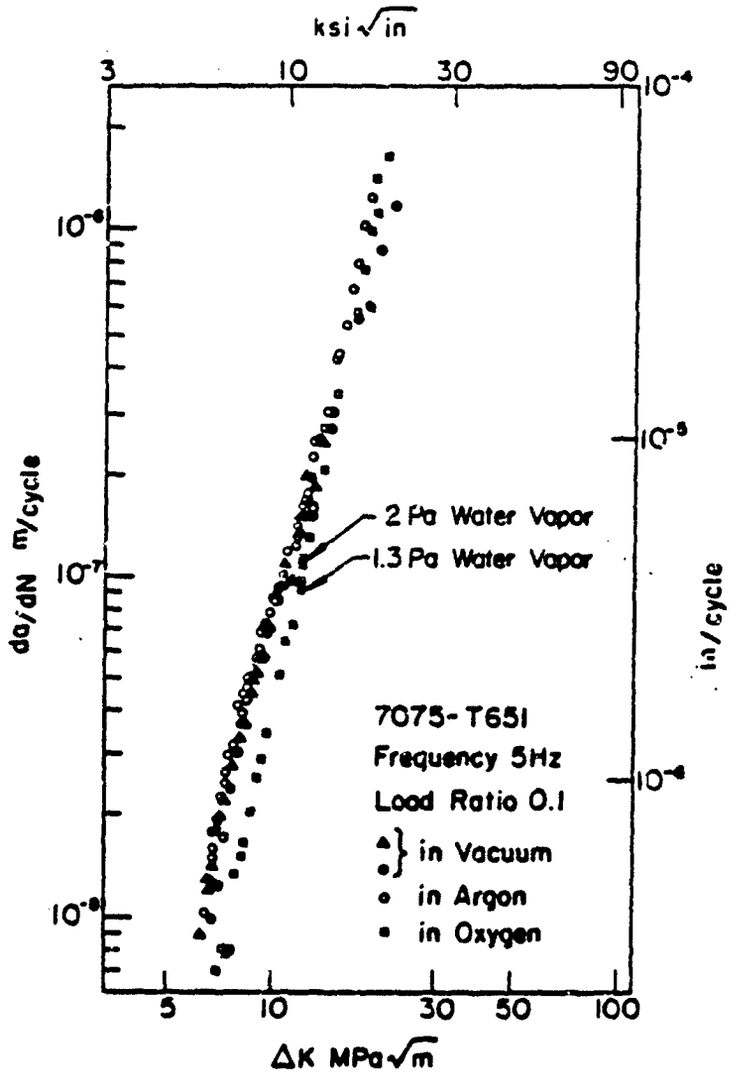

Fig. 24: Comparison of the kinetics of fatigue crack growth in I/M 7075-T651 in vacuum, pure argon and pure oxygen.

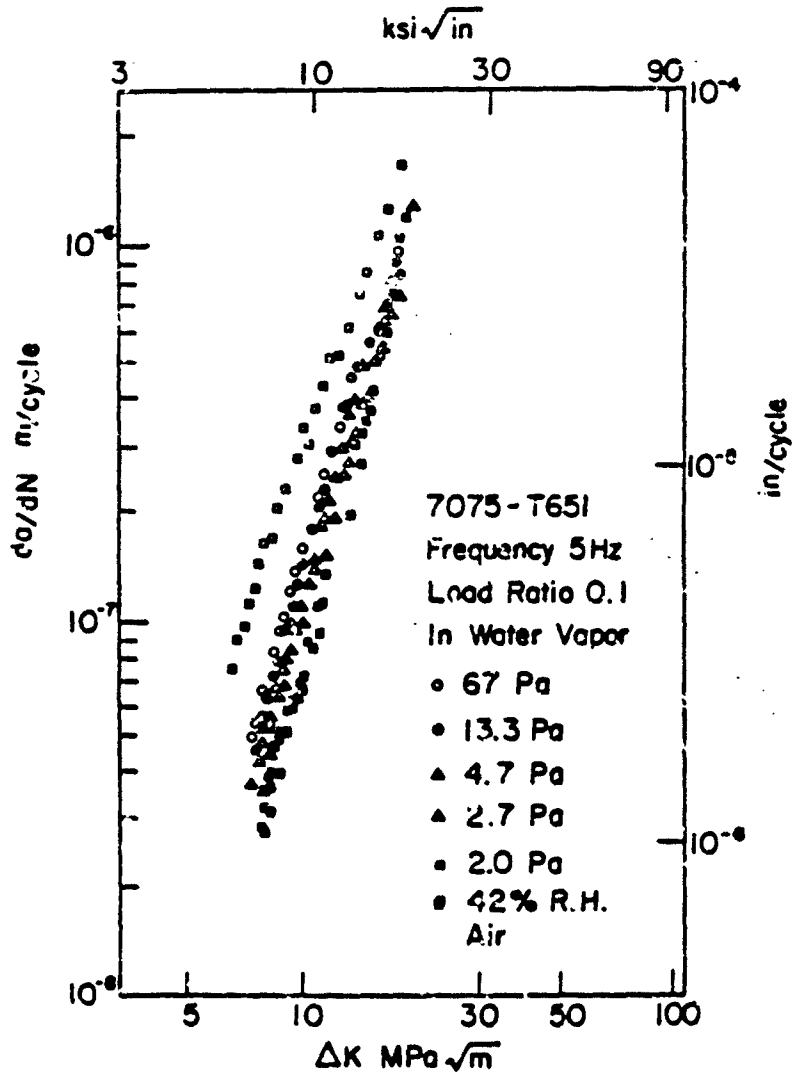

Fig. 25: Effect of water vapor pressure on fatigue crack growth kinetics for I/M 7075-T651 (f = 5 Hz, R = 0.1).

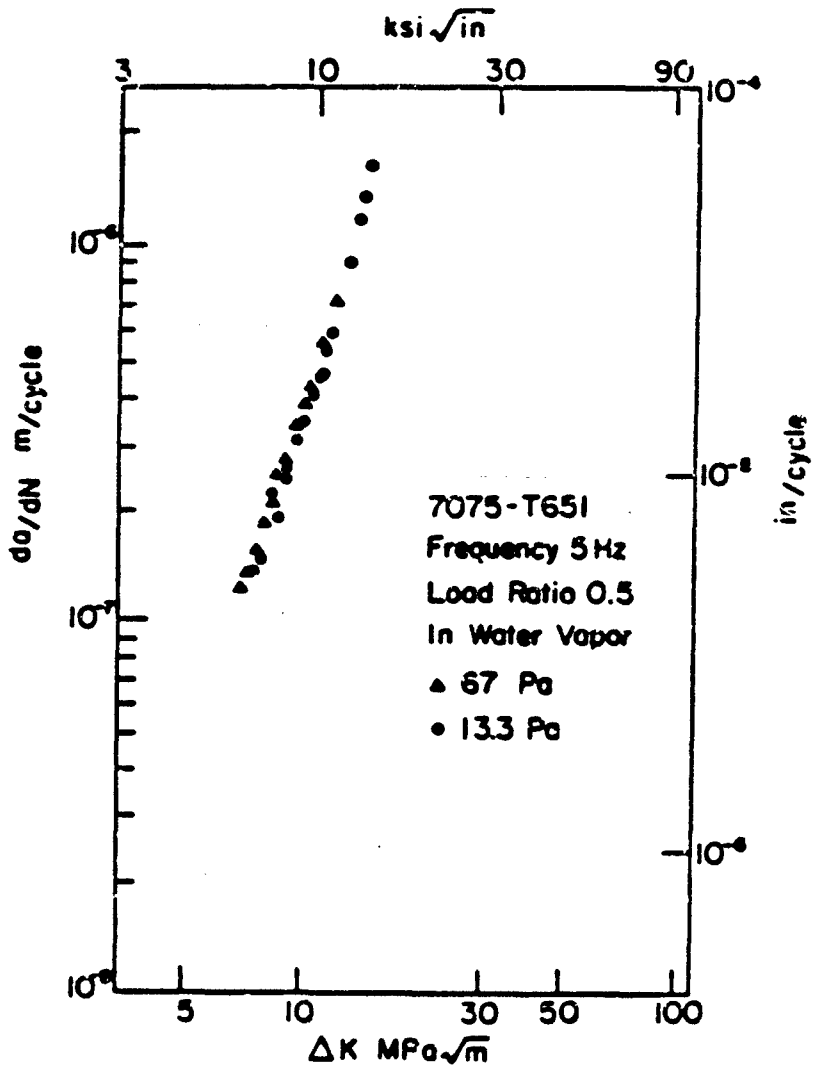

Fig. 26: Effect of water vapor pressure on fatigue crack growth kinetics for I/M 7075-T651 (R = 0.5 and f = 5 Hz).

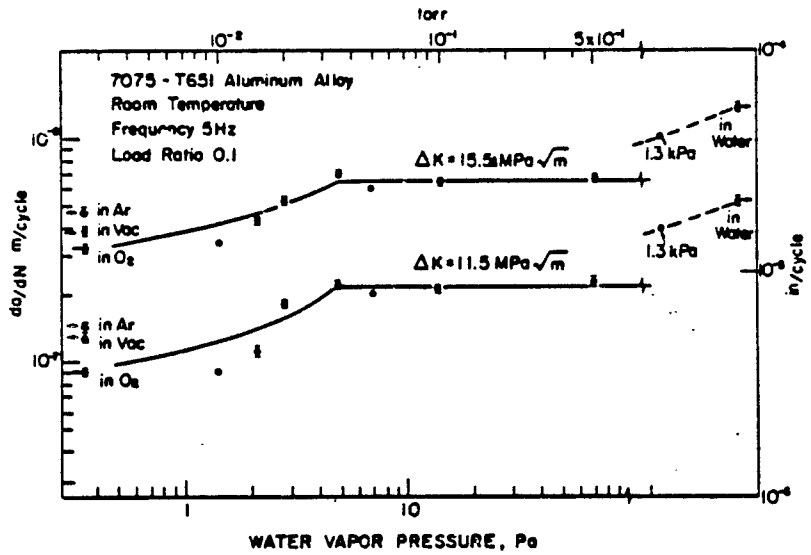

Fig. 27: The influence of water vapor pressure on the fatigue crack growth rate in I/M 7075-T651 aluminum alloy at room temperature and R = 0.1.

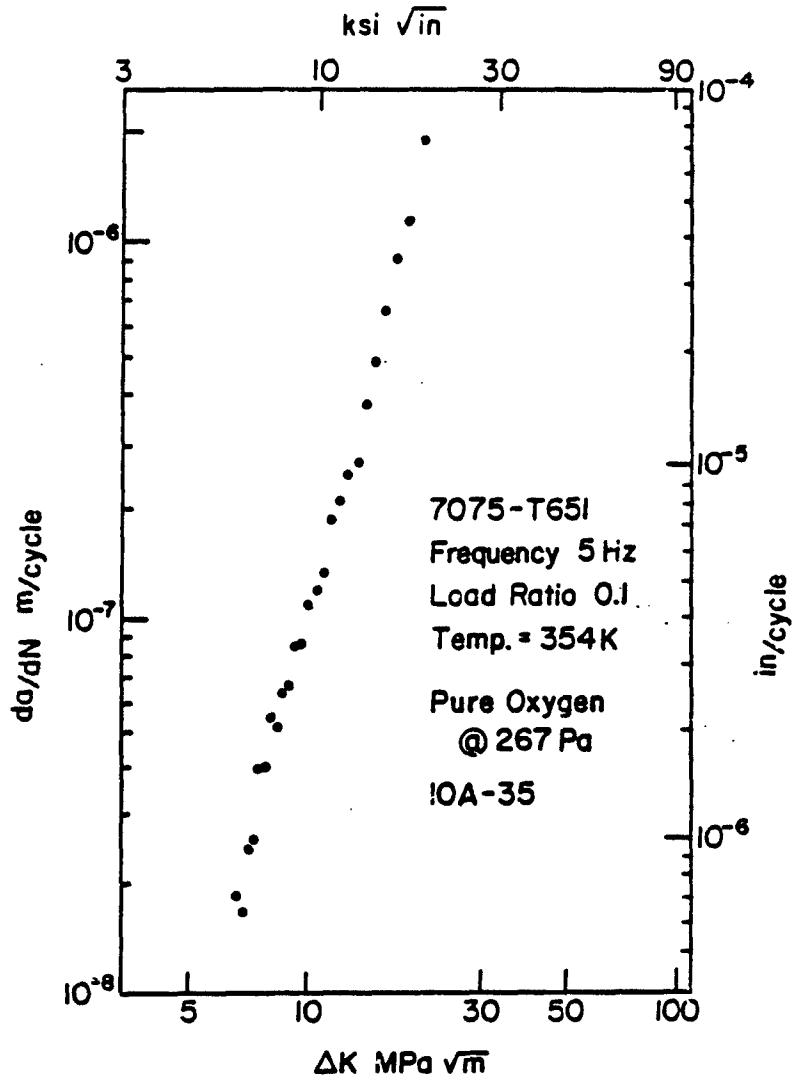

Fig. 28: Kinetics of fatigue crack growth for 7075-T651 aluminum alloy at 354K (R = 0.1 and f = 5 Hz) in pure oxygen at 267 Pa.

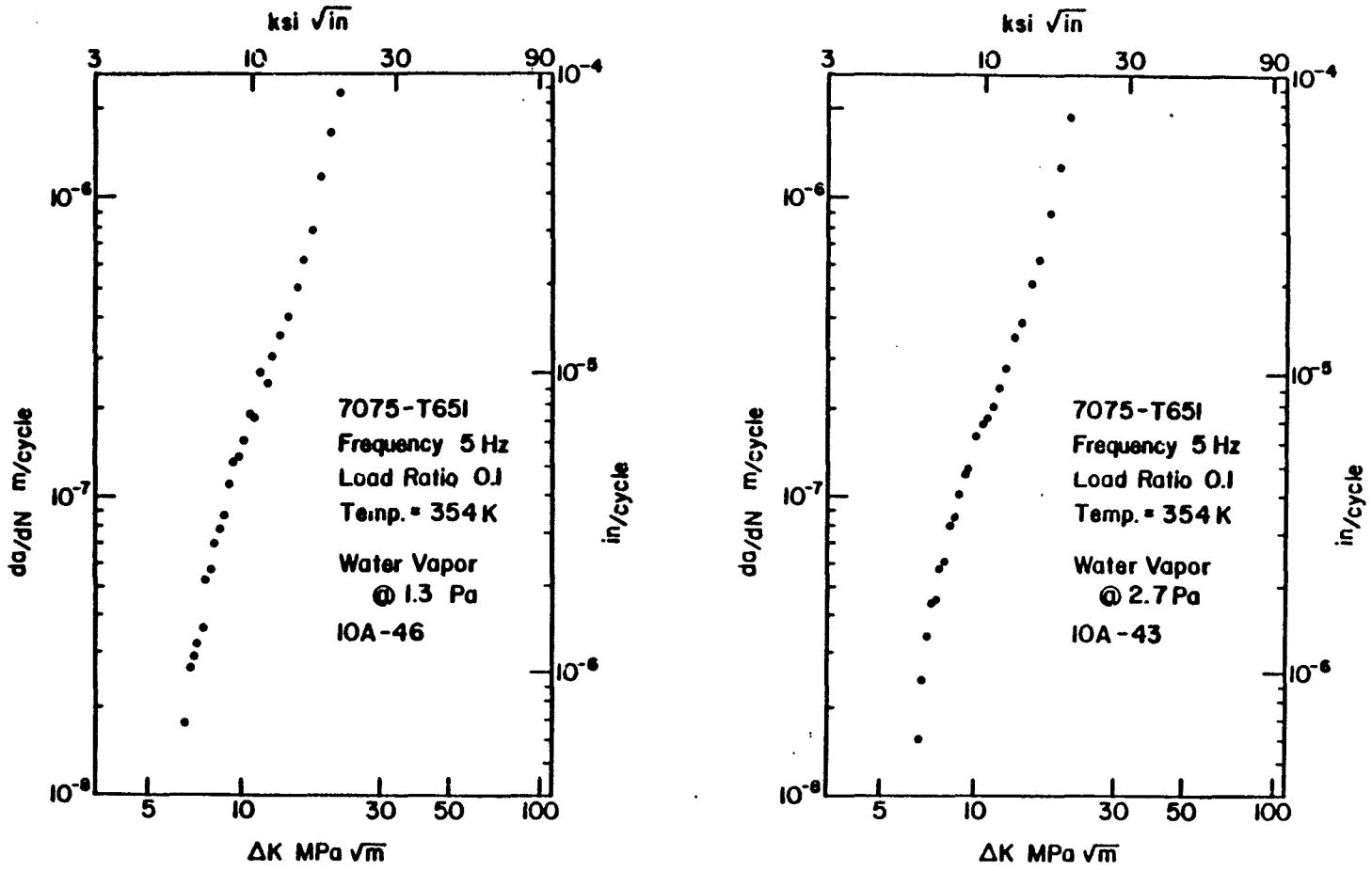

Fig. 29: Kinetics of fatigue crack growth for 7075-T651 aluminum alloy at 354K (R = 0.1 and f = 5 Hz) in water vapor at 1.3 Pa and 2.7 Pa.

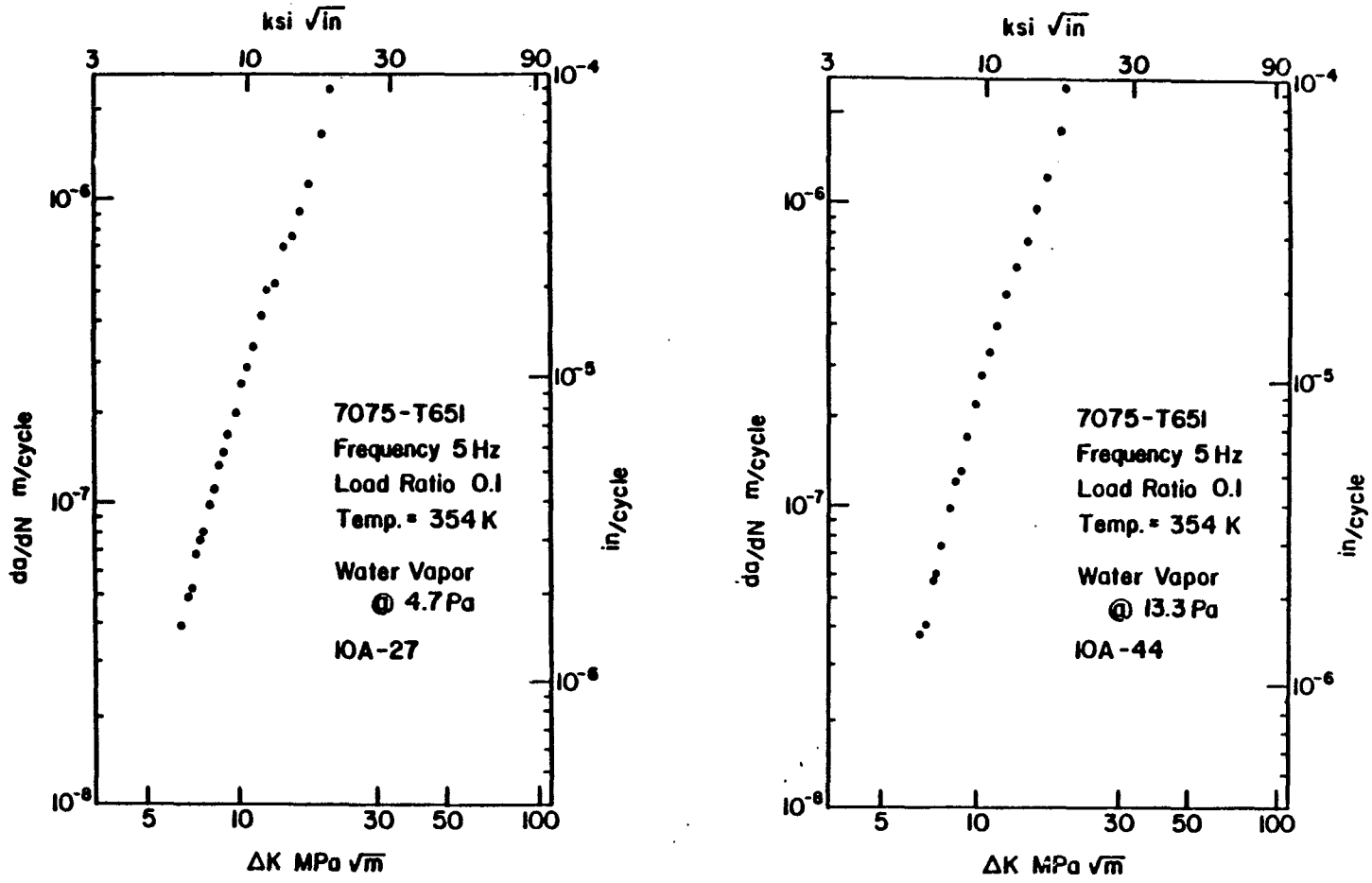

Fig. 30: Kinetics of fatigue crack growth for 7075-T651 aluminum alloy at 354K (R = 0.1 and f = 5 Hz) in water vapor at 4.7 Pa and 13.3 Pa.

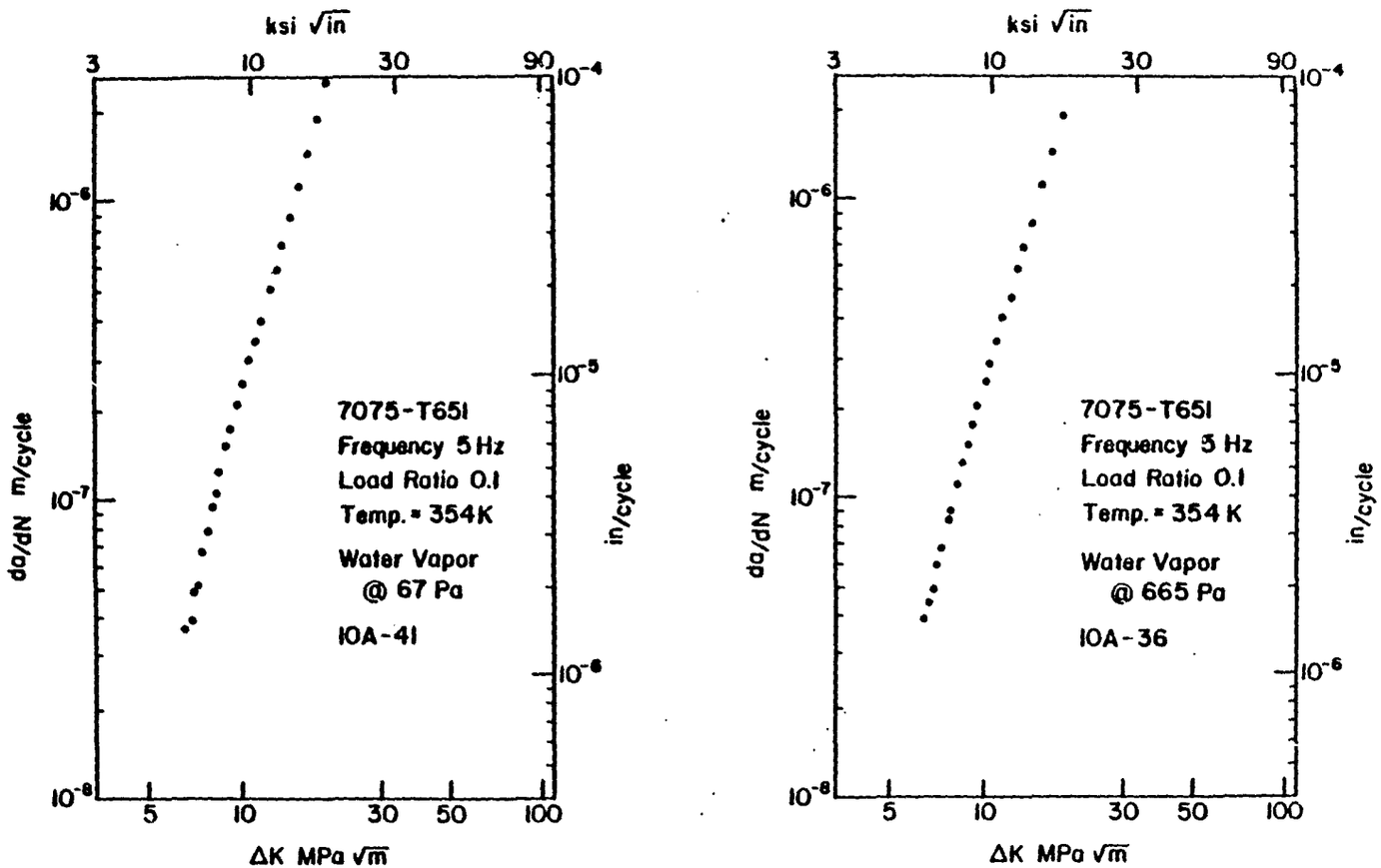

Fig. 31: Kinetics of fatigue crack growth for 7075-T651 aluminum alloy at 354K (R = 0.1 and f = 5 Hz) in water vapor at 67 Pa and 665 Pa.

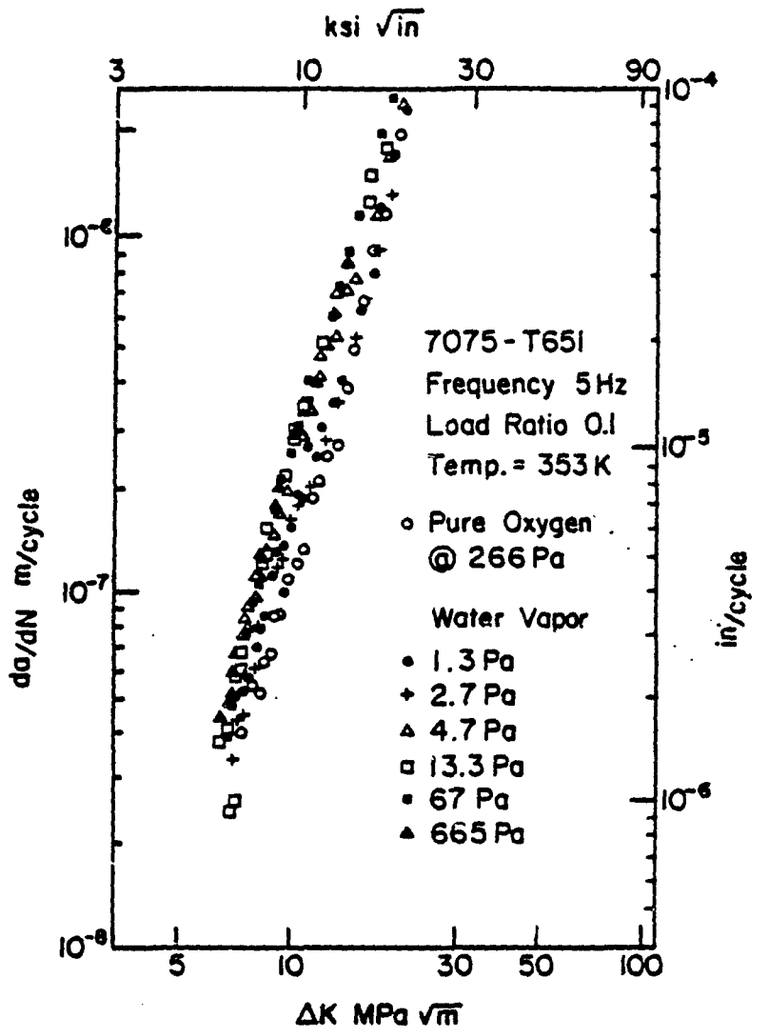

Fig. 32: Comparison of kinetics of fatigue crack growth in I/M 7075-T651 aluminum alloy at 354K in pure oxygen and in water vapor.

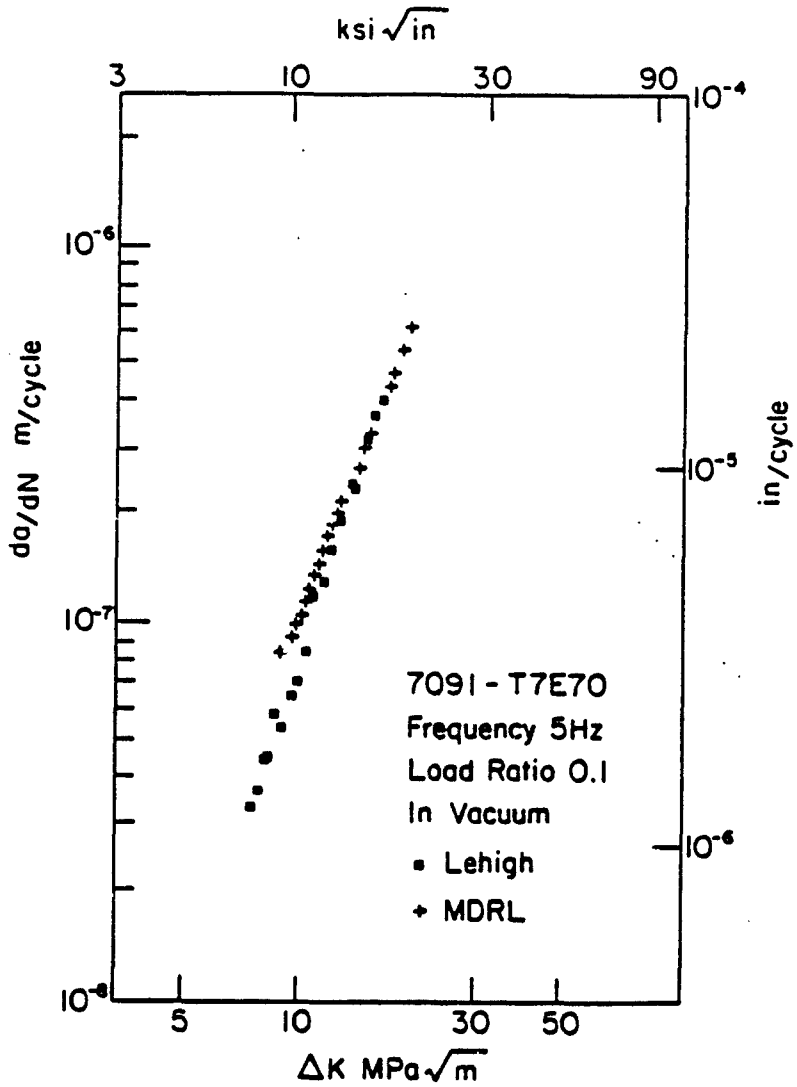

Fig. 33: Comparison of kinetics data of fatigue crack growth experiments in vacuum on P/M 7091-T7E70 aluminum alloy conducted at LU and MDRL.

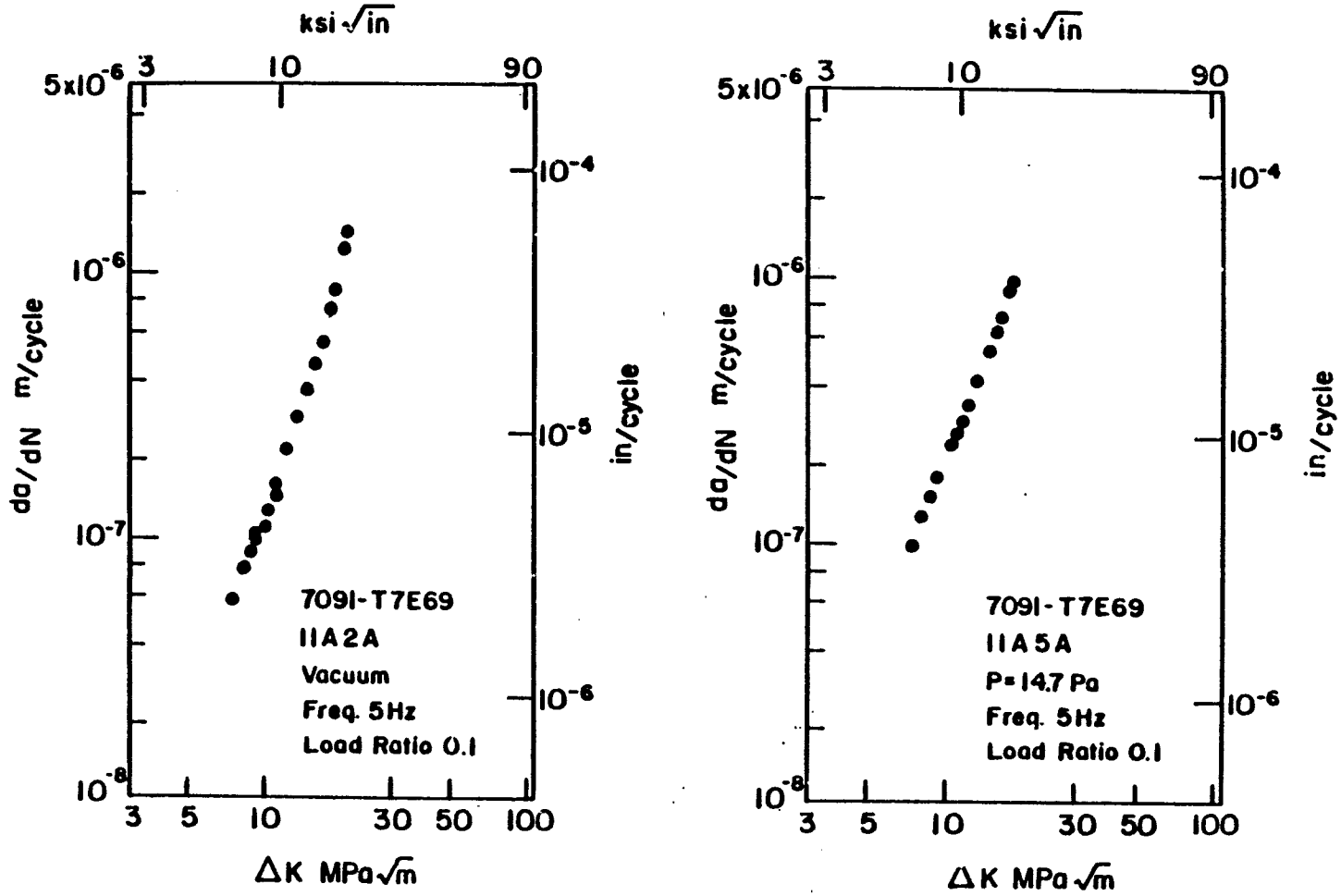

Fig. 34: Kinetics of fatigue crack growth for P/M 7091-T7E69 aluminum alloy (R = 0.1 and f = 5 Hz) in vacuum (<10^{-6} Pa) and in water vapor at 14.7 Pa.

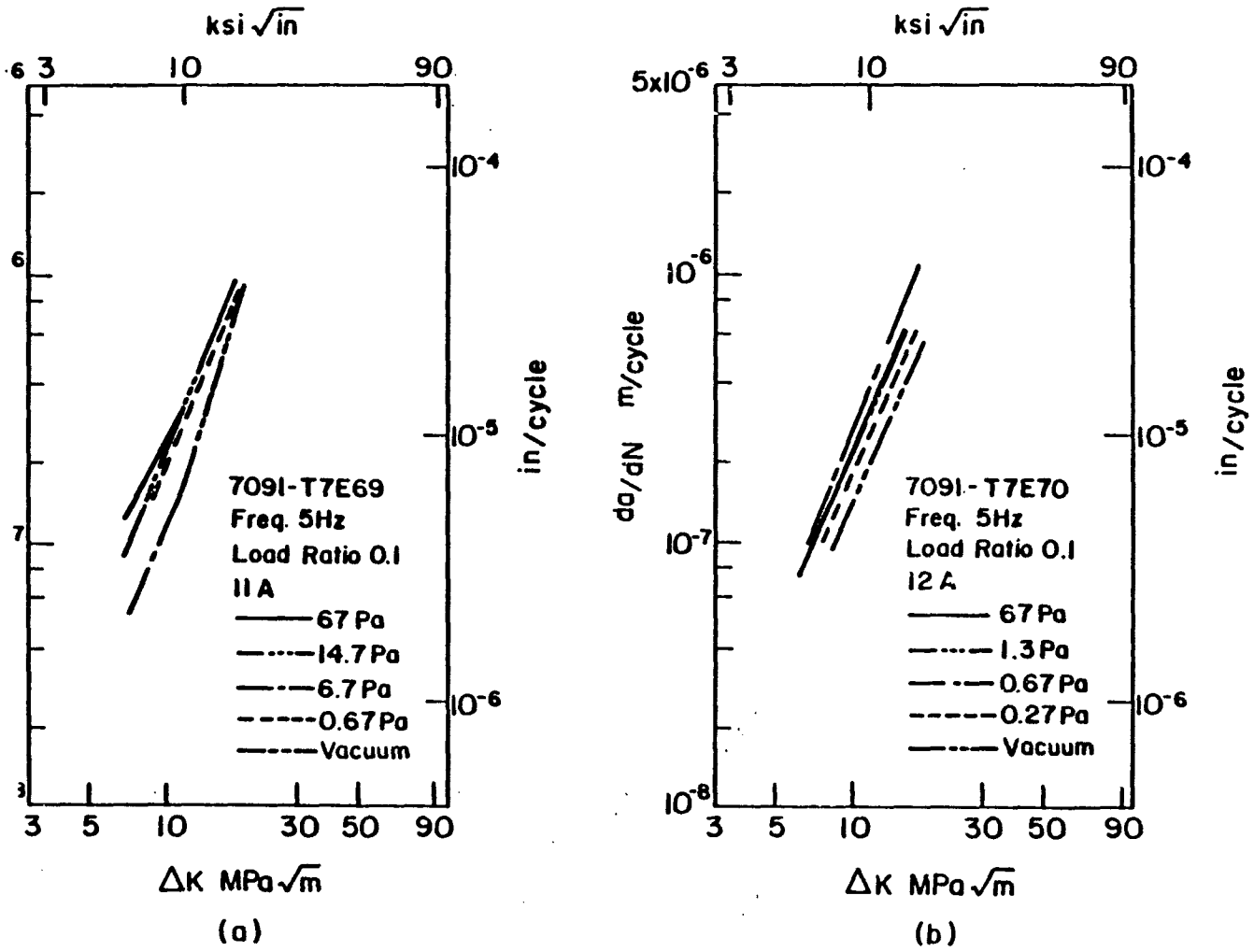

Fig. 35: Comparison of kinetics of fatigue crack growth in 7091-T7E69 and in 7091-T7E70 aluminum alloys tested in vacuum and water vapor environments: (a) 7091-T7E69, and (b) 7091-T7E70.

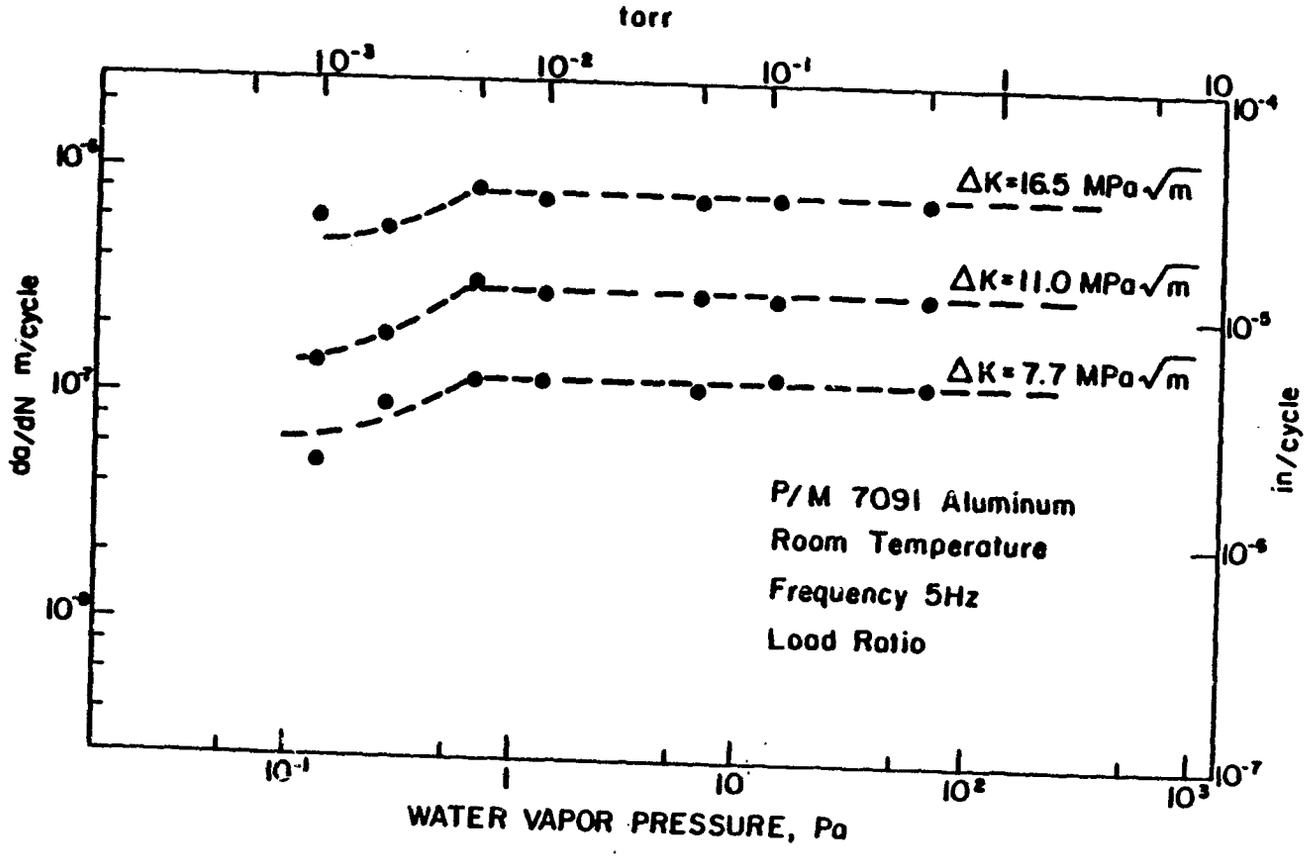

Fig. 36: Influence of water vapor pressure on the fatigue crack growth rate in P/M 7091 aluminum alloy.

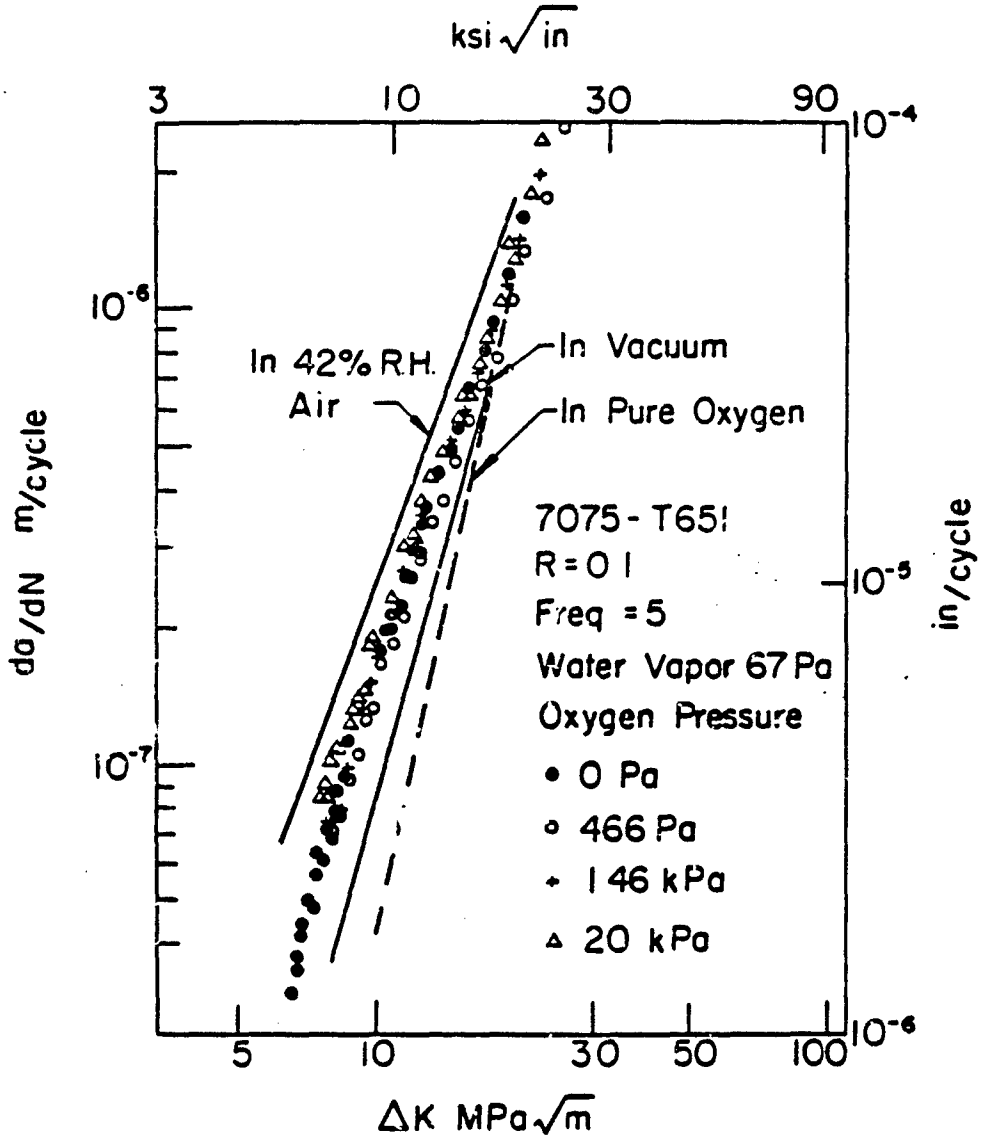

Fig. 37: Effect of oxygen pressure on fatigue crack growth kinetics in a binary gas mixture (P_{H_2O} = 67 Pa) for I/M 7075-T651 aluminum alloy.

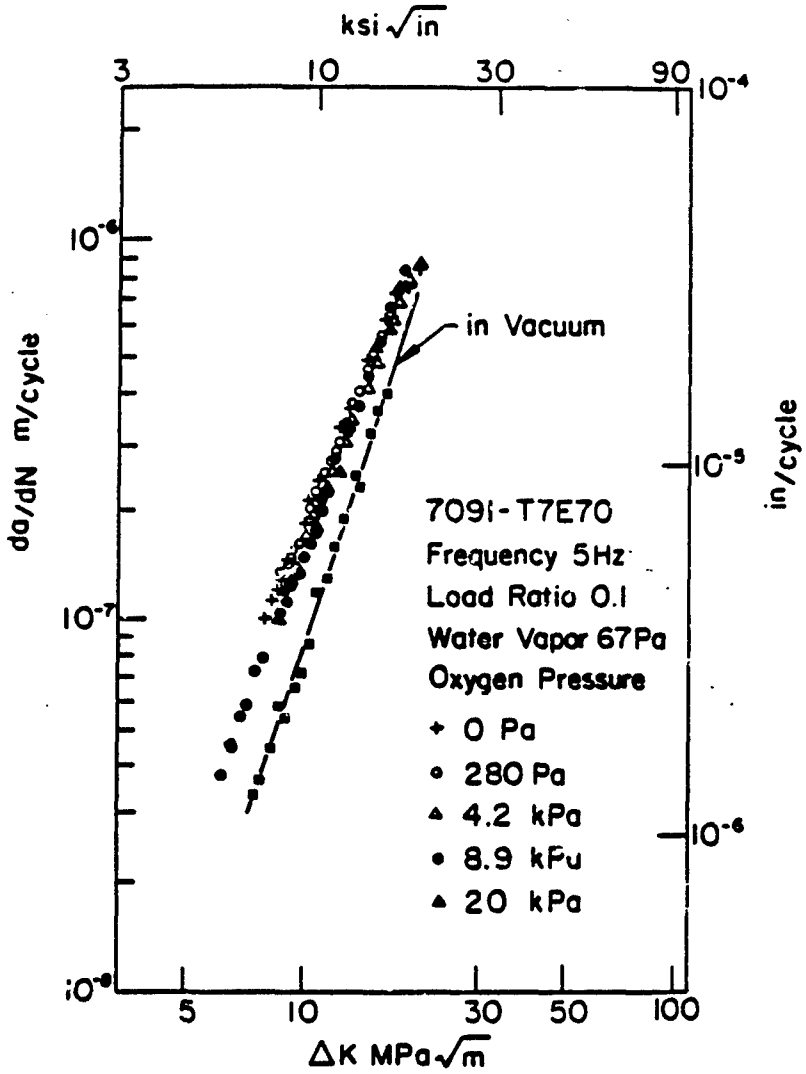

Fig. 38: Effect of oxygen pressure on fatigue crack growth in a binary gas mixture (P_{H_2O} = 67 Pa) for P/M 7091-T7E70 aluminum alloy.

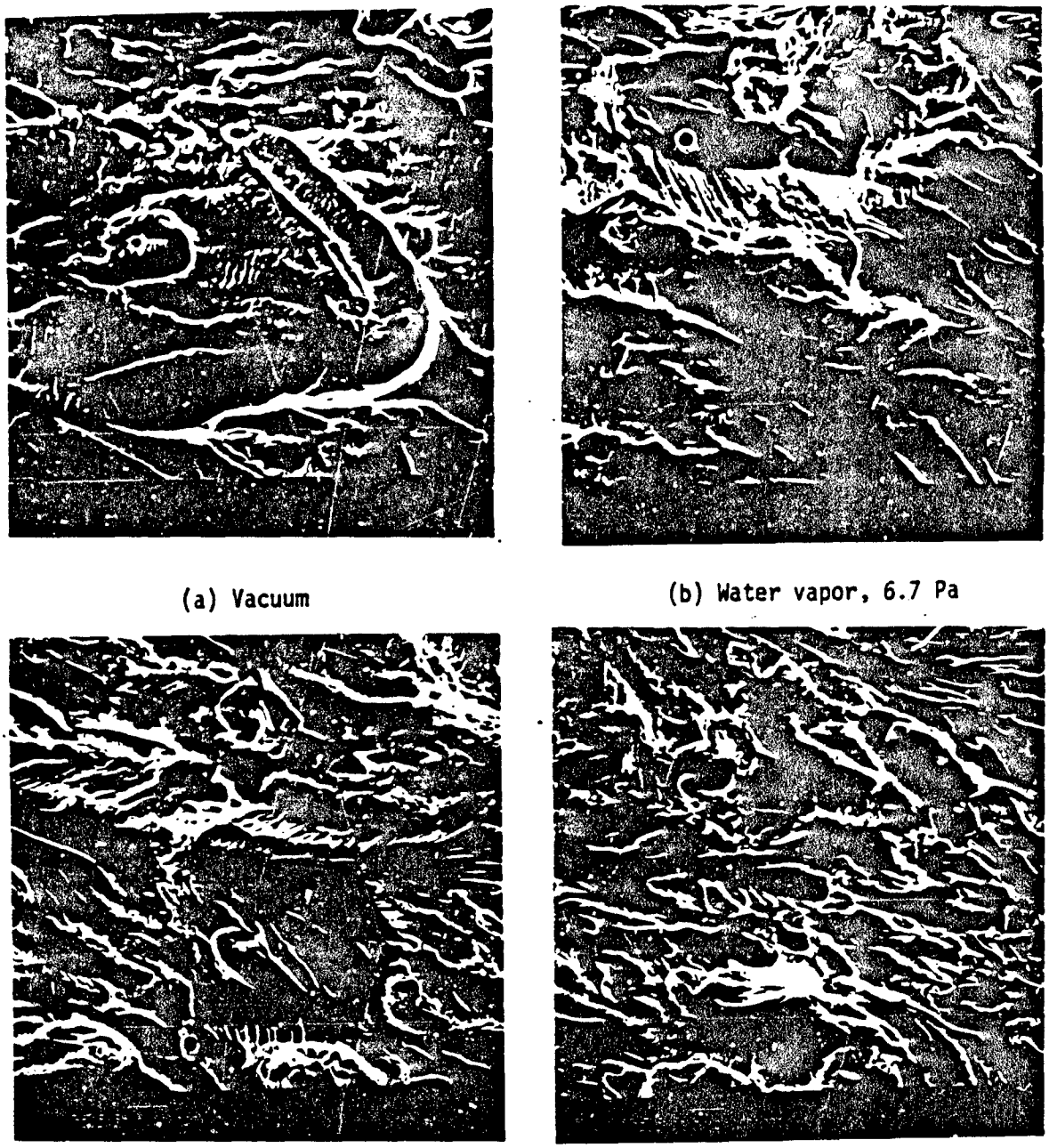

(a) Vacuum

(b) Water vapor, 6.7 Pa

(c) Water Vapor, 67 Pa

(d) Water

Fig. 39: Scanning electron microfractographs of 7050-T7451 aluminum alloy specimens tested in fatigue at room temperature at R = 0.1 (ΔK = 10 MPa$\sqrt{m}$): (a) in vacuum; (b) in water vapor at 6.7 Pa; (c) in water vapor at 67 Pa, and (d) distilled water.

(a) Vacuum

(b) Water vapor at 67 Pa

Fig. 40: Scanning electron microfractographs of 7050-T7451 aluminum alloy specimens tested in fatigue at room temperature at R = 0.5 (ΔK = 10 MPa$\sqrt{m}$): (a) in vacuum, and (b) in water vapor at 67 Pa.

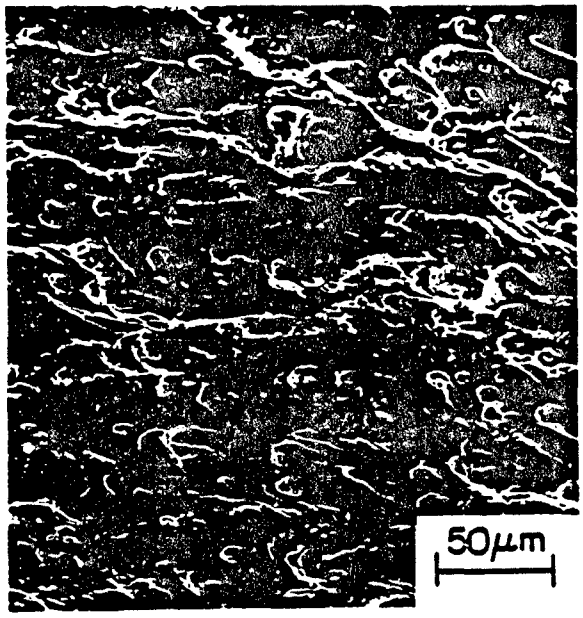

Fig. 41: SEM microfractographs of I/M 7075-T651 specimen tested in vacuum (ΔK = 11 MPa$\sqrt{m}$, R = 0.1 and f = 5 Hz), at low magnification.

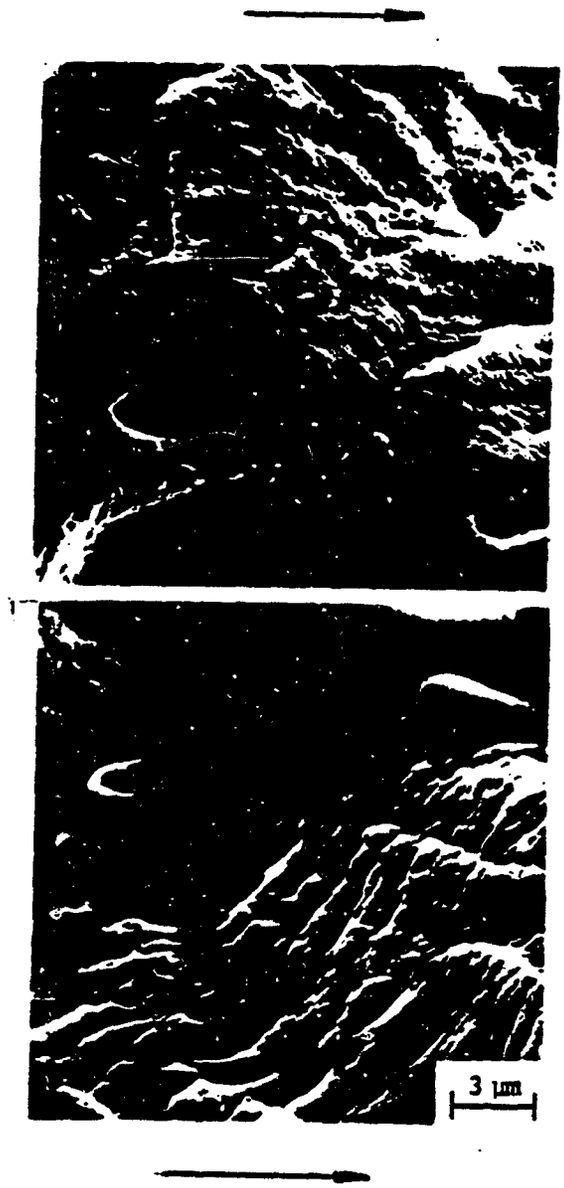

Fig. 42: SEM microfractographs from mating fracture surfaces at the area indicated by arrows in Fig. 41, showing the difference in fracture surface morphology.

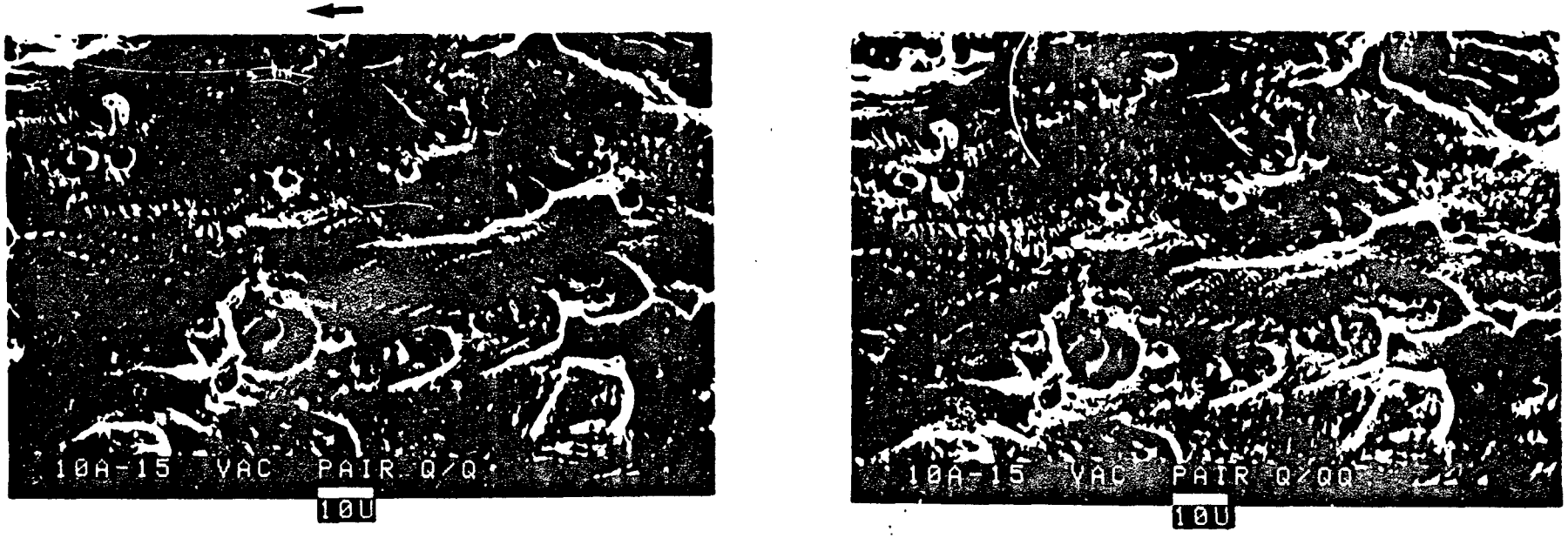

Fig. 43: Stereo pair of the fracture surface morphology for 7075-T651 tested in vacuum. The stereo pair of the mating half is shown in Fig. 44.

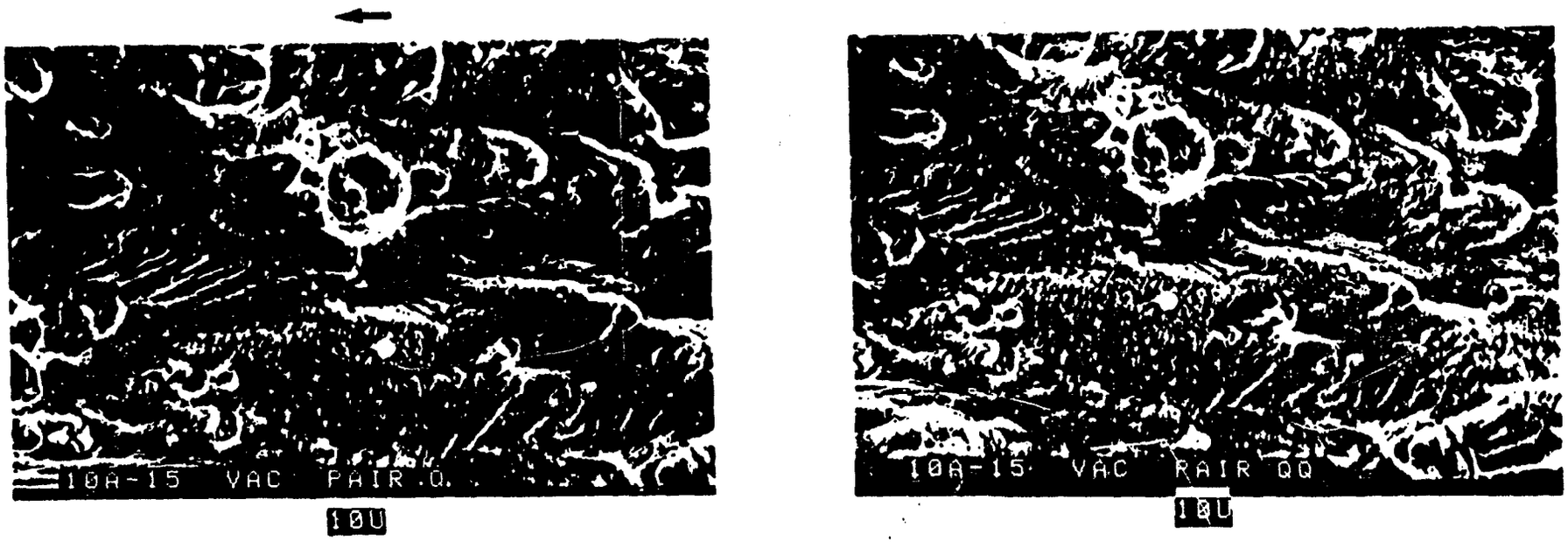

Fig. 44: Stereo pair of the fracture surface morphology for 7075-T651 tested in vacuum. The stereo pair of the mating half is shown in Fig. 43.

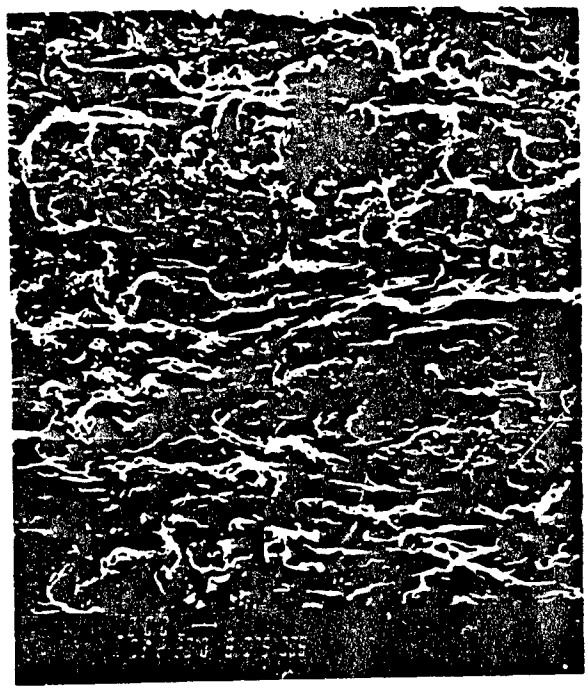

(a)

(b)

Fig. 45: SEM microfractographs of I/M 7075-T651 specimen tested in pure oxygen at 266 Pa (ΔK = 11 MPa$\sqrt{m}$, R = 0.1 and f = 5 Hz), a) 300X, and b) 600X.

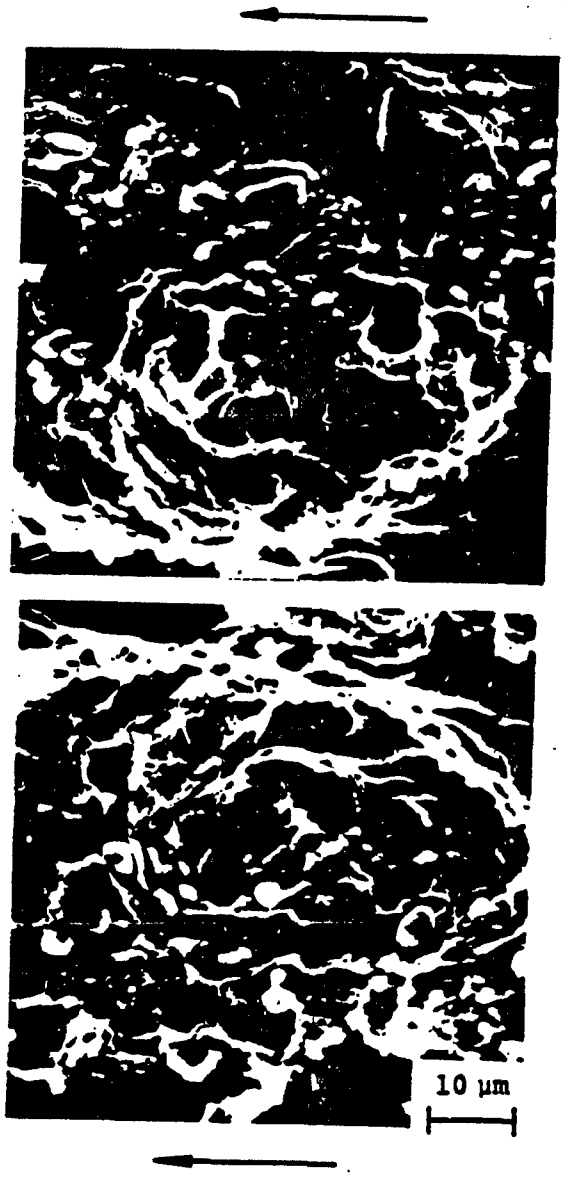

Fig. 16: SEM microfractographs from mating fracture surfaces tested in pure oxygen at 266 Pa (ΔK = 11 MPa$\sqrt{m}$, R = 0.1 and f = 5 Hz) showing particle-hole pairs. EDX spectrum shows that these particles are iron-rich.

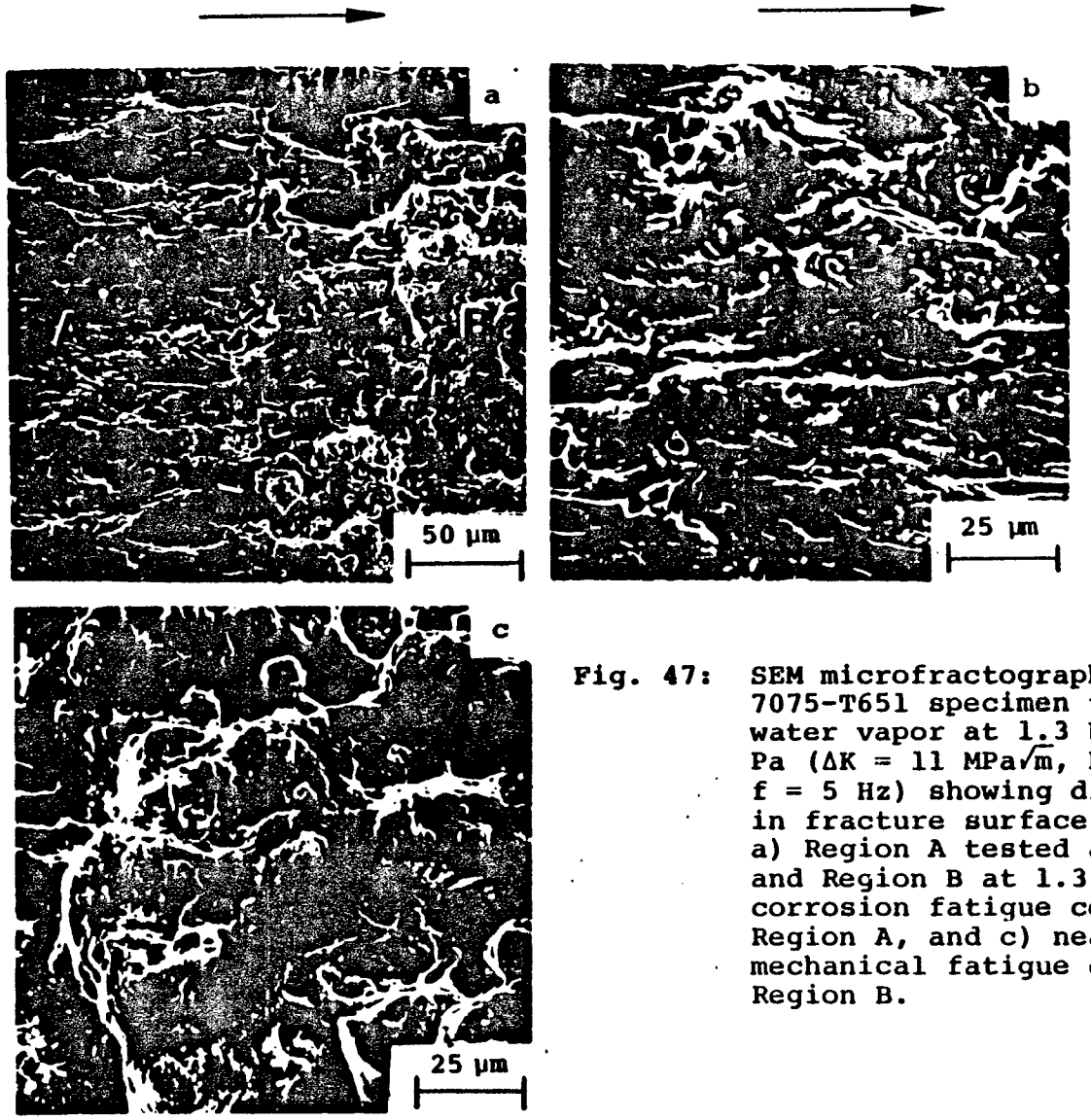

Fig. 47: SEM microfractographs of I/M 7075-T651 specimen tested in water vapor at 1.3 Pa and 670 Pa (ΔK = 11 MPa$\sqrt{m}$, R = 0.1 and f = 5 Hz) showing differences in fracture surface morphology. a) Region A tested at 670 Pa and Region B at 1.3 Pa; b) corrosion fatigue component, Region A, and c) near "pure" mechanical fatigue component, Region B.

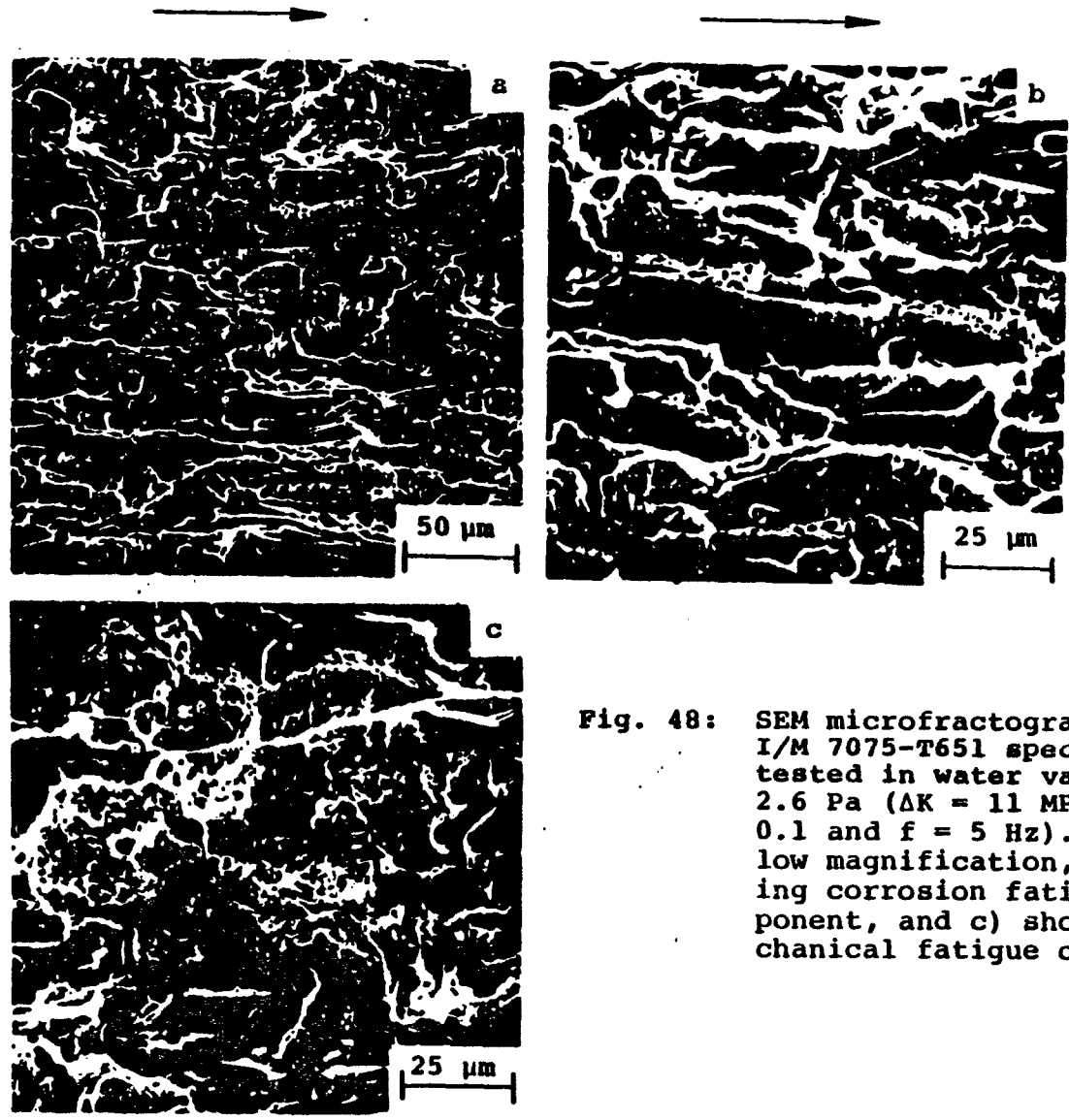

Fig. 48: SEM microfractographs of I/M 7075-T651 specimen tested in water vapor at 2.6 Pa (ΔK = 11 MPa$\sqrt{m}$, R = 0.1 and f = 5 Hz). a) at low magnification, b) showing corrosion fatigue component, and c) showing mechanical fatigue component.

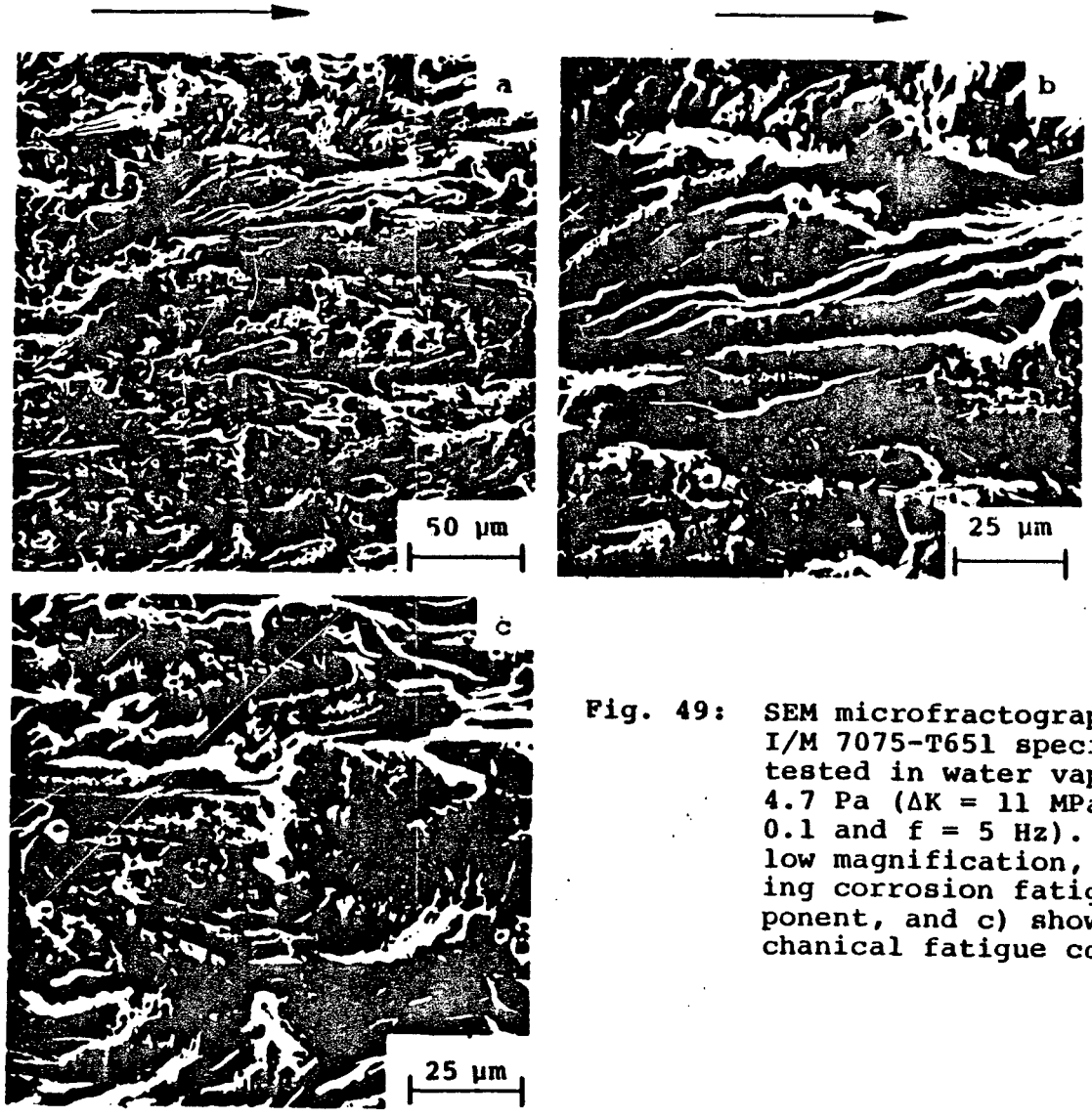

Fig. 49: SEM microfractographs of I/M 7075-T651 specimen tested in water vapor at 4.7 Pa (ΔK = 11 MPa$\sqrt{m}$, R = 0.1 and f = 5 Hz). a) at low magnification, b) showing corrosion fatigue component, and c) showing mechanical fatigue component.

(a)

(b)

Fig. 50: SEM microfractographs of I/M 7075-T651 specimen tested in water vapor at 67 Pa. (ΔK = 11 MPa$\sqrt{m}$, R = 0.1 and f = 5 Hz); a) 300X and b) 600X.

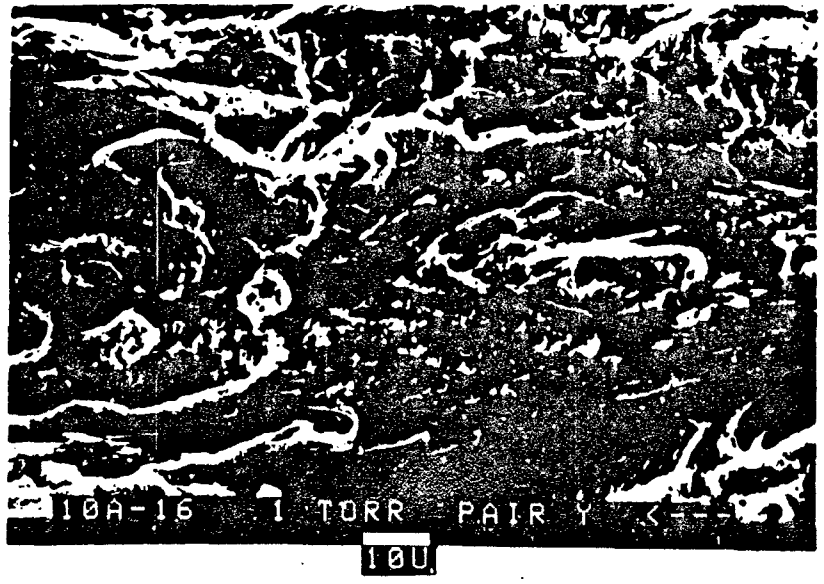

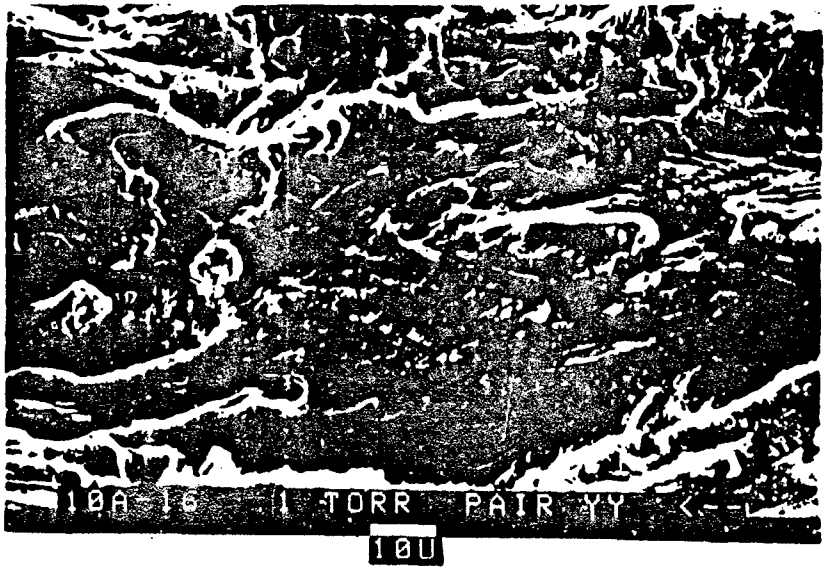

Fig. 51: Stereo pair of the fracture surface morphology for 7075-T651 tested at 133.3 Pa in water vapor. The stereo pair of the mating half is shown in Fig. 52.

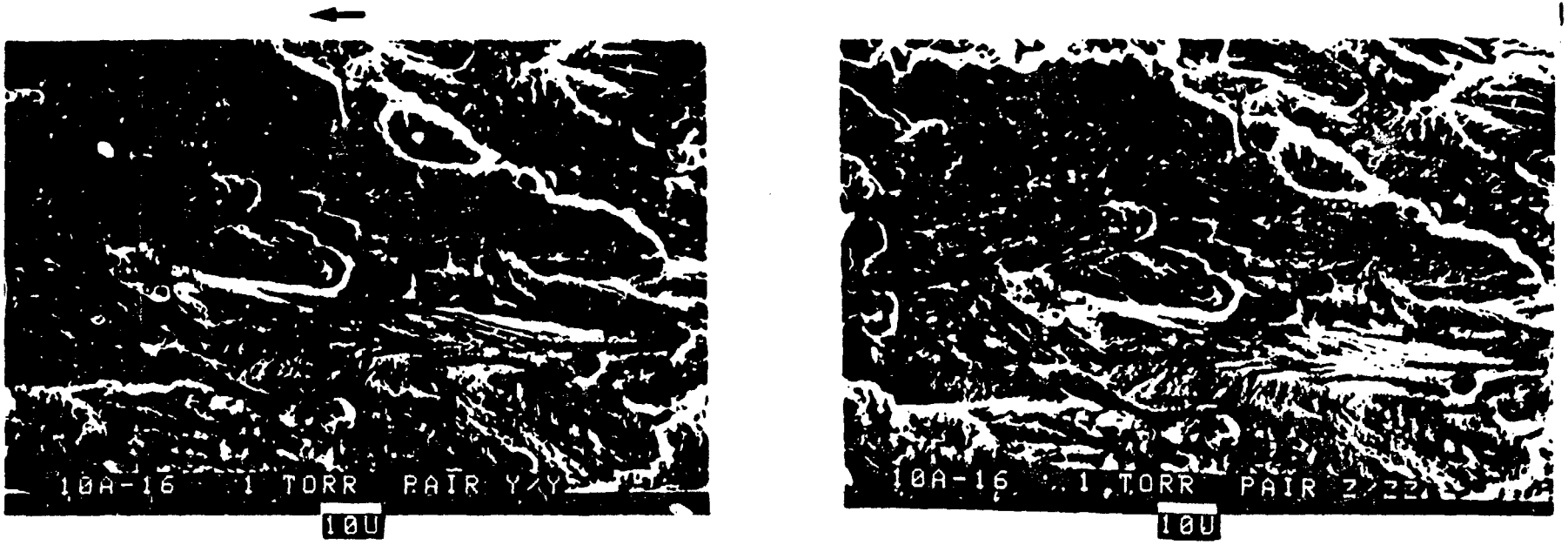

Fig. 52: Stereo pair of the fracture surface morphology for 7075-T651 tested at 133.3 Pa in water vapor. The stereo pair of the mating half is shown in Fig. 51.

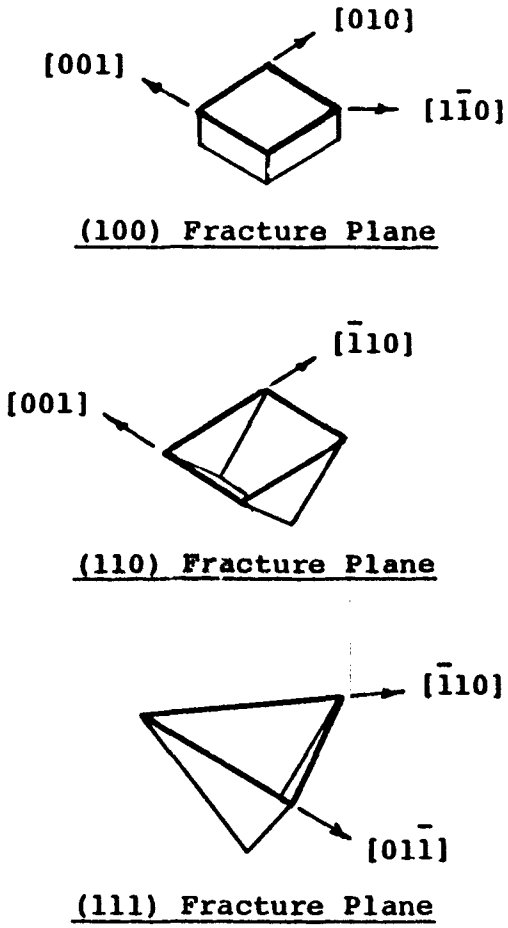

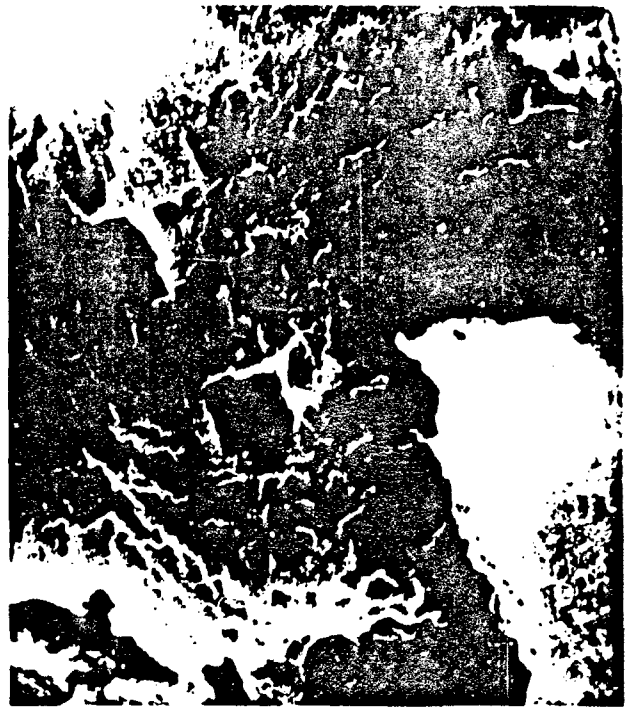

10,000X

Fig. 53: Comparison between etch pit geometry with that observed on a 7075-T651 aluminum alloy tested in air at room temperature to show correspondence with {100} fracture planes.

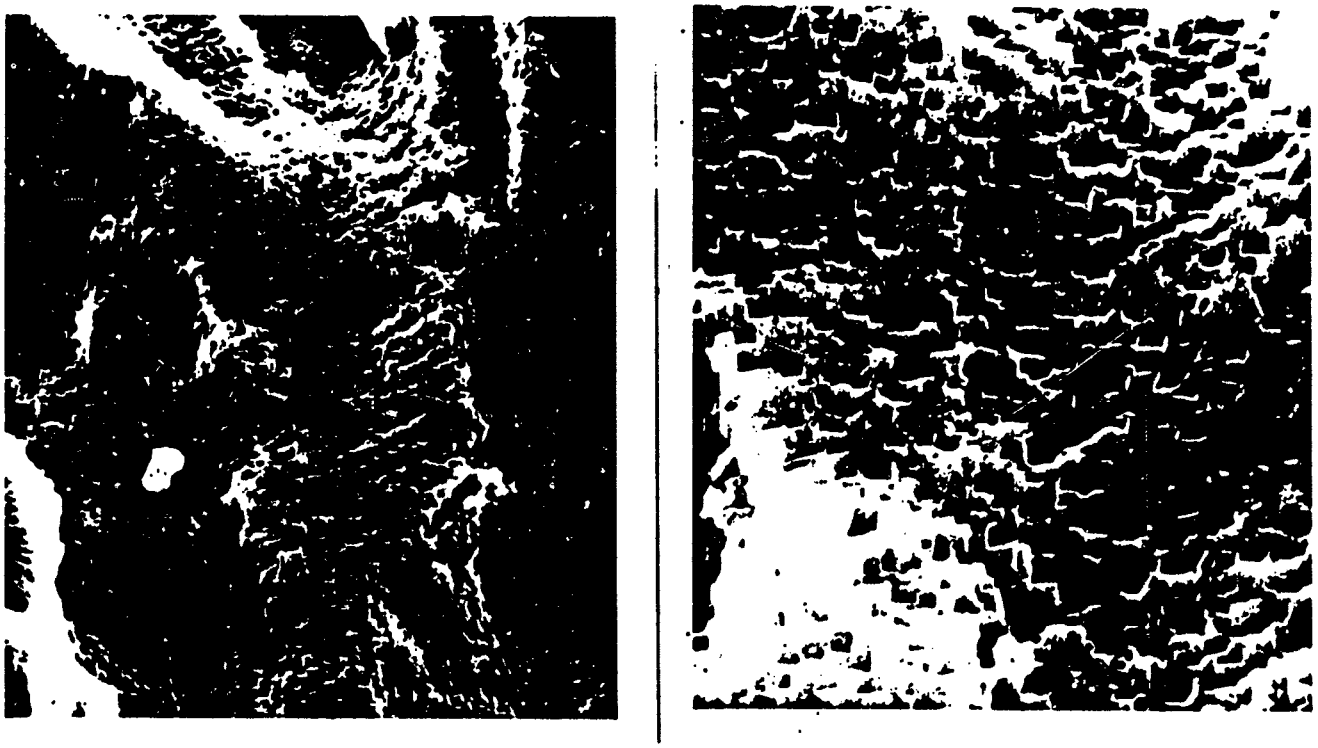

3,000X 10,000X

Fig. 54: Representative SEM microfractographs of etched surface of 7075-T651 aluminum alloy tested in air at room temperature showing alignment of striations approximately along <100> and <110> on {100} fracture planes.

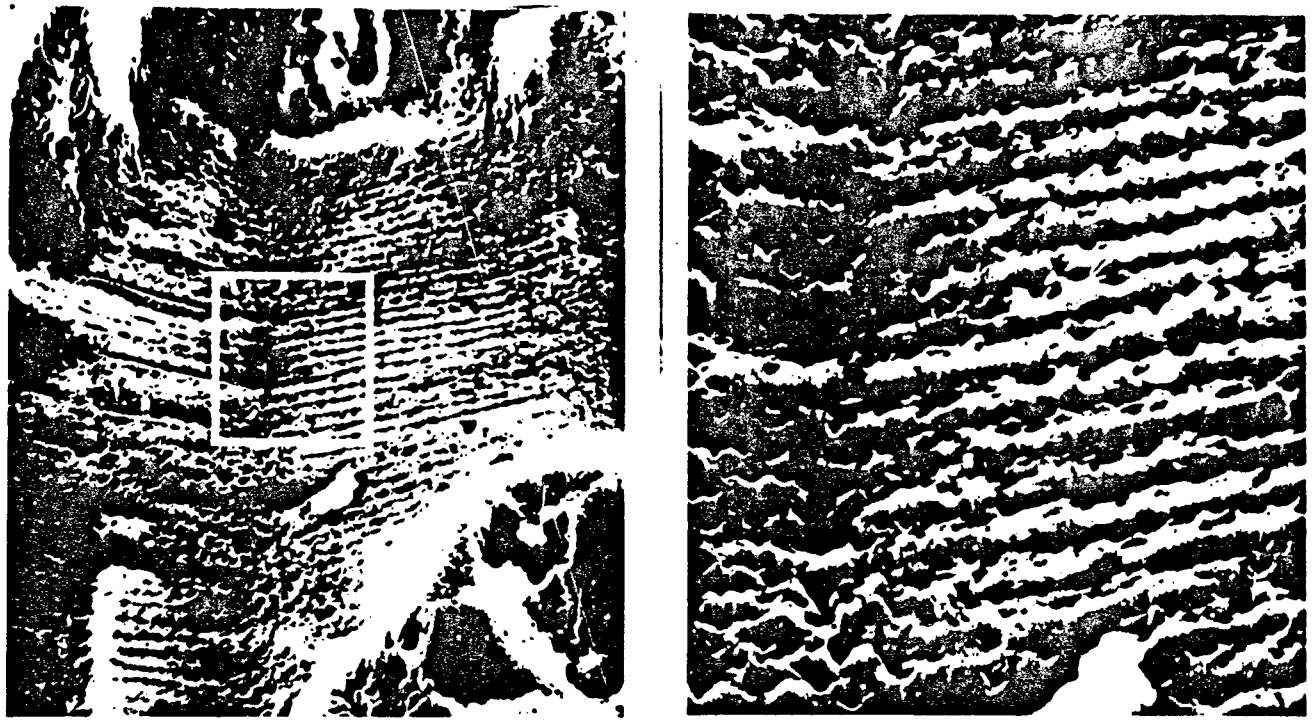

3,000X 10,000X

Fig. 55: Representative SEM microfractographs of etched surface of 7075-T651 aluminum alloy tested in air at room temperature showing alignment of striations along <110> on {100} fracture planes; although their orientations changed slightly from one subgrain to another.

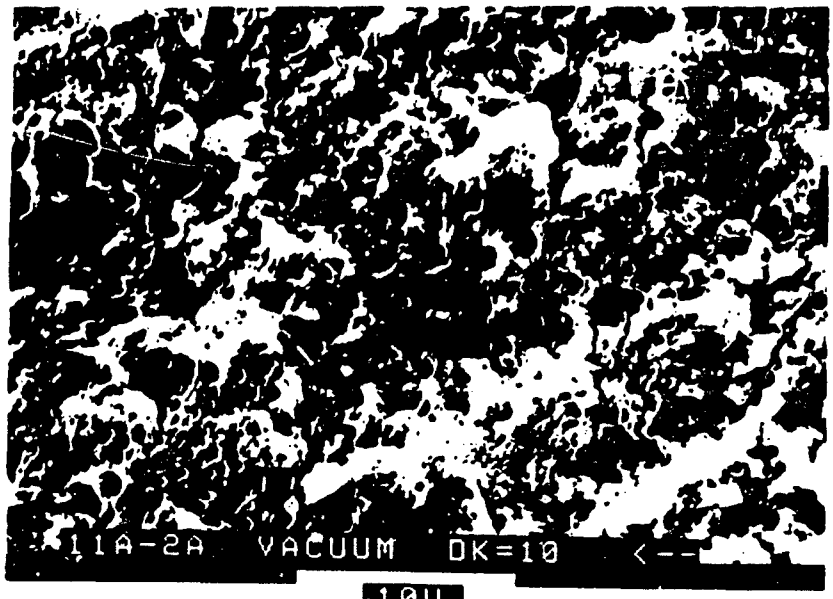

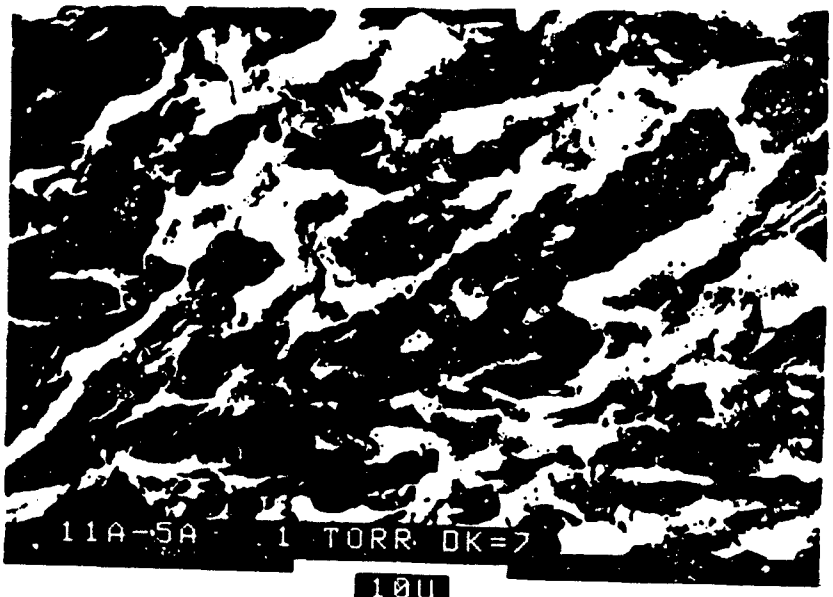

Fig. 56: SEM microfractographs of P/M 7091-T7E69 tested in (a) vacuum, and (b) 133.3 Pa in water vapor (R = 0.1 and f = 5 Hz).

(a)

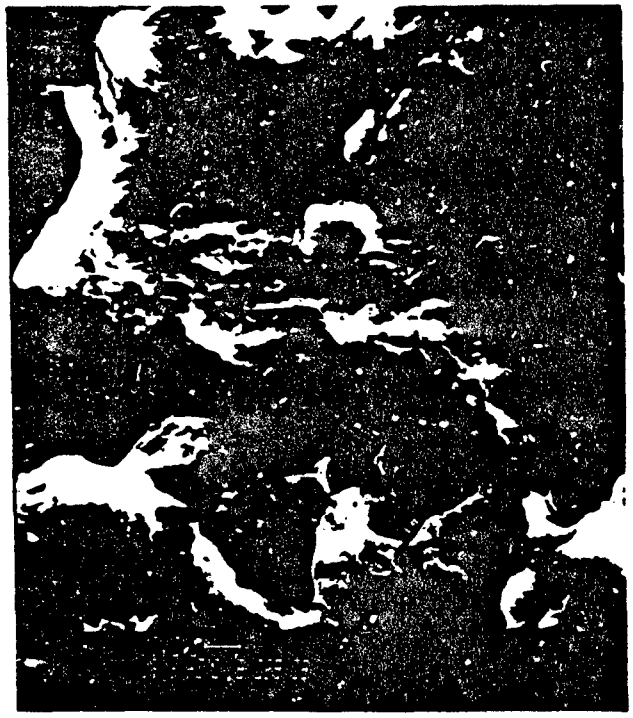

(b)

Fig. 57: SEM microfractographs of P/M 7091-T7E70 tested in pure oxygen (ΔK = 11 MPa$\sqrt{m}$, R = 0.1 and f = 5 Hz), a)1500X and b) 5000X.

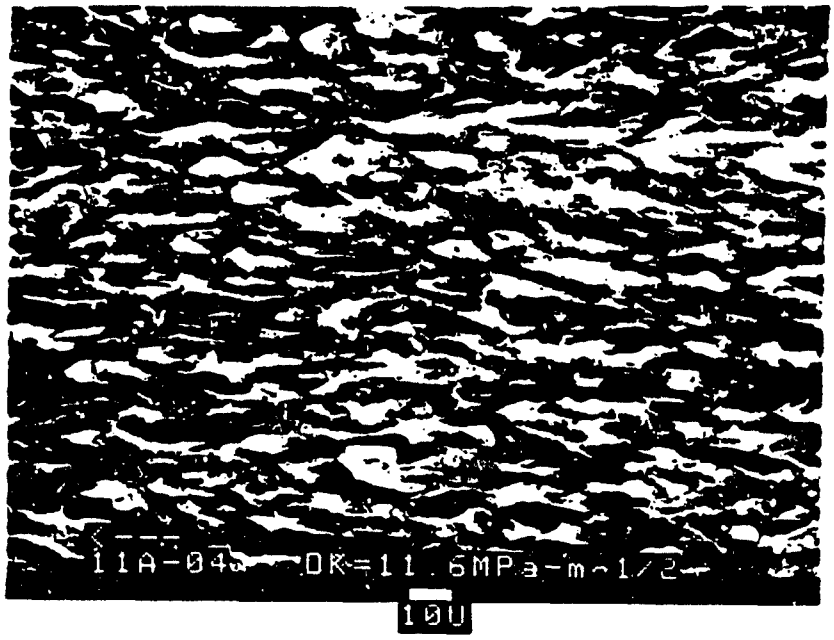

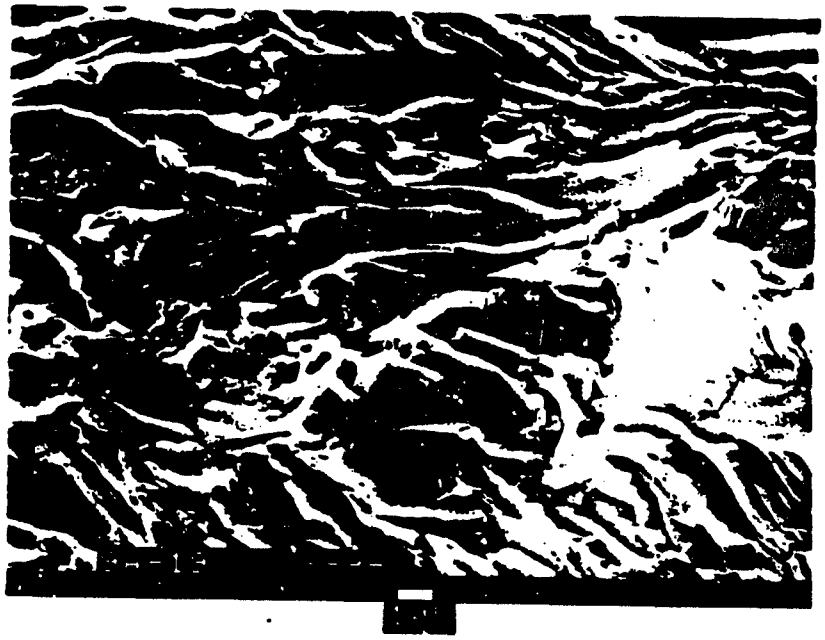

Fig. 58: Comparison of the fracture surface morphology of (a) P/M 7091-T7E69, and (b) I/M 7050-T7451. Both specimens were fatigue tested in water vapor environment (R = 0.1 and f = 5 Hz).

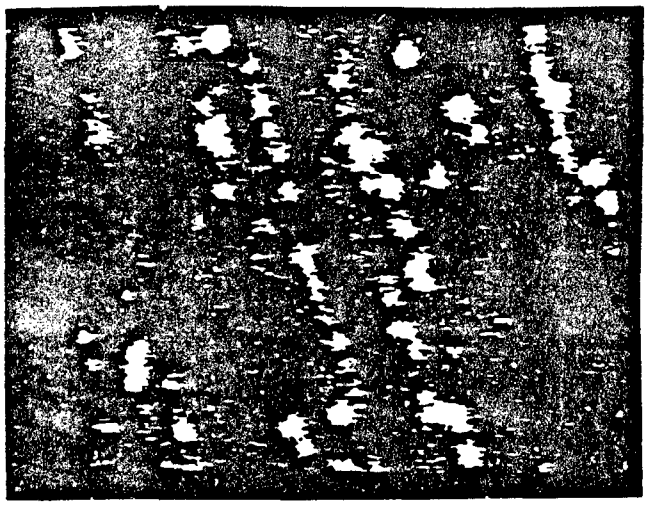

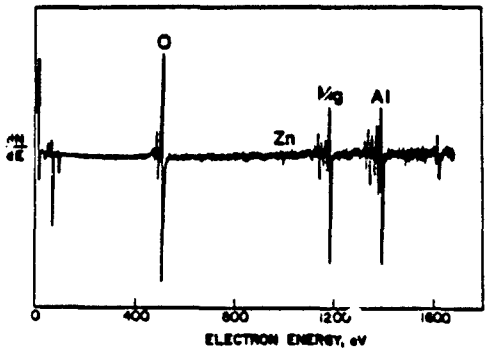

Fig. 59: Auger electron spectra and Auger map of impact fracture surface of a 7075-T651 aluminum alloy showing extensive segregation of magnesium.

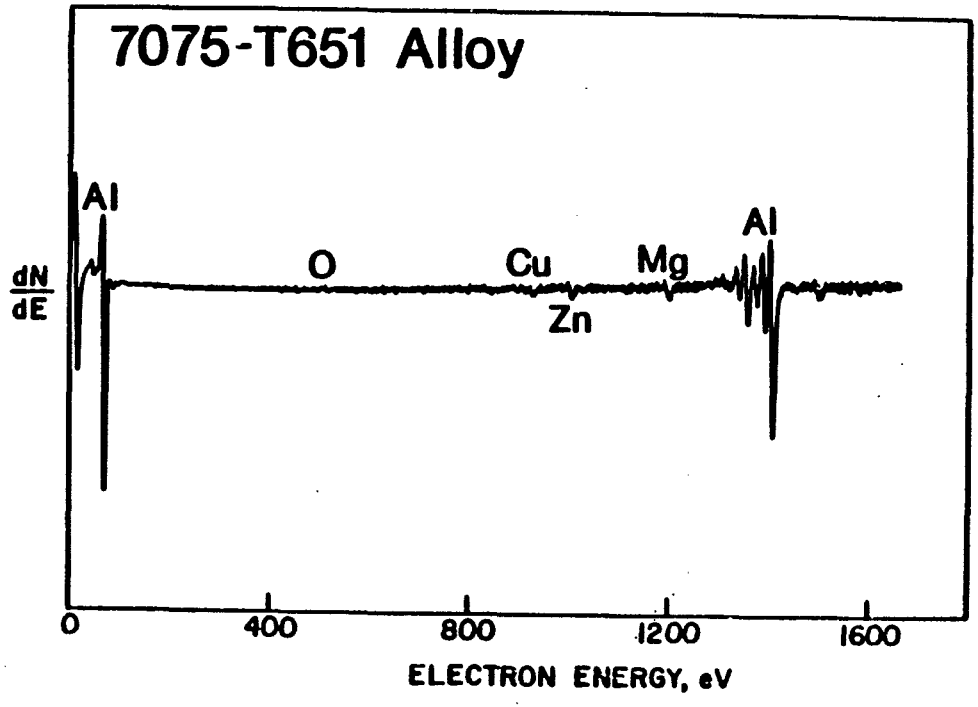

Fig. 60: Auger electron spectra of a "clean" surface of 7075-T651 aluminum alloy.

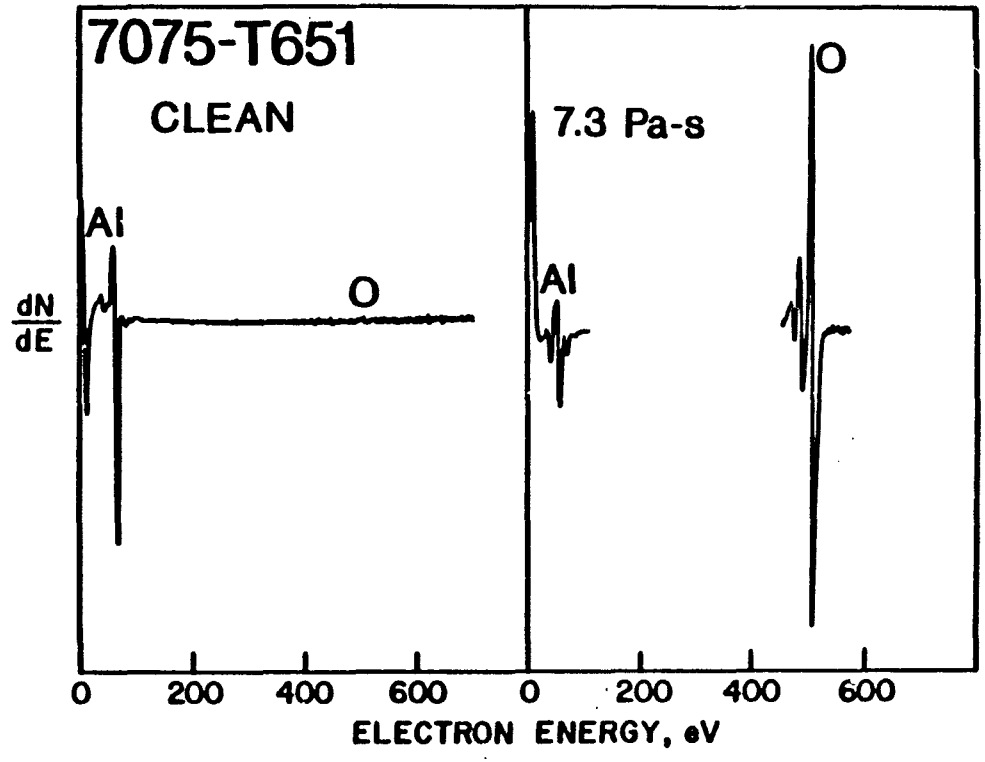

Fig. 61: Comparison of Auger electron spectra of 7075-T651 aluminum alloy before and after 7.3 Pa-s exposure to water vapor.

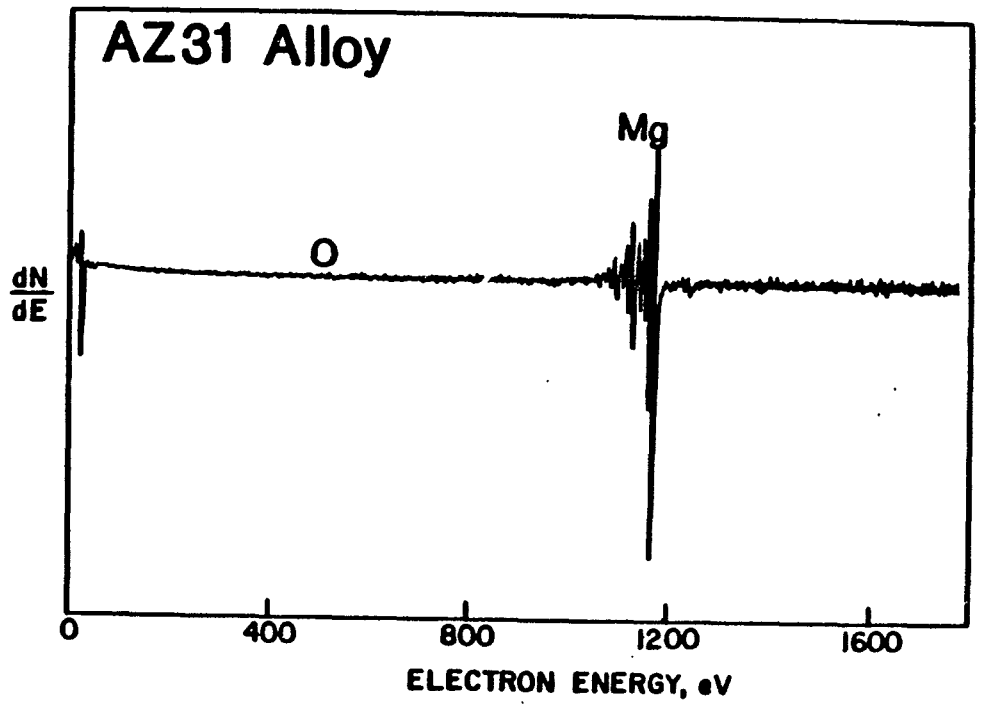

Fig. 62: Auger electron spectra of a "clean" surface of AZ31 magnesium alloy.

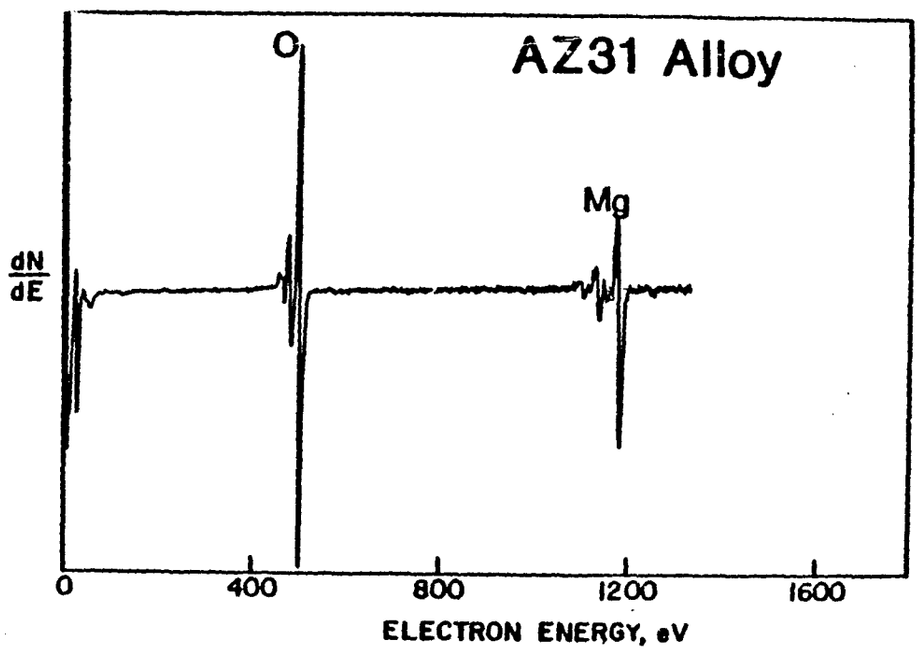

Fig. 63: Auger electron spectra of a surface of AZ31 magnesium alloy following 60 Pa-s exposure to water vapor.

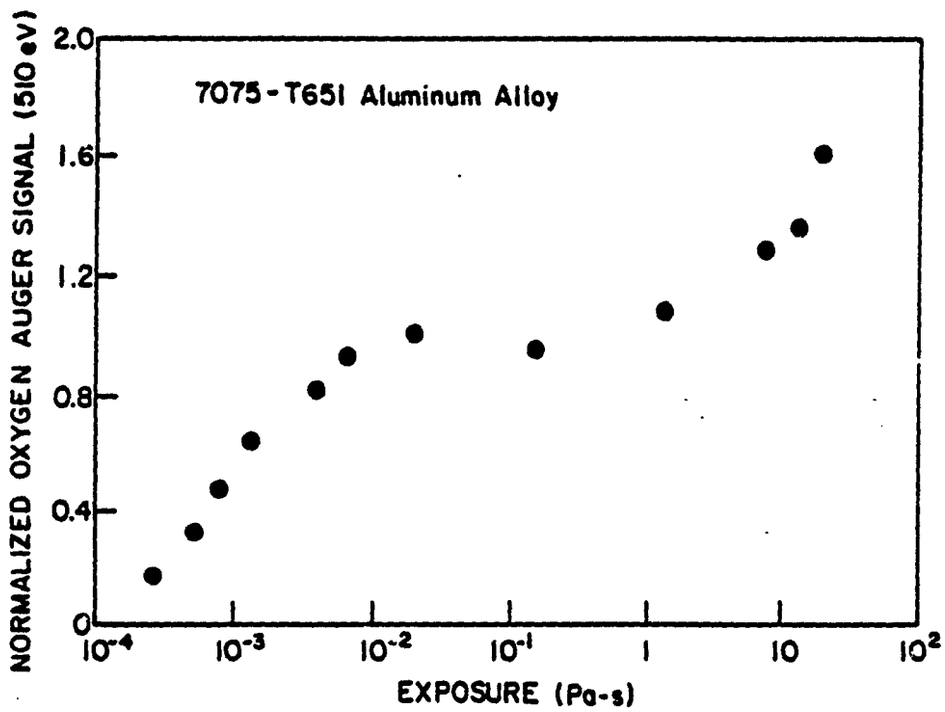

Fig. 64: Kinetics of reactions of water vapor with 7075-T651 aluminum alloy at room temperature, showing the contributions from a second reaction step [26].

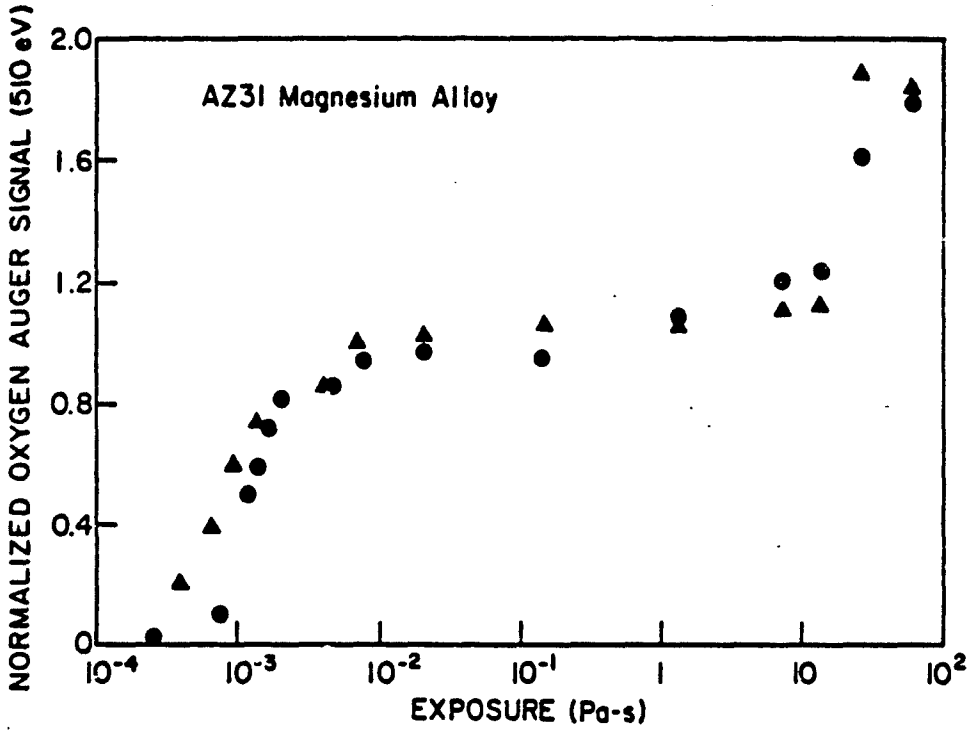

Fig. 65: Kinetics of reactions of water vapor with AZ31 magnesium alloy at room temperature, showing two reaction steps [26].

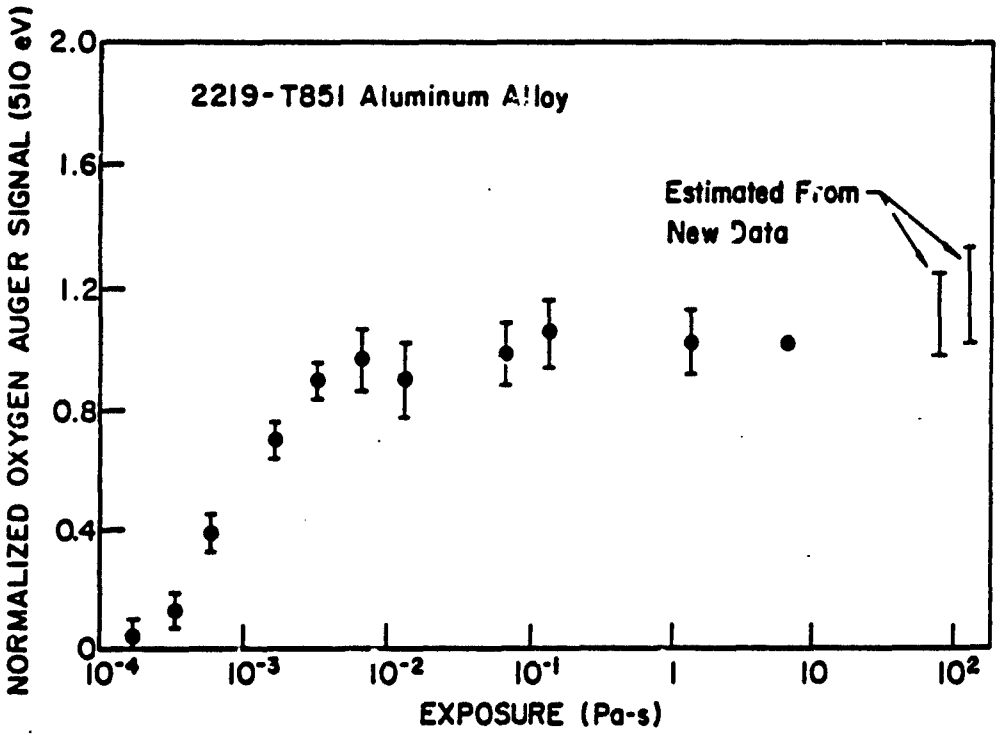

Fig. 66: Kinetics of reactions of water vapor with 2219-T851 aluminum alloy at room temperature, with no apparent second reaction step [1,26].

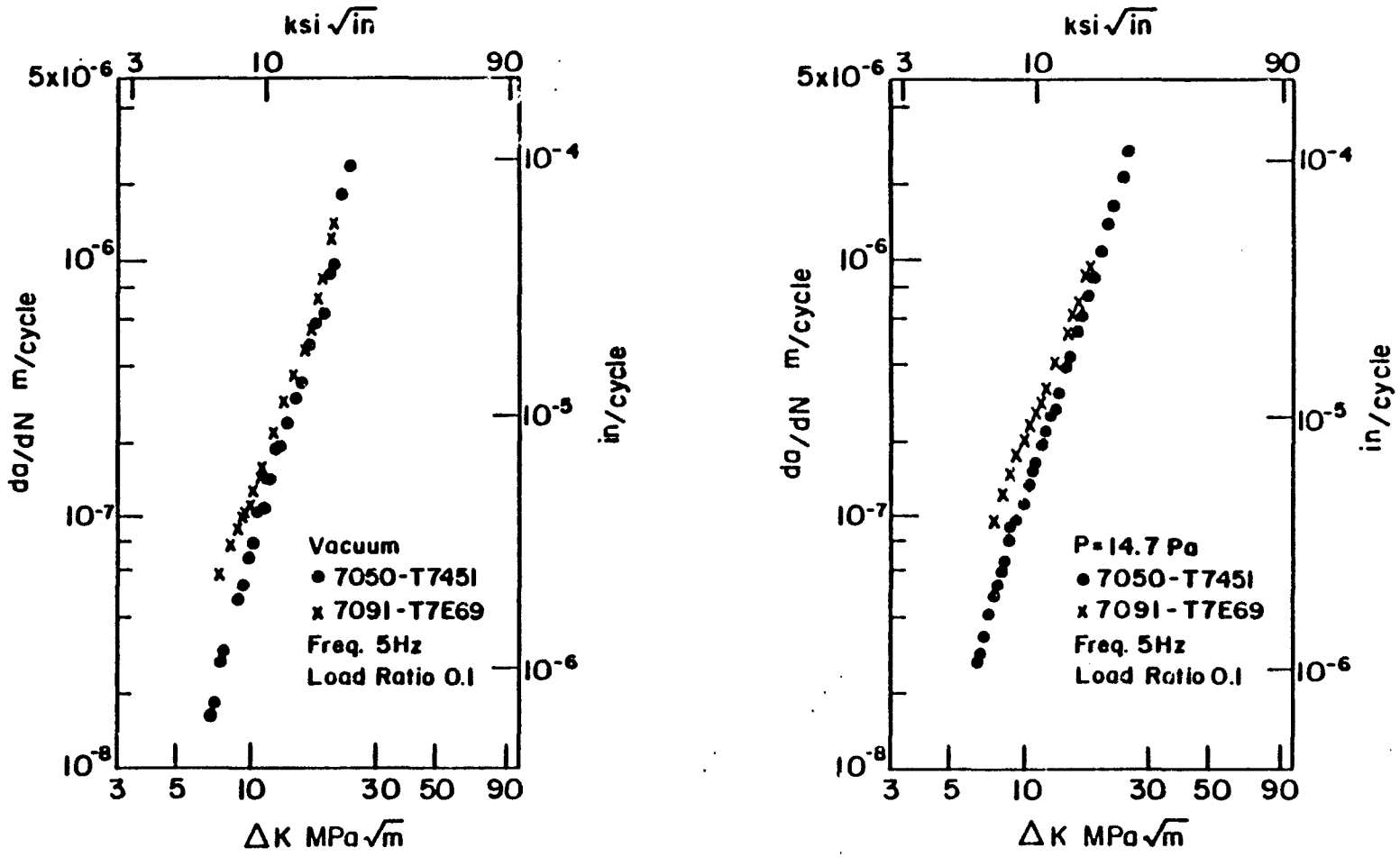

Fig. 67: Comparison of the kinetics of fatigue crack growth in I/M 7050-T7451 and in P/M 7091-T7E69 (R = 0.1 and f = 5 Hz) in vacuum ($<10^{-6}$ Pa) and in water vapor at 14.7 Pa.

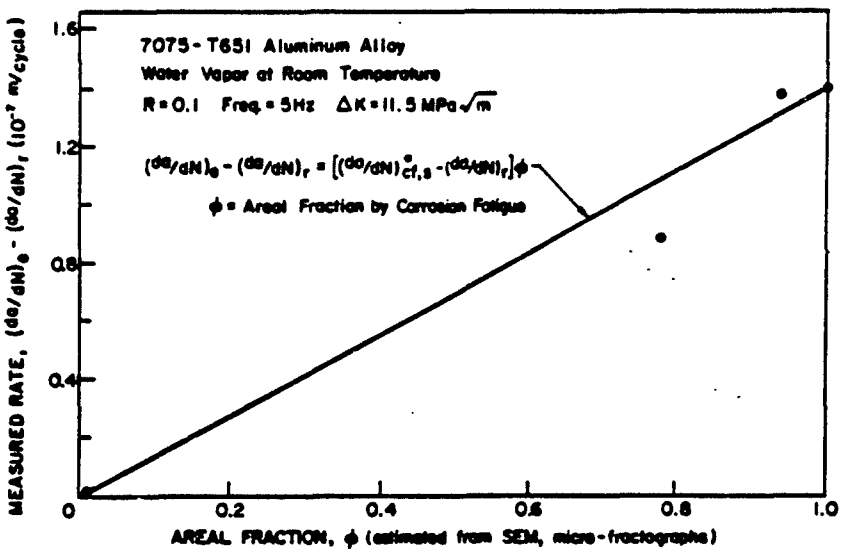

Fig. 68: Comparison between model predictions and fractographic observations on a 7075-T651 aluminum alloy tested in water vapor.

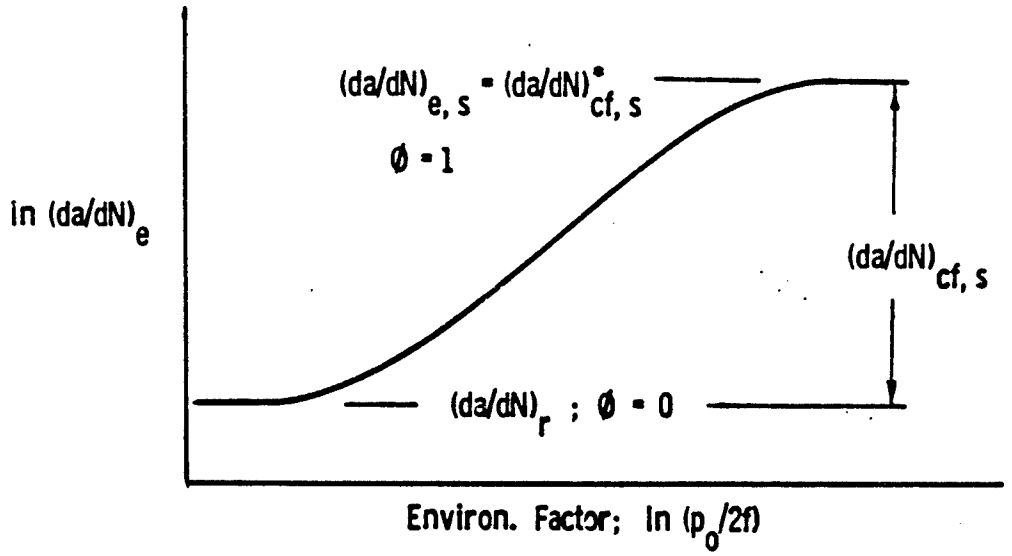

Fig. 69: Schematic illustration of environmentally assisted fatigue crack growth response and of the relationship between the various terms in the original and the modified models.

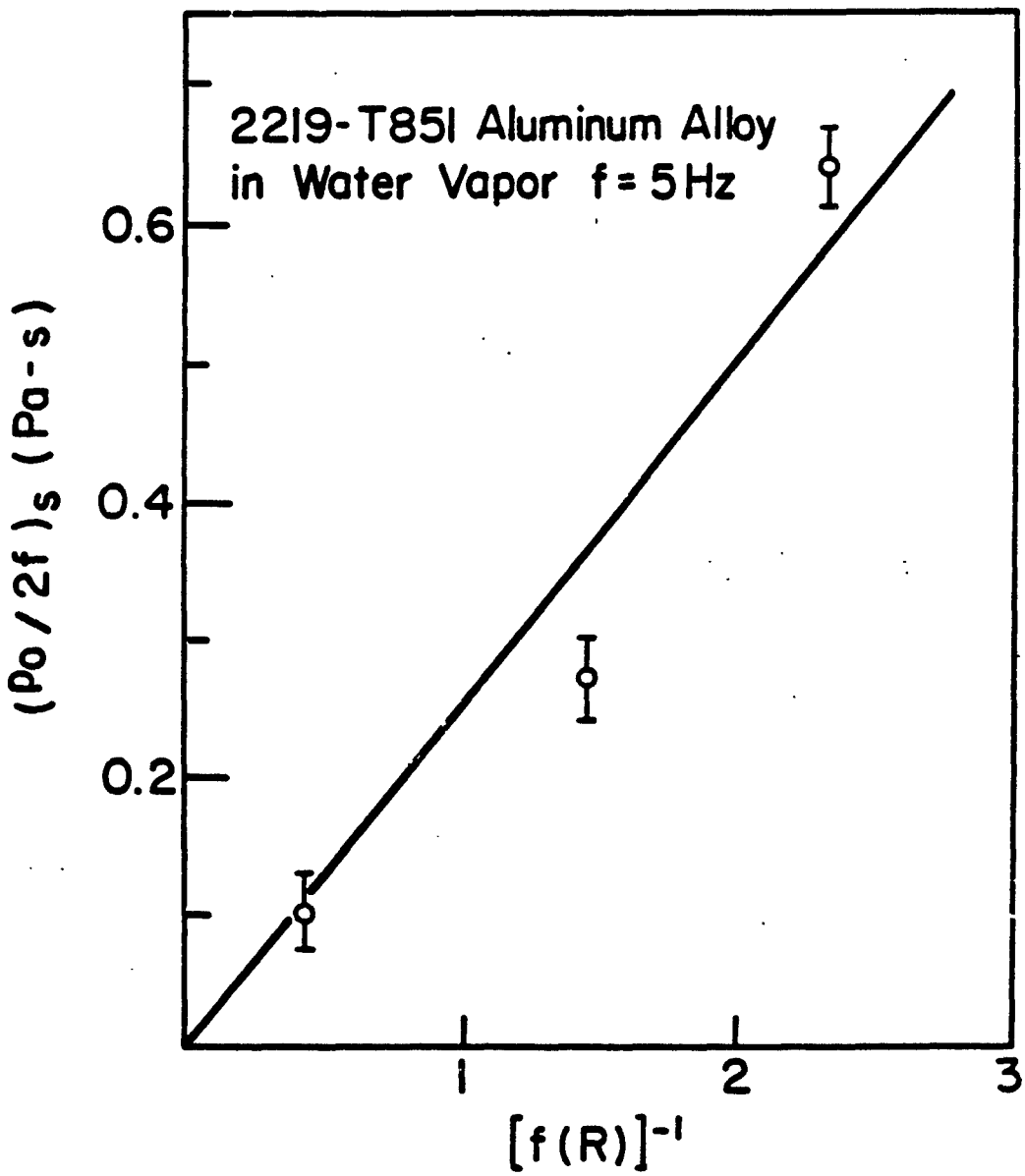

Fig. 70: Influence of load ratio on the saturation value of exposure in 2219-T851 aluminum alloy at room temperature. Solid line represents the best fit to the data.

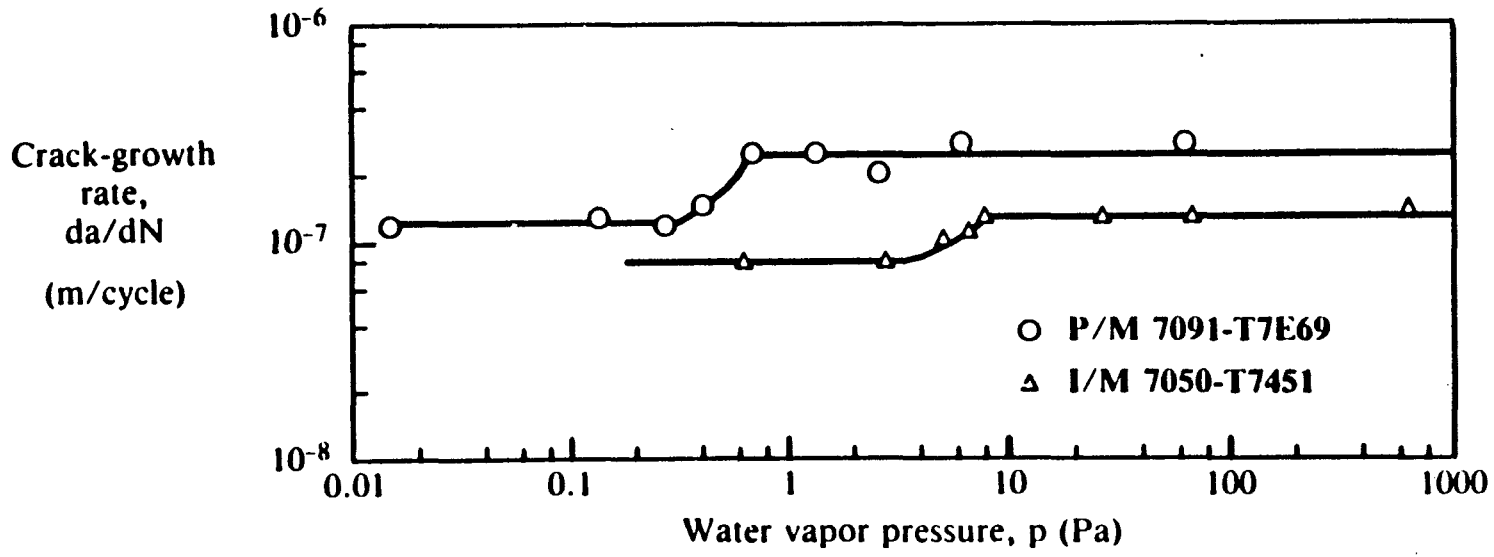

Fig. 71: Comparison of environmentally assisted fatigue crack growth response between P/M 7091-T7E69 and I/M 7050-T7451 aluminum alloys.

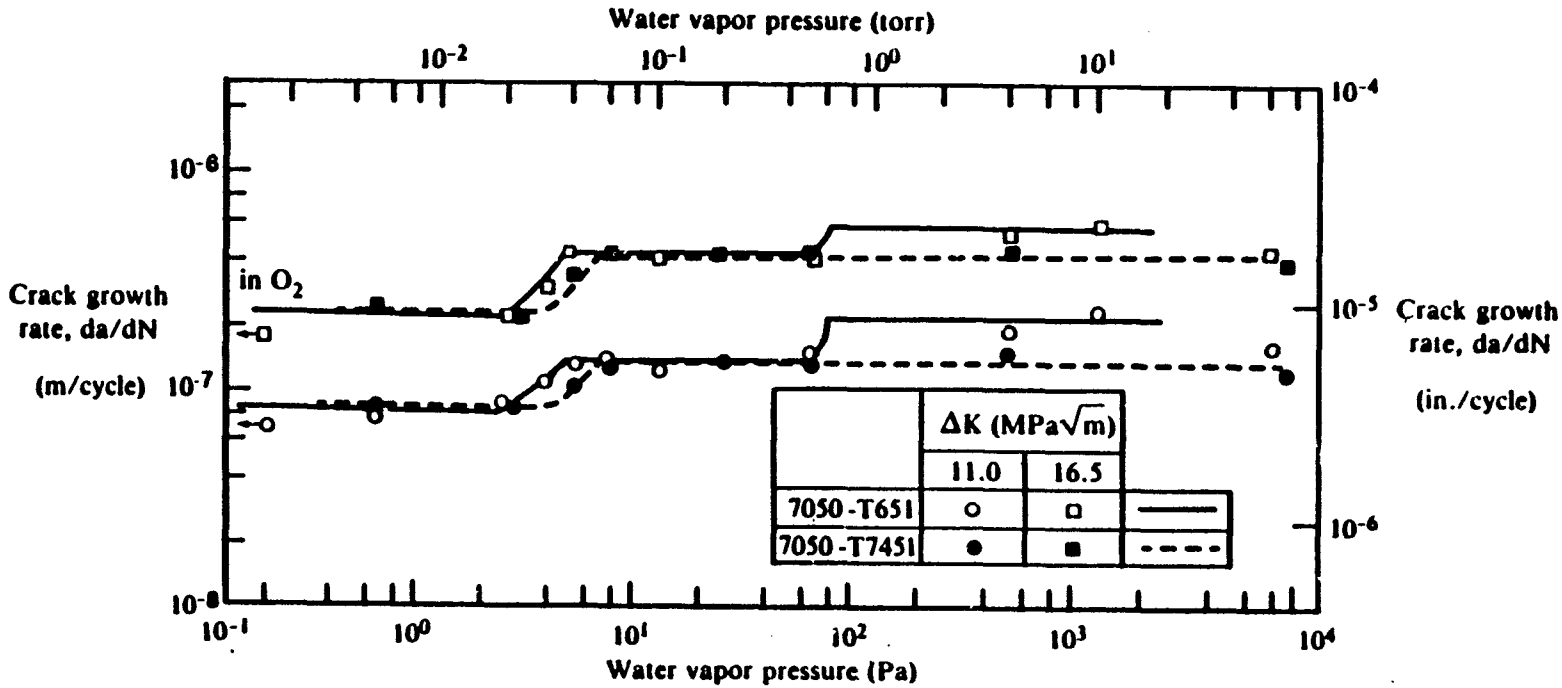

Fig. 72: Comparison of environmentally assisted fatigue crack growth response between 7075-T651 and 7050-T7451 aluminum alloys.

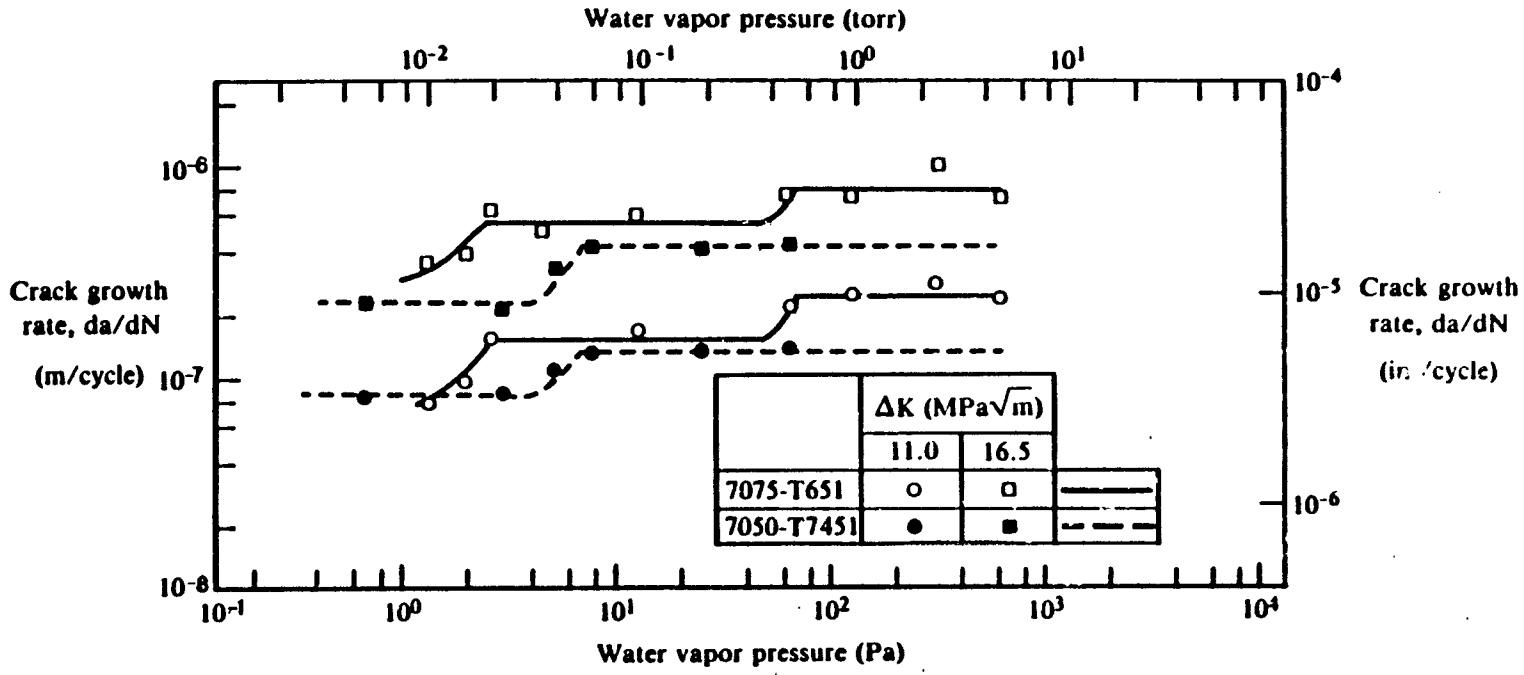

Fig. 73: Comparison of environmentally assisted fatigue crack growth response between 7050-T651 and 7050-T7451 aluminum alloys.

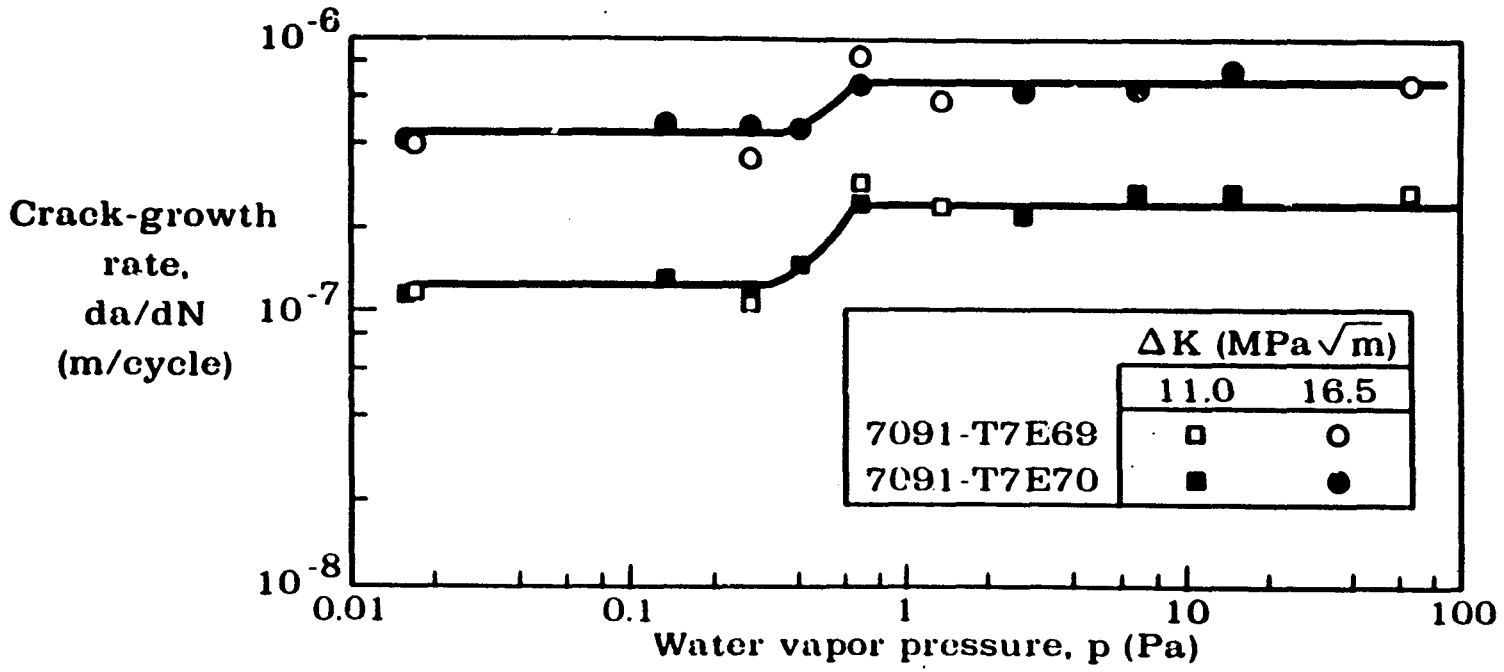

Fig. 74: Comparison of environmentally assisted fatigue crack growth response between 7091-T7E69 and 7091-T7E70 aluminum alloys.

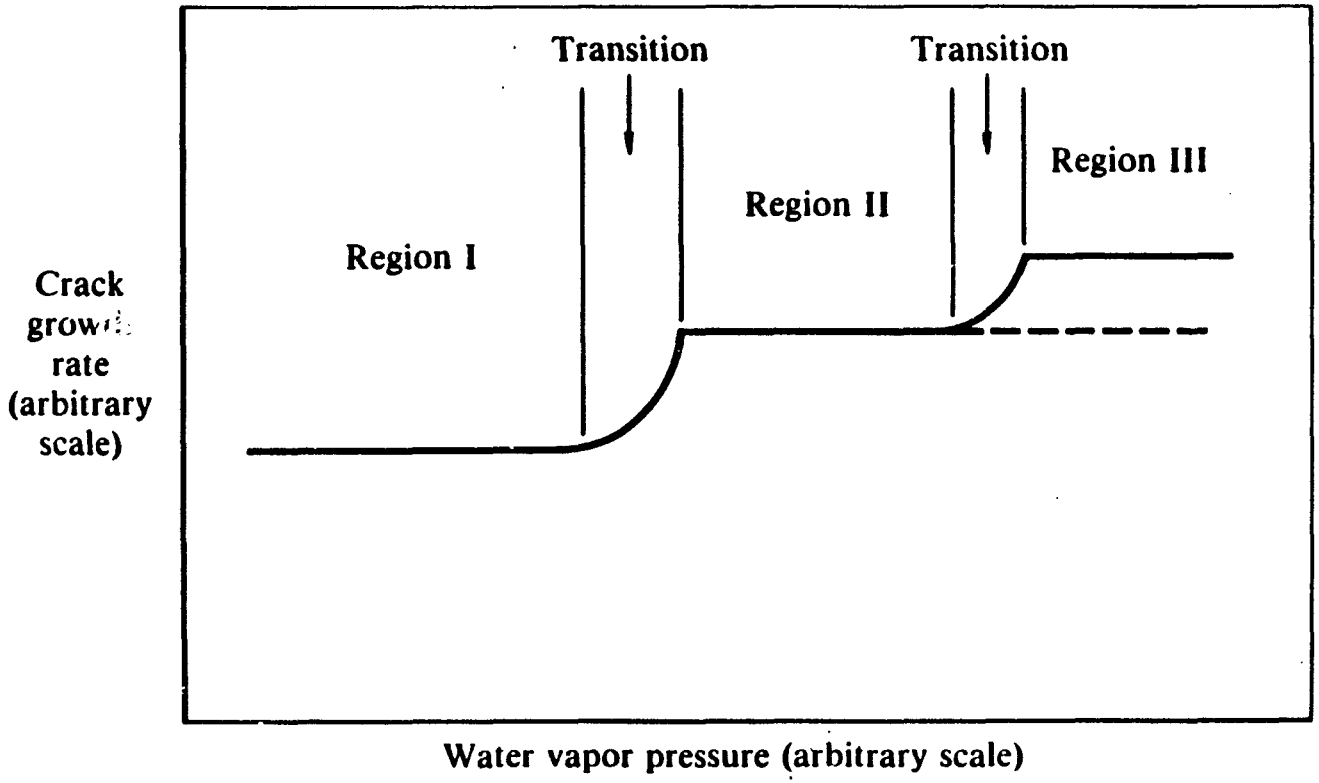

Fig. 75: Schematic diagram of fatigue crack growth response in high strength aluminum alloys.

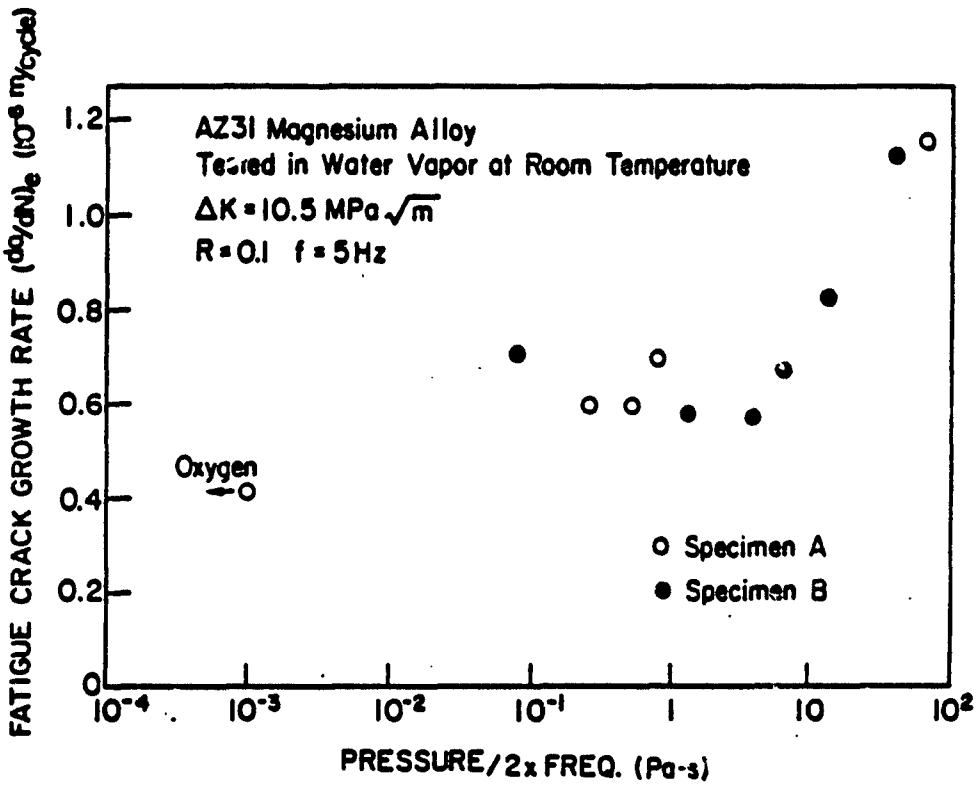

Fig. 76: The effect of water vapor pressure (or pressure/2xfrequency) on fatigue crack growth in AZ31 magnesium alloy at room temperature [26].

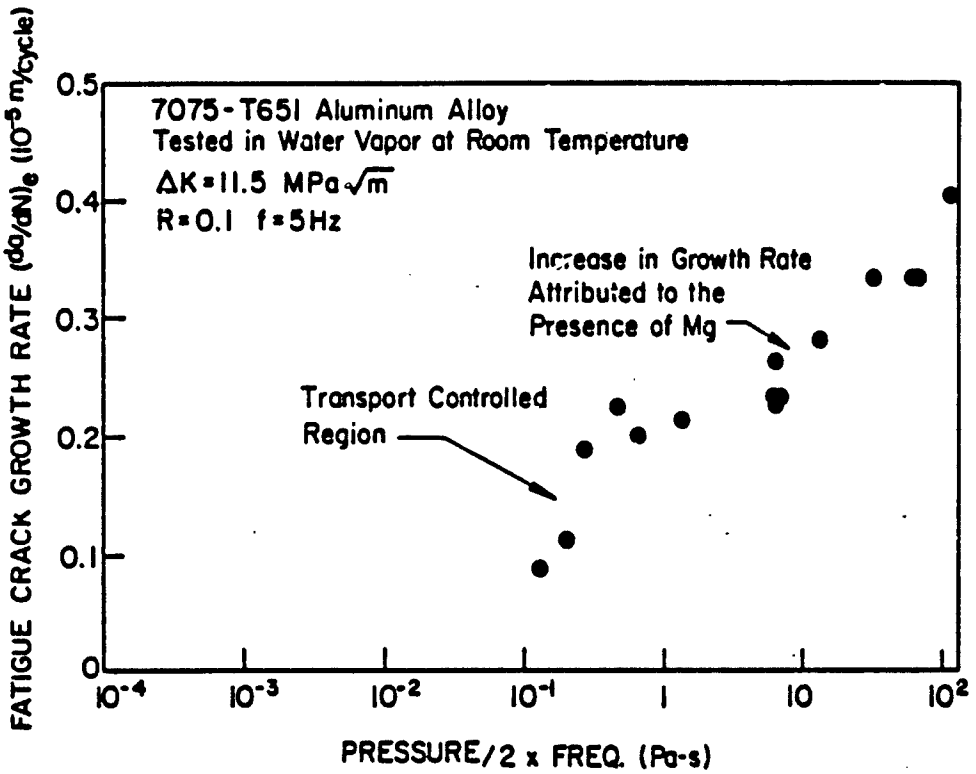

Fig. 77: The effect of water vapor pressure (or pressure/2xfrequency) on fatigue crack growth in 7075-T651 aluminum alloy at room temperature [26].

DISTRIBUTION LIST

January, 1982

Dr. Alan Rosenstein
AFOSR/NE
U. S. Air Force Office of Scientific Research
Bolling Air Force Base
Washington, DC 20332 (6)

AFWAL/MLLS
Attn: Dr. Terry Ronald (1)
Dr. Walt Griffith (1)
Dr. F. H. Froes (1)

WPAFB, Ohio 45433

Prof. I. M. Bernstein (1)
Dept. of Metallurgy/Material Science
Carnegie-Mellon University
Pittsburgh, PA 15213

Mr. Walter Cebulak (1)
Alcoa Technical Center
Alloy Technology Division
Alcoa Center, PA 15069

Dr. David L. Davidson (1)
Mechanical Sciences Dept.
Southwest Research Inst.
San Antonio, TX 78284

Prof. Morris E. Fine (1)
Dept. of Materials Science
Northwestern University
Evanston, IL 60201

Prof. Michael J. Koczak (1)
Dept. of Materials Engineering
Drexel University
Philadelphia, PA 19104

Dr. James Lankford, Jr. (1)
Mechanical Sciences Dept.
Southwest Research Inst.
San Antonio, TX 78284

Prof. Alan Lawley (1)
Dept. of Materials Engineering
Drexel University
Philadelphia, PA 19104

Prof. Art McEvily (1)
Dept. of Metallurgy
University of Connecticut
Storrs, CT 06268

Mr. Henry Paris (1)
Alcoa Technical Center
Alloy Technology Division
Alcoa Center, Pa 15069

Dr. Howard Hamilton (1)
Rockwell Science Center
Thousand Oaks, CA 91360

Prof. Thomas Sanders (1)
Purdue University
School of Materials Engineering
Chemical Metallurgy Engineering Building
West Lafayette, IN 47907

Dr. J. S. Santner (1)
Materials Research Lab., Inc.
One Science Road
Glenwood, IL 60425

Dr. Shankar M. L. Sastry (1)
McDonnell Douglas Res. Lab.
St. Louis, MO 63166

Mr. James Staley (1)
Alcoa Technical Center
Alloy Technology Division
Alcoa Center, PA 15069

Prof. E. A. Starke, Jr. (1)
Dept. of Materials Science
University of Virginia
Charlottesville, VA 22901

Prof. A. W. Thompson (1)
Dept. of Metallurgy/Material Sci.
Carnegie-Mellon University
Pittsburgh, PA 15213

Prof. Julia R. Weertman (1)
Dept. of Materials Science
Northwestern University
Evanston, IL 60201

Prof. R. P. Wei (1)
Dept. of Mechanical Engineering & Mechanics
Lehigh University
Bethlehem, PA 18015